DALTON KEI SASAKI

Variability and modeling of surface high frequency waves in the southwestern South Atlantic

São Paulo
2020

DALTON KEI SASAKI

Variability and modeling of surface high frequency waves in the southwestern South Atlantic

A thesis submitted to the Instituto Oceanográfico of the Universidade de São Paulo in partial fulfilment for the degree of Doctor of Science, Oceanography, with emphasis in Physical Oceanography

Advisor: Prof. Dr. Belmiro Mendes de Castro Filho

São Paulo

2020

SASAKI, Dalton Kei, **Variability and modeling of surface high frequency waves in the southwestern South Atlantic**. Thesis (Doctorate) submitted to the Instituto Oceanográfico of the Universidade de São Paulo for the degree of Doctor of Science, Oceanography, with emphasis in Physical Oceanography

Evaluated in: ____/ ____/ _____

Corrected Version

Examination Board

Prof. Dr.______________________________ Instituição ________________________
Presidente Assinatura ________________________

Prof. Dr.______________________________ Instituição ________________________
Conceito ______________________________ Assinatura ________________________

Prof. Dr.______________________________ Instituição ________________________
Conceito ______________________________ Assinatura ________________________

Prof. Dr.______________________________ Instituição ________________________
Conceito ______________________________ Assinatura ________________________

ACKNOWLEDGEMENTS

I want to extend my deepest gratitude to my advisor, professor Belmiro Castro, for allowing me to conduct research independently and for all the support over time. I am indebted to professor Shuyi Chen, who kindly accepted me in my visit to Seattle and showed me how to a better researcher and scientist. I deeply appreciate my family support through this entire period. My special thanks for my parents Shizue and Airton, and also to other people in my family, Natalia, Samuel, Seiju, Mara, Mako, Satsuki, Emi. Without their guidance and company, this work wouldn't exist. Thamirys, my partner has been wonderful through the entire program. Her support and care were fundamental to balance work and other aspects of life. I am grateful for all fun I had with her and my numerous friends in IO-USP Danilo, Paula, Ju, Cauê, Gil, Patola, Pedin, Thiago, Carine, José Roberto, Iago, Guilherme, Luiza, Dante, Iury, Helio, Marina N., Laura, João, Filipe, Igor, Domo, Burns, Marina T., Maiá, Patrick, Satie, Daniela, Silvio, Josi, Lourival and also to my friends in Seattle Guiwan, Yuanwen, Ajda, Ben, Edo, Jackie, Litai, Yuk, Shuting, Brandon, Megan, Lukas, Robin, Hamid Zahra, Emily, Rachel, Ed, Sara, Felipe, Ruela, Leão, Luiz. We shared invaluable moments. I would like to say thank you to Carolina Gramcianinov, a long-time friend who collaborated with this thesis. I also appreciate the company of my good old-time friends Eduardo, Nicolas, Rafael, Germano and Fabio. Thank you all for being present in good and difficult moments.

No less important were the IO professors Marcelo, Paulo, Olga Ilson, Joseph, Rubens, Eduardo, Javier, Rui, Marcia, Rosa, Rafael who set a lot of examples, not only professionally, but also for life. Without the staff of IO-USP, this work would not be possible. Thanks Ana Paula, Letícia, Daniel, Éder, Ricardinho, Maria, Lurdes, Vera and so many others. I also acknowledge the importance the staff in the Department of Atmospheric Sciences of University of Washington Dennis, Hettie, Francis who were also very kind and professional.

I am grateful for the Instituto Oceanográfico of Universidade de São Paulo and the Department of Atmospheric Sciences of University of Washington for providing all the support and environment necessary to develop my research and also for the Conselho Nacional de Desenvolvimento Científico e Tecnológico (CNPq) for the funding (processes number 163120/2015-3 and 201561/2018-2).

This study was financed in part by the Coordenação de Aperfeiçoamento de Pessoal de Nível Superior - Brasil (CAPES) - Finance code 001.

I am also grateful for the open source and python communities. These initiatives makes the work a lot more enjoyable and the world better. This research was conducted using data from the Global Ocean Observing System (GOOS), to the Programa Nacional de Boias (PNBOIA), Rede Ondas, the National Data Buoy Center (NDBC) from the USA and the Climate Forecast System of the National Oceanic and Atmospheric administration (NOAA) from the USA.

“*The world will not evolve*
past its current state of crisis
by using the same thinking
that created the situation.”

Albert Einstein

RESUMO

SASAKI, Dalton Kei, **Variability and modeling of surface high frequency waves in the southwestern South Atlantic**. Thesis (Doctorate) – Instituto Oceanográfico, Universidade de São Paulo, São Paulo, 2020

O objetivo deste trabalho foi descrever a variabilidade do clima de ondas no Atlântico Sudoeste com base em suas forçantes. A principal ferramenta utilizada neste trabalho foi o Modelo de Ondas da Universidade de Miami. Para avaliar e melhorar os resultados do modelo, implementamos uma parametrização da função fonte de forçante do vento construída no experimento australiano de águas rasas (Donelan et al., 2006) e, também, um algorítmo que inclui o espectro de ondas nos contornos do modelo (Capítulo 2). Os resultados com diferentes algorítmos são testados com as medições do programa de bóias americanas *National Data Buoy Center* (NDBC), do Programa Nacional de Boias (PNBOIA) e também da Rede Ondas. As simulações de ondas, as componentes do vento à 10m, a altura do geopotencial em 850hPa da reanálise Climate Forecast System e um conjunto de dados do rastreamento de ciclones foram empregados para estudar as relações entre a variabilidade interanual das ondas forçadas pelo vento no Atlântico Sudoeste (Capítulo 3) e também a variabilidade sazonal e alta frequência (Capítulo 4). Os resultados indicam que os principais mecanismos que regem a variabilidade interanual estão associados à modulação da posição da Alta Subtropical do Atlântico Sul (ASAS) e ciclones indicados pela primeira Função Ortogonal Empírica (EOF) do vento zonal e da altura do gepotencial em 850hPa, que agem sobre a EOF2 da altura significativa de onda (swh). Considerando a variabilidade de alta frequência (processos com período menor que 14 dias), as condições que definem a direção dominante de ondas na costa sul e sudeste da América do Sul estão atreladas à posição de ciclones e anticiclones transientes e também a posição da ASAS. A swh média, junto à costa associada ao flanco oeste de ciclones (anticiclones), é de 2-4m

(1-2m). Os resultados indicam, ainda que a variabilidade internual (entre 1 e 8 anos) no Atlântico Sudoeste possui variância explicada pelos resultados do modelo é de apenas 2%.

Palavras-chave: Ondas, modelagem, ciclones, Anticiclone Subtropical do Atlântico Sul, parametrização

ABSTRACT

The objective of this work was to describe the climate variability of the waves on the southwestern region of the South Atlantic based on the wind forcing. The main tool for wave simulations in this work was the University of Miami Wave model (umwm). In order to evaluate and improve the results of this model, we implemented a wind input source function built in the Australian Experiment of Shallow Water (Donelan et al., 2006) and also an algorithm that includes the lateral boundary in the model (Chapter 2). The results of the different algorithms are compared against observations of the American National Data Buoy Center (NDBC) , the brazilian National Buoy Program (PNBOIAS) and also the brazilian Rede Ondas datasets. The wave simulation, the 10m wind components, the 850hPa geopotential height from the Climate Forecast Reanalysis System (CFSR) and a cyclone tracking dataset were used to study the interannual variability (Chapter 3) and also the seasonal and high frequency variability (Chapter 4) of the surface wind waves on the Southwestern Atlantic. The results indicate the main mechanisms that controls the interannual variability of waves are the meridional shifting and intensity of the South Atlantic Subtropical Anticyclone (SASA) indicated by the Empirical Orthogonal Function (EOF) 1 of the geopotential height in 850hPa and the EOF1 of the zonal wind, which act over the EOF2 of the significant wave height. In the high frequency case (processes with period lower than 7 days), the conditions that define the dominant wave direction on the South and Southeast coast of South America are linked to the position of transient cyclones, anticyclones and also the position of the SASA. The average significant wave height close to the coast in the western flanks of cyclones (anticyclones) present values of 2-4m (1-2m). The results also indicate the low interannual variability has an explained variance that represent only 2% in the model results. **Keywords**: Waves, model, cyclones, South Atlantic Subtropical Anticyclone, parametrization

LIST OF FIGURES

SUMMARY

1 INTRODUCTION

Surface gravity waves are relevant for the navigation safety, the operation of ports and the operation of offshore oil platforms. They may also enhance flooding and erosion on the coasts when storm surges and high spring tides occur simultaneously. The waves also have a role as the coupler interface between the ocean and the atmosphere: they control the exchange of momentum between both environments (Donelan et al., 2012). Surface gravity waves may also be important for the water mass formation, since they may affect the rate of mixing in the water column through non-breaking processes and affect water mass formation which acts, for example, in the meridional overturning circulation (Babanin et al., 2012).

Our main interest is to study the variability of the surface waves on the southwestern region of the South Atlantic. We organized this Thesis in five different chapters. In the first chapter, an overview of the entire work is presented. In Chapter 2, we implement a wind input source function (Donelan et al., 2006) and also lateral boundary forcing in the code of the University of Miami Wave Model (umwm). Umwm hasn't been tested on areas where the swell is important, or within regions with weak to intermediate winds. Recently, (Liu et al., 2017) evaluated umwm by comparing it with the WavewatchIII model (ww3) under hurricane winds and observed that it overestimates (underestimates) high (low) values of significant wave height. The authors suggests that the biases are due to the wind input source function and the non linear source function of umwm. We hypothesize that implementing the source function of Donelan et al. (2006) in the umwm code will lead to improvements in the aforementioned comparisons and also that the original source function will able to reproduce the wave variability under swell conditions in shallow and deep water environments. In order to test our hypothesis, we compare the wave bulk parameters of the National Data Buoy Center (NDBC) buoys observations and the results of a global wave model using the original and the newly implemented source function.

The hypothesis is also tested on shallow water environments using a high resolution grid. In this case, a lateral boundary forcing was implemented in the umwm, since the wave modeling in shallow waters requires higher grid resolution and, also, the energy introduced into the grid by the swell.

The interannual variability of the wave climate is studied in Chapter 3. There are few works that studied the interannual variability in the SW region of South Atlantic, which found little or non significant correlation with indexes such as the El Niño Southern Oscillation (Pereira and Klumb-Oliveira, 2015; Dragani et al., 2010). Initial conditions are not fundamental in determining how a wave model simulation will evolve throughout a long period of time, since the wave problem variability is essentially controlled by the wind forcing over time. Thus, understanding the variability of the wind field is fundamental for the study of the wave climate. Our hypothesis is that the Southern Annular Mode (SAM) modulates the wave climate through the South Atlantic Subtropical Anticyclone (SASA) and, also, the position and occurrence of transient cyclones. We test this hypothesis by filtering the frequencies higher or equal than $year^{-1}$ and studying the filtered signals using Empirical Orthogonal Functions (EOFs) to evaluate the 850hPa geopotential height fields, the 10m wind components and the significant wave height calculated by umwm.

In Chapter 4 our question is: what are the time and spatial scales of winds that are relevant for the wave climate? Although previous studies about cyclones and the South Atlantic Subtropical high are important for the long term variability, the effects of the spatial structure and position of these systems have not been studied yet. Our hypothesis is that cyclones and anticyclones have preferential positions that control the wave variability at the coast, followed in importance by the seasonal variability associated to the SASA and by the interannual signals.

In Chapter 5 the final remarks summarize the main conclusions of this work.

2 MODELING OF SURFACE WIND WAVES

2.1 Introduction

It is becoming clear that waves are important for large-scale geophysical processes, both for the atmosphere and the ocean (Babanin et al., 2012). Waves are relevant in the exchange of momentum between the atmosphere and ocean (Donelan et al., 2012) and, as Cavaleri et al. (2007) mention, the inclusion of sea-state momentum in atmospheric forecast models were shown to improve the forecast skill at the European Centre for Medium-Range Weather (ECMWF). Moreover, a significant reduction of the SST bias in the tropical Atlantic Ocean and an improvement of 10% in the magnitude of large scale currents were obtained by including the forecasts of Météo-France wave model in the simulation of the Nucleus for European Modeling of the Ocean (NEMO) Ocean Model. In this system, the results also show changes of the order of 10 to 20% in the average energy flux and momentum to the ocean, when compared to classical parametrizations in ocean models (Chune and Aouf, 2018). Regional coastal forecast systems such as the New York Harbor Observing and Prediction System (NYHOPS) also have taken advantage of wave ocean coupling (Georgas and Blumberg, 2010) and have successfully predicted storm surges in the streets of New Jersey (Blumberg et al., 2015). The formulation of NYHOPS has a sea surface roughness that depends on the steepness of the modeled waves (Taylor and Yelland, 2001). Wave models are also part of atmosphere-ocean-waves models used in the study of hurricanes (Chen et al., 2007; Chen and Curcic, 2016; Curcic et al., 2016). The coupling of waves in such systems improves the direction and intensity of surface wind speeds, which are important for the evolution of the storm (Chen et al., 2013).

The present knowledge about the main wave processes allows wave models to output satisfactory results, at least on the large scale (Cavaleri et al., 2007). This has allowed several operational centers to produce good regional and global wave hindcasts in the last decade (Tolman, 2002; Chawla et al., 2013; Pilar et al., 2008) and has also allowed the assessment of wave climate in several parts of the world, such as the North Sea (Weisse and Gnther, 2007), the southwest South Atlantic (Pianca et al., 2010; Pereira and Klumb-Oliveira, 2015), the North Atlantic (Gulev and Hasse, 1999). There are tow types of wave models: phase-resolving models and phase-averaged models (e.g. Rusu, 2012). The first family of models are computationally very demanding as they solve the sea surface elevation in space/time and need to resolve a fraction of the wave periods and lengths. On the other hand, phase-averaged model describes the evolution of the wave spectrum (superposition of sinusoidal waves that travel in different frequencies and directions, assuming random phase) and are based on the energy balance equation (Equation 2.1). This equation solves for the advection of the waves and also includes sink/source functions that act to decay/grow waves at a given point. The wave model formulation is explained in details in Section 2.1.1.

Recently, the Australia Shallow Water Experiment (AUSWEX) (Young et al., 2005; Donelan et al., 2006) revealed details on wave dynamics and its results were used to update the source/sink functions of phase-averaged wave models (Liu et al., 2017, 2019; Tsagareli et al., 2010). These experiments led Liu et al. (2017) to simulate the Hurricane Ivan (2004) using different formulations of ww3 and also the University of Miami Wave Model (umwm). Umwm was developed as a part of a numerical component of a coupled atmosphere-wave-ocean model with emphasis on numerical efficiency in high wind scenarios (Donelan et al., 2012; Chen and Curcic, 2016). This model was successfully tested in areas with intermediate and high wind speeds in the North Sea and under Hurricane Ikke. In Liu et al. (2017) the model also produced accurate results when compared to measurements of the National Data Buoy Center (NDBC) buoys, but tended to overestimate (underestimate) the significant wave height (swh) during high (low) waves events and also showed less accuracy in representing the wave bulk parameters than ww3. These inaccuracies were attributed to the wind input source function and also to the non linear source function parametrizations present in umwm.

While high resolution grids increase the level of detail in the simulated processes, they also increase the cost the computation effort. The resolution of these grids allow the models to better solve processes such as the interaction of the waves with currents and the bottom topography, and allow a greater number of processes to act on the wave spectrum over space and time. Refraction, triad non-linear interaction and shoaling are examples of processes that happens when the waves occur over shallow water (Cavaleri et al., 2007). In order to compensate the prohibitive cost of running a basin wide high resolution grid, chains of models are usual implementations for regional forecast and studies (Chawla et al., 2013). In the following section we present the formulation of a spectral model and focus on the source functions present in umwm.

2.1.1 What is a wave model?

The linear theory of gravity waves is used to interpret a fully arisen sea at a given wind speed. The observed sea surface is integrated as the infinite sum of single waves with different wave numbers. The set of all individual waves is also known as spectrum of waves (Pierson, 1955). It may be formulated as the spectrum of elevation variance (E) as a function of the wave number k and the direction of propagation ϕ.

The spectrum is incorporated in the wave action equation (Andrews and McIntyre, 1978) yielding the energy balance equation (as in Donelan et al. (2012)):

$$\frac{\partial E'}{\partial t} + \frac{\partial [E' c_g cos\phi + u]}{\partial x} + \frac{\partial [E' c_g sin\phi + v]}{\partial y} + \frac{\dot{k} E'}{\partial k} + \frac{\dot{\phi} E'}{\partial \phi} = \rho_w g \sum_{i=1}^{n} S_i \tag{2.1}$$

where E' is the wave variance spectrum, t is the time, x and y are respectively the zonal and meridional coordinates, c_g is the group speed velocity, ϕ is the wave direction, u, v are the mean current in wave boundary layer depth, $\dot{k}$ is the advection in wave number space, $\dot{\phi}$ is the advection in directional space, ρ_w is the water density and g is the gravity and S_i are the different wave source functions.

The spectral advection of waves the absence of significant currents propagate according to the left-hand-side of Equation 2.1. The right-hand side is related to the source and sink functions, which are responsible for inducing local growth or decay of the waves (Komen et al., 1994; Donelan et al., 2012).

The wave modeling community separated the wave problem physics in the following themes: Generation of waves by the wind, Dissipation term (mainly white-capping and bottom dissipation) and Nonlinear interactions in shallow water and deep water (Cavaleri et al., 2007). In the following paragraphs we present these source functions with emphasis on the formulation of umwm (Donelan et al., 2012).

2.1.1.1 Generation of waves by the wind

The generation of waves by the wind is traditionally treated by a quasi-linear theory (Miles, 1957) modified by Janssen (1991). Miles (1957) proposed that resonance was the process responsible for the wave generation, although it has been criticized due to the neglect of the turbulence (Janssen, 1991; Donelan et al., 2006). This approach succeeds in predicting the wave growth (Cavaleri et al., 2007). The growth rates of Miles' theory is:

$$\gamma = \frac{1}{\omega F}\frac{\partial F}{\partial t} \tag{2.2}$$

where ω is the wave frequency, γ is the growth rate and F is the wave power spectrum. Another alternative to model the wave generation is the study by Jeffreys (1924, 1925), who proposed the sheltering hypothesis. This hypothesis states that the wind blowing on a surface of existing waves supplies energy for their growth by means of the difference of pressure between the windward and leeward of the waves.

Measurements in solid wave models indicated that Jeffreys' theory couldn't account for the entire rate of wave growth (Stanton et al., 1932; Menéndez et al., 2008). Those experiments were made in a 15 meters long and 30cm by 30cm cross sections wind tunnel (Stanton et al., 1932) and could not reproduce the whole spectrum of possibilities of a lake or an ocean. Donelan et al. (2006) found that Jeffrey's hypothesis explains the results of AUSWEX, where the authors found the exponential growth depends on the slope of the waves. The authors also found the occurrence of a detachment from the airflow on the crests and a reattachment on the windward side of the wave under cases where the inverse wave age (u_{10}/c_p) ranges from 5.1-7.6, characterized as "very strongly forced waves", where u_{10} is the wind at 10m and c_p is the phase velocity of the wave. There are other approaches to the generation of waves by wind, some of which are nonlinear (Townsend, 1980; Belcher and Hunt, 1993). Nevertheless, regarding wind-wave generation, there is still no conclusive theory (Cavaleri et al., 2007).

In Donelan et al. (2006) and Donelan et al. (2012), the wind input source function is presented under the sheltering hypothesis of Jeffreys (1924, 1925). The growth rate of the elevation of the surface water with $\eta_w(x,t) = a\cos(kx - \omega t)$ is proportional to the growth rate of the spectral density of the wave and to the pressure perturbations induced by the flow separation (η_w is the surface elevation and a is the amplitude in meters):

$$\frac{\partial F(\omega)}{\partial t} = S_{in} = \frac{1}{\rho_w g}\overline{p(x,t)\frac{\partial \eta_w(x,t)}{\partial t}} \tag{2.3}$$

The parametrization of Donelan et al. (2006) includes the pressure perturbation component in the growth rate as follows:

$$\gamma = G\sqrt{B_n}\left(\frac{u_{10}}{c_p} - 1\right)^2 \tag{2.4}$$

where G represents the flux separation - a function of c_p/u_{10} and of the wave slope (represented by the spectral saturation B_n, which depends upon the spectral spreading function A). G is defined as follows:

$$G = 2.8 - 1.00\left\{1 + \tanh\left[10\sqrt{B_n}\left(\frac{u_{10}}{c} - 1\right) - 13\right]\right\} \tag{2.5}$$

$$B_n(\omega) = \frac{\omega^5 E(\omega)}{2g^2}A(\omega) \tag{2.6}$$

$$A(\omega)^{-1} = \int_{-\pi}^{\pi} K(\omega,\phi)d\phi \tag{2.7}$$

where A is the spectral spreading function and K is the distribution of wave spectral density.

In Donelan et al. (2012), S_{in} was parametrized as:

$$\begin{aligned} S_{in}(k,\phi) = {} & A_1(U_{\lambda/2}\cos\theta - c_p - u\cos\phi - v\sin\phi) \\ & |U_{\lambda/2}cos\theta - c_p - u\cos\phi - v\sin\phi|\frac{k\omega}{g}\frac{\rho_a}{\rho_w}E(k,\phi) \end{aligned} \tag{2.8}$$

where the wθ is the angle between the wave direction and the wind and A_1 is a tuneable coefficient, $U_{\lambda/2}$ is the wind speed at a height of one half wave length $(\lambda/2)$m ρ_a is the air density. This wind input source function allows the transfer of energy and momentum from wind to waves when $U_{\lambda/2}cos\theta > c_p - u\cos\phi - v\sin\phi$ and negative transfer when $0 < U_{\lambda/2}cos\theta < c_p - u\cos\phi - v\sin\phi$ or when the swell propagate against the wind ($cos\theta < 0$). According to the author, S_{in} goes to zero (the wind forcing vanishes) when the waves approach full development. We will call hereinafter the wind input source function of Donelan et al. (2006) and Donelan et al. (2012) respectively as Sin_{don06} and Sin_{don12}.

2.1.1.2 The dissipation term

WHITE-CAPPING

The physics of spectral dissipation of waves is poorly understood and its most important processes are related to complex and little known physics of wave breaking (Babanin, 2011). There is little agreement among different analytical theories of spectral dissipation and also experimental results. Today, two experimental functions cover the entire wave spectrum and consider non-local wave number dissipation (Cavaleri et al., 2007; Babanin, 2011). The first evaluates the spectral dissipation using the balance of the source terms (Donelan, 2001) and the second shows that dissipation happens mainly at scales smaller than the spectral peak waves (Young and Babanin, 2006).

Here, we present the dissipation source function in umwm (Equation 2.9) (Donelan et al., 2012), which was calculated based on (Donelan, 2001). This source function depends on the the degree of saturation of the wind-wave spectra given by $B(k, \phi) = k^4 E(k, \phi)$ and the dissipation sink function (green colors). It parametrizes the wave breaking associated to the effect of reduced (increased) orbital velocity divergence (convergence) (blue colors) and also the increased wave breaking due to plunging breakers in shoaling areas (gray colors), where d is the depth and χ^2 is the mean square slope:

$$S_{ds}(k, \phi) = -A_2 \coth kd [1 + A_3 \chi^2]^2 [B(k, \phi)]^{2.5} \omega(k) E(k, \phi) \tag{2.9}$$

where S_{ds} is the dissipation source function, A_2 and A_3 are tuneable coefficients.

BOTTOM DISSIPATION

Bottom dissipation is a process related to shallow areas where waves interact with the bed. There are many processes associated with bottom dissipation and some of those are unrelated to friction. Known processes affecting the waves energy damping are the percolation of water into porous bed, the damping of energy by muddy bottom, the turbulent effects within the bottom boundary layer, mobile sediment beds and also the roughness of bedform (Cavaleri et al., 2007).

As an example, one may cite movable beds in sandy bottoms (Cavaleri et al., 2007). In these cases the generated bedforms have its own bottom roughness, which is more important than the effects of the bottom boundary layer itself. The modeled wave spectra shows good agreement to observations when the variability of the bed ripples are included in bottom friction, working even better than the empirical Joint North Sea Wave Project (JONSWAP) bottom friction term in low and high energy conditions (Ardhuin et al., 2003).

2.1.1.3 Nonlinear interactions

DEEP WATER

Non linear interactions in homogeneous seas with constant depth are explained theoretically by a weak nonlinear interaction resolved by a Boltzmann Integral for surface gravity waves (Hasselmann, 1962). Known as the non linear quadruplets interactions, a set of four waves can exchange energy when the resonance conditions are satisfied.

This complex integral is computationally time consuming, making it unsuitable for operational purposes (Cavaleri et al., 2007). Hence, the discrete interaction approximation (DIA) was proposed as a simpler but more efficient deep water solution of the Boltzman Integral (Hasselmann and Hasselmann, 1985; Hasselmann et al., 1985). Although important, the DIA is not very accurate, since it produces errors in the shape and in the intensity of the modeled spectrum.

Besides, the original Boltzmann integral is valid only in a deep, homogeneous, stationary sea state. Other approaches for shallow water applications do not consider a sloping bottom, which means that the initial assumptions of the Boltzman integral are violated. Still, the DIA is good enough to allow good skill for the models when compared to buoy measurements in reanalysis hindcasts (Tolman, 2002).

Non linear interactions were also studied by Pierson et al. (1992), who found the energy dissipated in the spectrum by coalescing groups is passed to lower and higher frequencies. As a result, the spectrum is broadened and reduced at the same time. While the energy passed to higher frequencies is dissipated, the energy passed to lower frequencies bands increases longer waves. Donelan et al. (2012) parametrized this effect, through an algorithm that passes a quantity of energy proportional to the energy dissipated by the spilling breakers in a conservative manner to the next two lower wave numbers bins following:

$$S_{nl}(k,\phi) = A_5[b_1 S_{sb}(k-\Delta k,\phi) + b_2 S_{sb}(k-2\Delta k,\phi) - S_{sb}(k,\phi)] \tag{2.10}$$

where S_{nl} is the non linear source function, $b_1 = exp(-16(\Delta\omega/\omega)^2)$, $b_2 = exp(-16(2\Delta\omega/\omega)^2)$, $A_5 = 5$ (default value) and $b_1 + b_2 = 1$, S_{sb} is the dissipation source function associated to spilling breakers, and $\Delta omega$ is the difference between frequencies.

SHALLOW WATER

Shallow water nonlinear interactions are a consequence of the different dispersion relation from the deep water environment, which allows the presence of resonant triad interaction with all wave components traveling with the same speed. These interactions force steepening and pitching of wave crests (Cavaleri et al., 2007).

The nonlinear wave evolution is still an open problem when variable depth is considered. The validation of models at those environments have been made generally at beaches with moderate slope but natural coastlines present environments such as reefs and banks, which have not been incorporated into the studies. Those models do not predict reflection of waves and the nonlinear dynamics associated (Cavaleri et al., 2007).

2.1.2 Hypothesis and objectives

The question of this work is: what is the ability of umwm source functions in predicting the wave conditions where the swell is relevant and in regions of low to intermediate wind speeds? We hypothesize that the model will better predict the wave evolution in regions with high winds and, also, that the including a wind input source function will produce better results. Our second hypothesis is that in shallow water, the high resolution grid will improve the simulation results. To test these hypothesis, our objectives are to compare model results against observations under different wave conditions and also under different grid resolutions. In order to do this we implemented the new wind input source function (Donelan et al., 2006) and also a lateral boundary forcing, which are tested independently. The details are presented in Sections 2.3.1 and 2.3.2.

2.2 Data and methods

2.2.1 Lateral boundary forcing

Algorithm

The code of umwm was changed to include forcing on the lateral boundaries in a high resolution grid. Restart files of the low resolution grid provide the spectrum at each boundary point of the high resolution grid. The spectrum is linearly interpolated from the three closest points of the coarse grid (baricentric linear interpolation). In the code, the spectral information on the boundaries are defined prior the calculation of the source functions and the propagation scheme in the begin of the global time step.

Model grid and data

A basin scale grid is used to generate the incoming swell in the southeastern region of the Brazilian shelf. Its area extends in between (69^oW,60^oS) to ($0.5oW$, 0.5^oS) (Figure 2.1). It is a regular rectangular grid with resolution of $0.5^o \times 0.5^o$, 137 longitudinal points and 119 latitudinal points.

The implemented regional grid presents a resolution of $0.05^o \times 0.05^o$, with 160 longitudinal points and 120 latitudinal points within the area defined in between (49.0^oW, 22.5^oS) and (41.0^oW,27.5^oS) (Figure 2.1).

The bathymetric data was obtained from the ETOPO1 Global Relief Model (`https://www.ngdc.noaa.gov/mgg/global/`) and was bilinearly interpolated to the grids.

The global wave hindcast ww3 by the National Oceanic and Atmospheric Administration (NOAA) results are used as additional dataset for the evaluation of the umwm results. This hindcast uses the Climate Forecast System v2 Operational Analysis Time Series(CFSv2) (`https://www.ncdc.noaa.gov/`), with a 0.5^o resolution grid in the period from Feb 2005 through Mar 2019. The distributed data contains significant wave height (swh), dominant wave period (dwp) and dominant wave direction (dwd). The data were obtained at ftp://polar.ncep.noaa.gov/history/waves/.

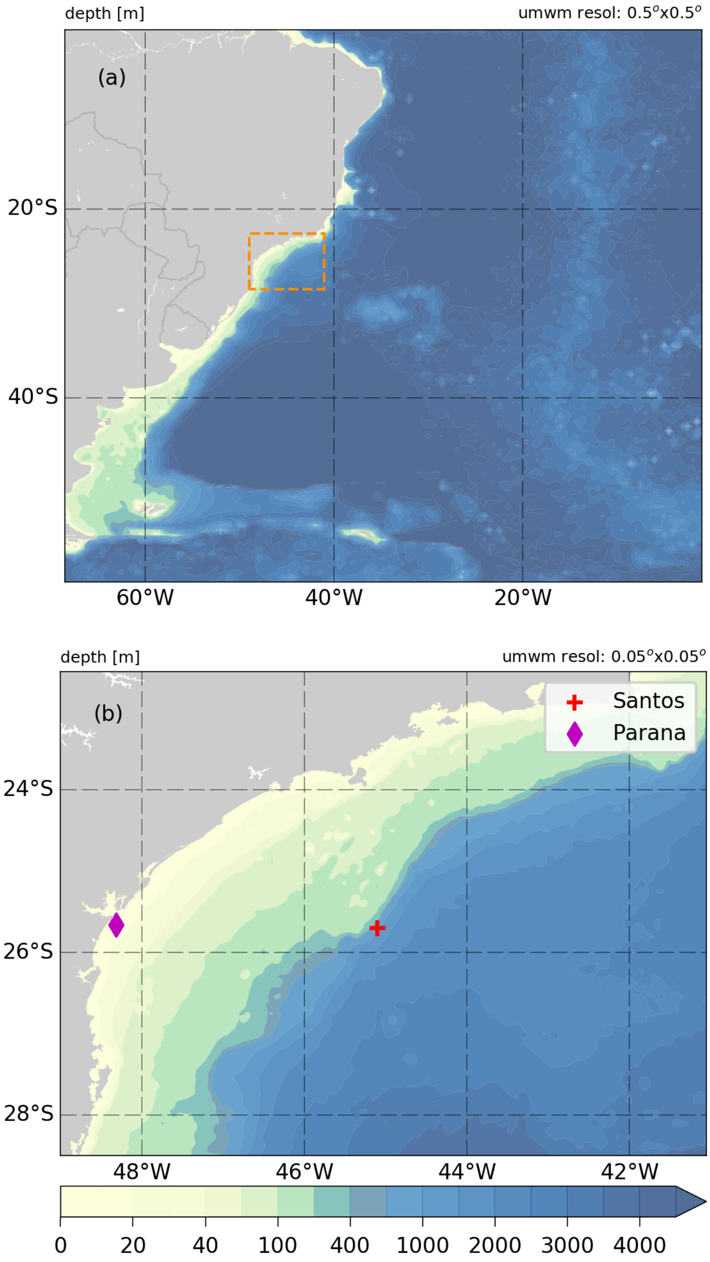

Figure 2.1: (a) The basin scale model grid comprises the Southwest Atlantic. The orange dashed rectangle in the SE brazilian coast indicates the position of the regional grid (b). The regional grid with the red cross and magenta rhombus mark the position respectively of the PNBOIA (Santos - 25.7^{o}S, 44.1^{o}W) and Rede Ondas (Parana - 25.66^{o}S, 48.32^{o}W) buoys. The bathymetry is in meters.

2.2.2 *Wind input source function*

PARAMETRIZATION

We implement the source function Sin_{don06} in umwm described in equation 2.4. The flux separation G is calculated by equation 2.11 configured as:

$$G = \mu_1 - 1.00 \left\{ 1 + \tanh \left[\mu_2 \sqrt{B_n} \left(\frac{u_{10}}{c_p} - 1 \right) - \mu_3 \right] \right\} \tag{2.11}$$

where μ_1=2.8, μ_2=10, μ_3=11 are tunable coefficients. The growth rate is implemented as:

$$\gamma = \begin{cases} a_0 G \sqrt{B_n} (U_r \cos\theta / c_p(f) - 1)^2 \text{ for } U_r \cos\theta / c_p(f) - 1 \geq 0 \\ -a_0' G \sqrt{B_n} (U_r \cos\theta / c_p(f) - 1) \text{ for } U_r \cos\theta / c_p(f) - 1 < 0. \end{cases} \tag{2.12}$$

where a_0=1.0 and a_0'=0.09 are also tunable coefficients.

MODEL GRID AND DATA

A global grid was built in order to test the source function Sin_{don06}. It presents a horizontal resolution of 0.25^o with 1440 longitudinal points, 680 latitudinal points and the wave variance spectrum is discretized into 37 frequencies and 36 directions and the simulated period starts in 2017-Aug-01 and ends in 2017-Oct-01. The maximum and minimum resolved frequencies are respectively 0.0313Hz and 2.0Hz with.

Figure 2.2 presents the areas on the North Pacific and North Atlantic, where the buoys of the USA National Data Buoy Center (NDBC) are located (orange rectangles). The measurements of the NDBC buoys are employed in the evaluation of the wave model results These buoys measure the wave spectrum in the frequency range from 0.02Hz to 0.485Hz (Earle, 1996) and provide swh, mean wave period (mwp) and mean wave direction (mwd) measurements.

The Cross-Calibrated Multi-Platform (CCMP) Ocean Surface Wind vector Analysis (Atlas et al., 2011) dataset provides the 10m wind speed fields between August and September of 2017, which were used to force the global fields of umwm. This dataset of ocean surface wind vector fields has a horizontal resolution of 0.25^{o}x0.25^o and time increments

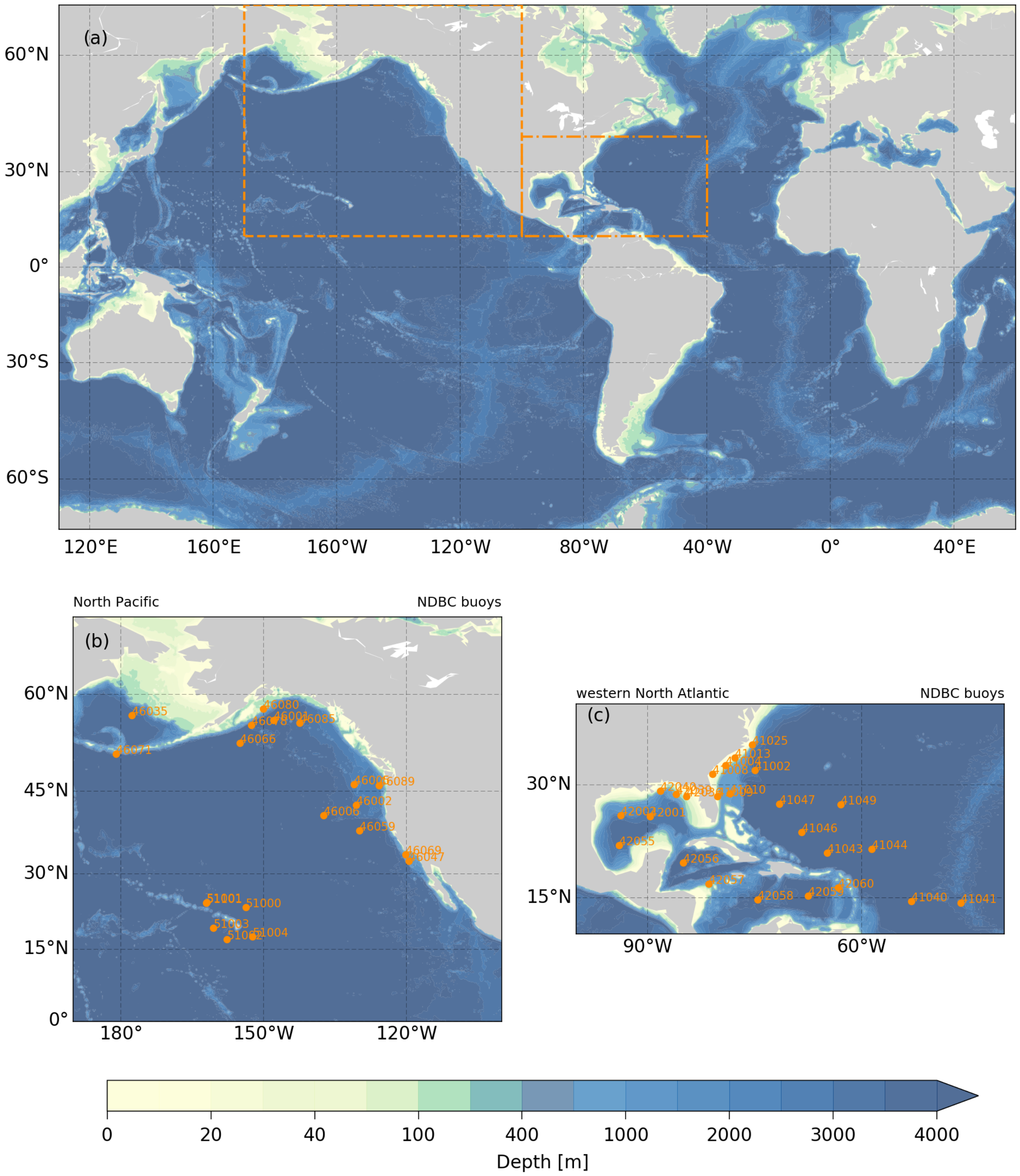

Figure 2.2: (a) The global grid of the wave model. The orange dashed rectangles delimits the area where the National Data Buoy Center buoys are present (b) in the North Pacific and (c) in the western North Atlantic. The orange dots and numbers show respectively the position and the identification of the buoys.

of 6-hours from July 1987 through the present and is built using a Variational Analysis Method (VAM) which cross-calibrated measurements of winds by several microwave satellite instruments such as the SSM/I, SSMIS, AMSR, TMI, WindSat (Atlas et al., 2011).

2.3 Results

2.3.1 Lateral boundary forcing

We present Figure 2.3 in order to compare the similarities and differences between the wave fields in the results of the high and low resolution grids. The swh and mwd fields present spatial structure with similar features. For instance, the swh field show the similar distribution over regions where the values are higher than 3.0m, although noticeable differences are also present. In the high resolution results, maximum values of swh are over 5.0m, whereas in the low resolution case, the maximum values are of about 4.2m. Furthermore, the lateral boundaries of the high resolution and low resolution model present a discontinuity on the wave height fields. It indicates that the propagation of waves within the high resolution grid is slower, or delayed, in comparison with the propagation in the low resolution grid.

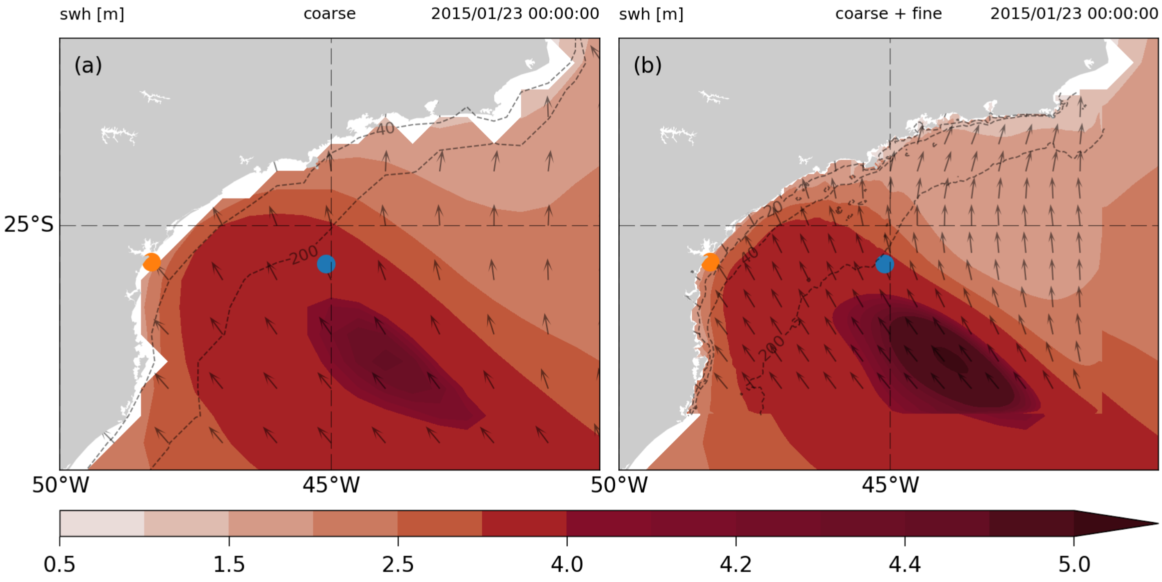

Figure 2.3: Significant wave height in meters in (a) low and (b) high resolution grids. The vectors indicate the mean wave direction. The results of the high resolution grid overlays the low resolution results for comparison. The dashed contours represent the depth in meters.

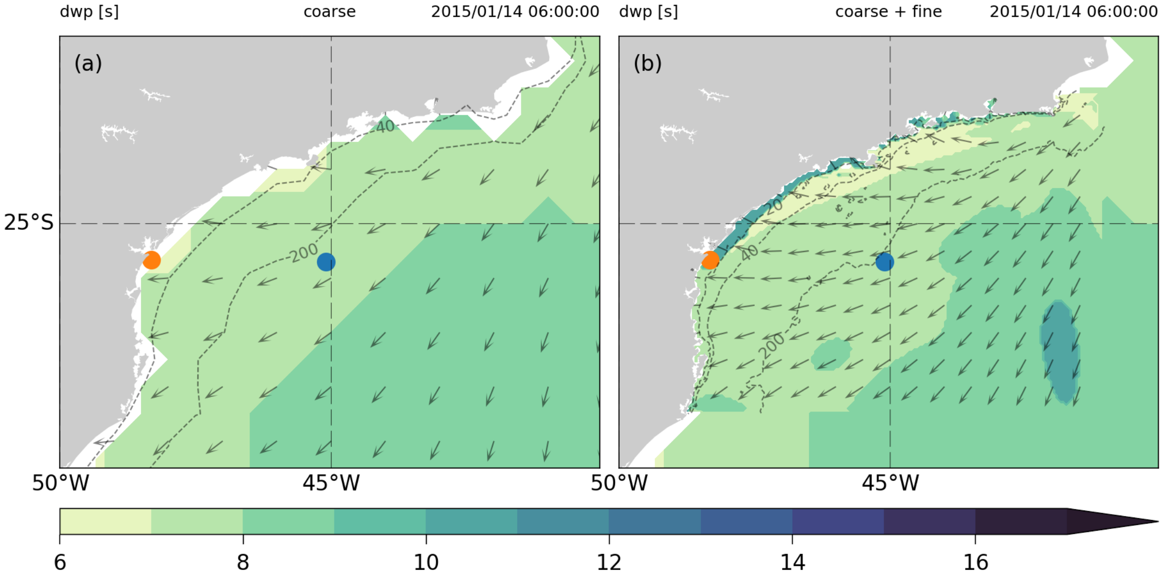

Figure 2.4: Dominant wave period in seconds in (a) low and (b) high resolution grids. The vectors indicate the mean wave direction. The results of the high resolution grid overlays the low resolution results for comparison. The dashed contours represent the depth in meters.

The dwp also present similar wave fields in the high resolution and low resolution grids (Figure 2.4). In intermediate (depths between 20m-200m) and deep water (depths higher than 200m), there is a gradient of dwp from the coast to the open ocean in both grids. In shallow water environment, there is an increase of the dwp marked by the narrow dwp strip parallel to the coast with wave periods values higher than 10s.These high values of dwp over shallow water is present throughout the simulation.

We evaluate the effects of introducing the lateral forcing by comparing the evolution of the wave modeled fields near the Santos buoys with the results of the ww3 reanalysis hindcast and also with the buoy data (Figure 2.5). The swh showed better comparison than the other parameters, is the parameter with best results followed by the mwd and dwp. As the Figure 2.5b shows, the dwp modeled evolves in discrete intervals, while ww3 results show a smoother time series. This is explained by the higher resolution in the frequency space of the spectrum in ww3 hindcast: the wave spectrum consists of frequencies between 0.036-0.963Hz and is divided in 50 bins, while umwm presents a frequency range between 0.0313-2.0Hz divided in 32 bins. As the mean wave direction in ww3 hindcast reanalysis is not available, we use the dominant wave direction at the buoy position instead. In Santos buoy position, the high resolution results present a lag of about 12 hours in the

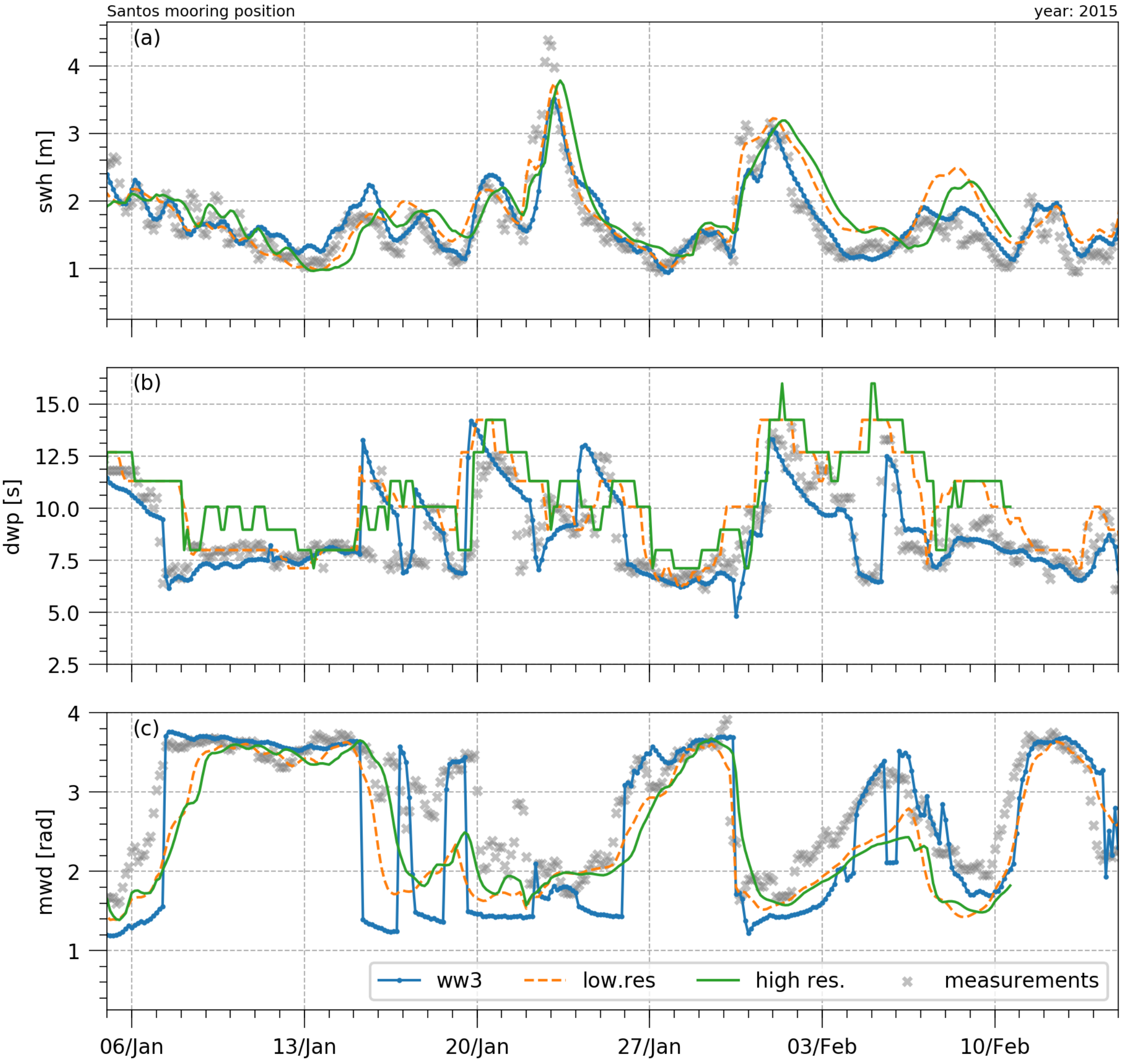

Figure 2.5: Comparison between low and high resolution results of umwm, ww3 and measurements of (a) swh, (b) dwp, (c) mwd on the position of the Santos buoy. The ww3 hindcast results in (c) is the dominant wave direction.

signal of the swh, dwp and mwd when compared with the results of the other models and measurements. Overall, the time series of all parameters show a good agreement between the model results and the measurements on the buoy in Santos, which is quantified by the Taylor Diagram (Taylor, 2001) in Figure 2.6.

The Taylor Diagram compares model and measurements time series in terms of correlation, normalized standard deviation and the root mean squared error. The standard deviation of the high and low resolution umwm results are similar in all three parameters (shw, dwp, mwd), but the correlation is higher in the low resolution results with maximum correlation differences of 0.1. The smaller correlations values in the high resolution grid are a consequence of the time lag introduced by the lateral forcing.

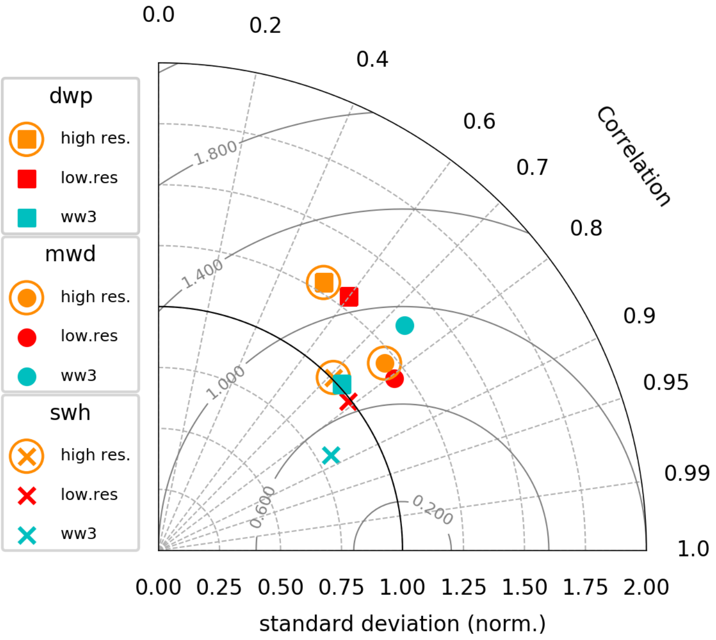

Figure 2.6: Taylor Diagram for the wave parameters of umwm (high and low resolution) and ww3 compared with the measured parameters by the Santos buoy. The gray semi-circles centered at the 1.0 standard deviation and 1.0 correlation coordinates are the root mean squared error. To normalize the standard deviation all time series were divided by the standard deviation of the observations.

The time series of the wave models and of the measurements in the position of Parana buoy are presented in Figure 2.7 and the Taylor Diagram is shown in Figure 2.8. The time series of the significant wave height of the low resolution grid has a significant high correlation (0.81) with the observations and a normalized standard deviation of 1.12. An exception occurs in the period between 30/Jan to 7/February, when there is an overestimation of 0.5m in the wave height. In the Parana buoy position, there is a lag in the swh

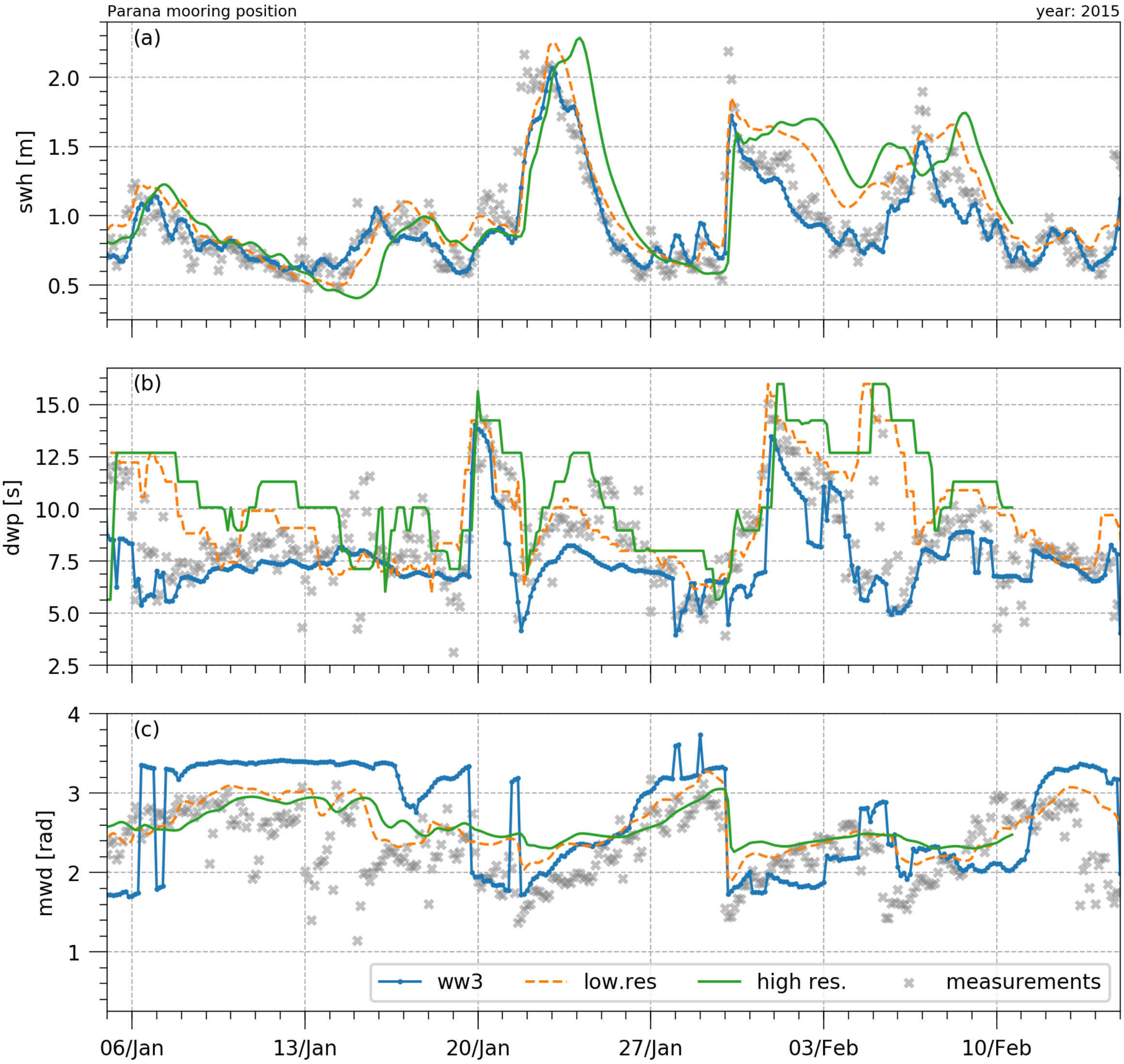

Figure 2.7: Comparison between low and high resolution results of umwm, ww3 and measurements of (a) swh, (b) dwp, (c) mwd on the position of the Santos buoy. The ww3 hindcast results in (c) is the dominant wave direction.

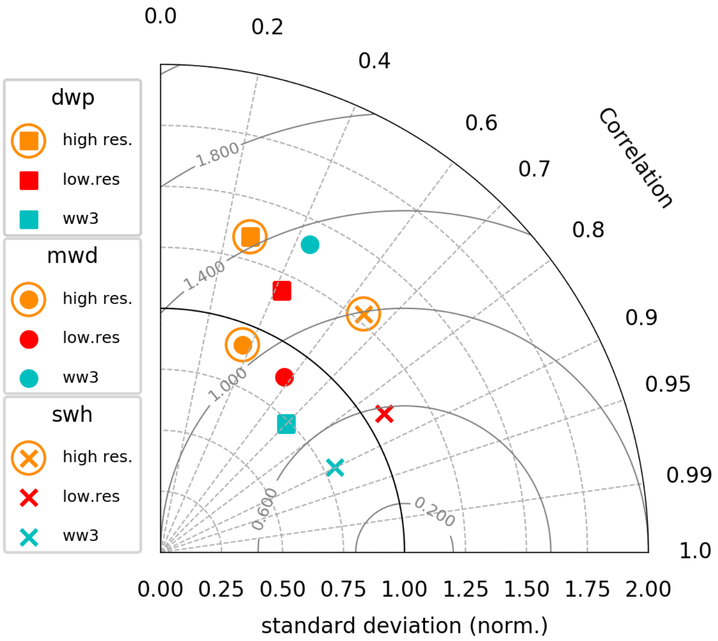

Figure 2.8: Taylor Diagram of the wave parameters of umwm (high and low resolution) and ww3 compared with the measured parameters by the Parana buoy.

of the high resolution time series of up to 1 day and the values between 30/Jan to 7/Feb also present values higher than the measured time series with differences reaching values of 0.8m. The higher values and delay in this result lead to a lower correlation value (0.65).

The dwp of the low resolution umwm model has intermediate correlation with the measurements (0.42), although the modeled time series generally captures the variability in the measurements. The high resolution model usually overestimates the wave period values on the entire series and the correlation with the measurements is low (0.27). In the Parana buoy position, the high resolution results for dwp overestimate values between January 8th and January 15th and also between January 22nd and 25th. Umwm uses the energy balance equation in a basin of varying depth and the advection scheme employs the c_g=$0.5c_p(1 + 2kh/sinh(2kh)$, which is a function of the local depth (h) (Figure 2.9). Overestimated values of dwp near the shoreline are explained by the spilling breakers and by the non linear source function parametrization and also by the convergence of energy produced by a negative gradient of the group velocity (c_g) towards shallow water. When waves propagate from deep to shallow water, the gradient of group velocity forces a convergence in the wave variance spectrum within the same frequency bin (shoaling). This convergence leads to an increase of the energy present in the wave variance spectrum and

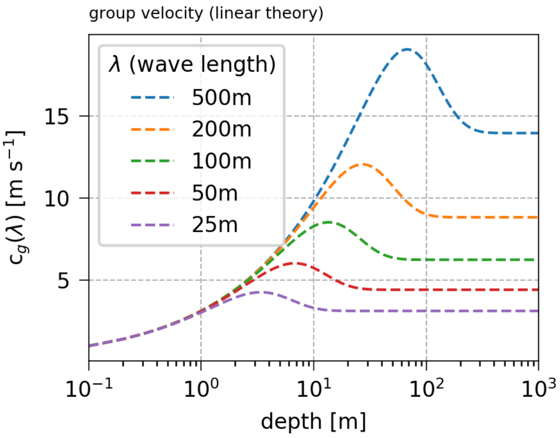

Figure 2.9: Group speed of waves with different wave lengths.

consequently to an increase of the wave steepness (measured by the degree of saturation).

The minimum values of the dwp values occur in intermediate water, where there is an increase in the group speed values from deeper to shallower water (Figure 2.4). Its signature in the wave period is the local minimum of dwp parallel to the coast which is associated with reduced wave breaking due to divergence in the wave spectrum. As the dissipation source function of the wave model parametrizes spilling breakers through the increased steepness, there is an increase in the dissipation by the breakers (Equation 2.9) and the energy is downshifted to lower frequencies in the spectrum by the non linear source function (Equation 2.10). Thus, the convergence of energy due to changes of depths, the increase of the dwp values near the coast. Higher values of dwp at these areas are not a response to the resolution of winds in the high resolution models. The CFSv2 wind speed values over the position of Parana buoy present about 50% of the magnitude in the low resolution grid (Figure 2.10).

The mwd of the low resolution umwm appears as a smoother version of the wave variability, as is indicated by the normalized value of the standard deviation (0.88) and intermediate value of correlation (0.6) in Figure 2.8. In the high resolution case (Figure 2.7), the range of mwd is also smoothed ($\sigma_{norm} = 0.88$) and the time series presents a low correlation between results and measurements (0.38). According to the Taylor Diagram (Figure 2.8), ww3 has the best results among the models followed respectively by the low and high resolution umwm.

2.3.2 Wind input source function

In this section we evaluate the umwm results using NDBC buoys during August-September of 2017 and also discuss the differences between the wave models with different wind input source functions. The wave fields over the oceans may be divided into swell pools and wind wave zones based on global statistics of wind sea/swell intensities and probabilities, following Chen et al. (2002). Swell pools occur on the eastern tropical areas of the oceans and their spatial configuration consists of well-defined tongue shaped zones where swell dominates. Wind wave zones are distributed over the northeast region of Pacific, the northwest region of Atlantic, the Mediterranean Sea, the Southern Ocean, and are characterized as regions where there is an intense wave growth. Here, we call the intermediate areas where neither swell nor wind waves dominate as "transition zones".

Figures 2.11 to 2.16 present wave parameters measured by the NDBC buoys and wave model results simulated on the global grid using Sin_{don12} and Sin_{don06}. We present the time series of swh, mwp and dwp from eight different NDBC buoys. Each buoy summarizes the wave conditions over its region. For instance, in Hawaii case the results of the selected buoy are representative of the surrounding array of buoys. The wave statistics on the Taylor Diagram (panel b of the Figures 2.11 to 2.16) show high correlation values ($0.75 < r < 0.95$) between the model results and measurements, when the buoys are present within transition zones in the Atlantic (Figs 2.11, 2.12, 2.13, 2.14), or in wind wave zones over the Bering Sea and Gulf of Alaska (Figs 2.15, 2.16). On the other hand, the correlation values are lower ($0.75 < r < 0.85$) in the swell pool in Hawaii and offshore the western coast of USA

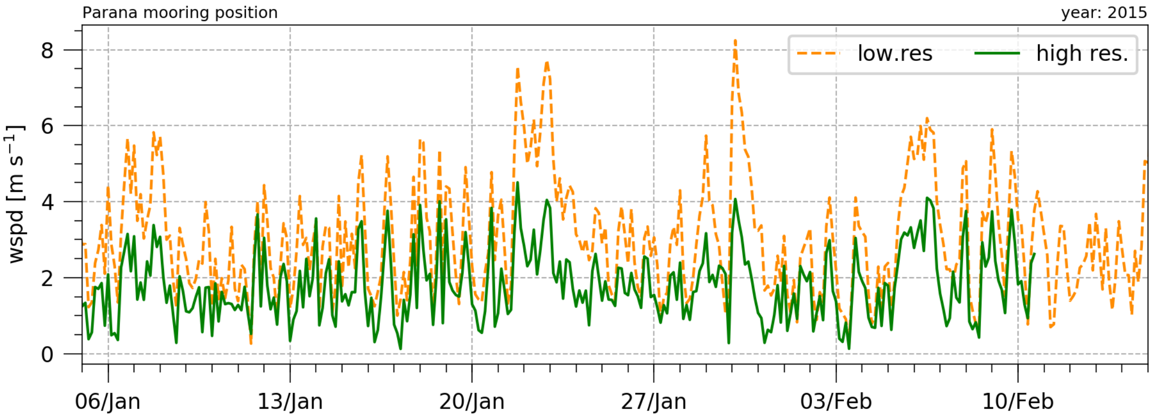

Figure 2.10: Time series of the 10m wind speed (CFSv2) on Parana buoy position in the high and low resolution models. The values were linearly interpolated to the points.

(Figs 2.17, 2.18).

The wave model was originally designed as the wave component of the United Wave Interface Coupled Model (Chen et al., 2013; Chen and Curcic, 2016) and the parametrizations were selected to efficiently simulate waves under strong winds such as in hurricane environments. Low correlation between the observations and the simulated wave parameters may be related to its original design, where non-linear wave-wave interactions are relatively less important when compared with the downshift of the of the energy to longer waves associated to spilling breakers. As discussed by Babanin (2011), if the breaking due to modulational instability (Equation 2.9) is maintained over time by the wind input, the non-linear downshifting of energy in the wave number space will be related to S_{ds}. The temporal scale for the downshift under this process is of tens of wave periods (Babanin et al., 2007), whereas the usual S_{nl} takes hundreds of thousands of wave periods (Babanin, 2011). Over the swell pool on the Pacific and tropical Atlantic, the absence of the parametrization of resonant wave-wave interactions in the model can explain poorer results of the swh (and other wave parameters), indicated by the intermediate correlations values($0.4 < r < 0.7$). The absence of this parametrization in the umwm's physics is a possible explanation for the differences between the wave model results and the observations, in regions where swell dominates the variability. The downshifting of the energy by non linear interactions is important mainly for the wave period and, although the downshifting and spilling breaking quantitative relation has not been established yet (Donelan et al., 2012), the model produces mwp results with high correlation (> 0.7) and accurate values of normalized standard deviation (≈ 1.2) in wind wave zones over the Gulf of Alaska and the Bering Sea. This indicates the non-linear source function related to spilling breakers may be relevant in regions where the swell is not dominant. At the present umwm is less reliable where the swell dominates the wave variability, but confirm the ability of the model on simulating waves in wind wave and transition zones.

Taylor Diagrams in Figure 2.19 summarize the statistics of the collection of wave model results in the positions of NDBC buoys considering the Atlantic and Pacific basins. Each red (or orange) dot indicates the comparison between a pair of measured/modeled time series at a buoy position in terms of correlation and standard deviation. As Taylor (2001) mentions, the azimuthal coordinate represents the correlation coefficient between these pairs, while the radial distance from the origin is proportional to the normalized standard

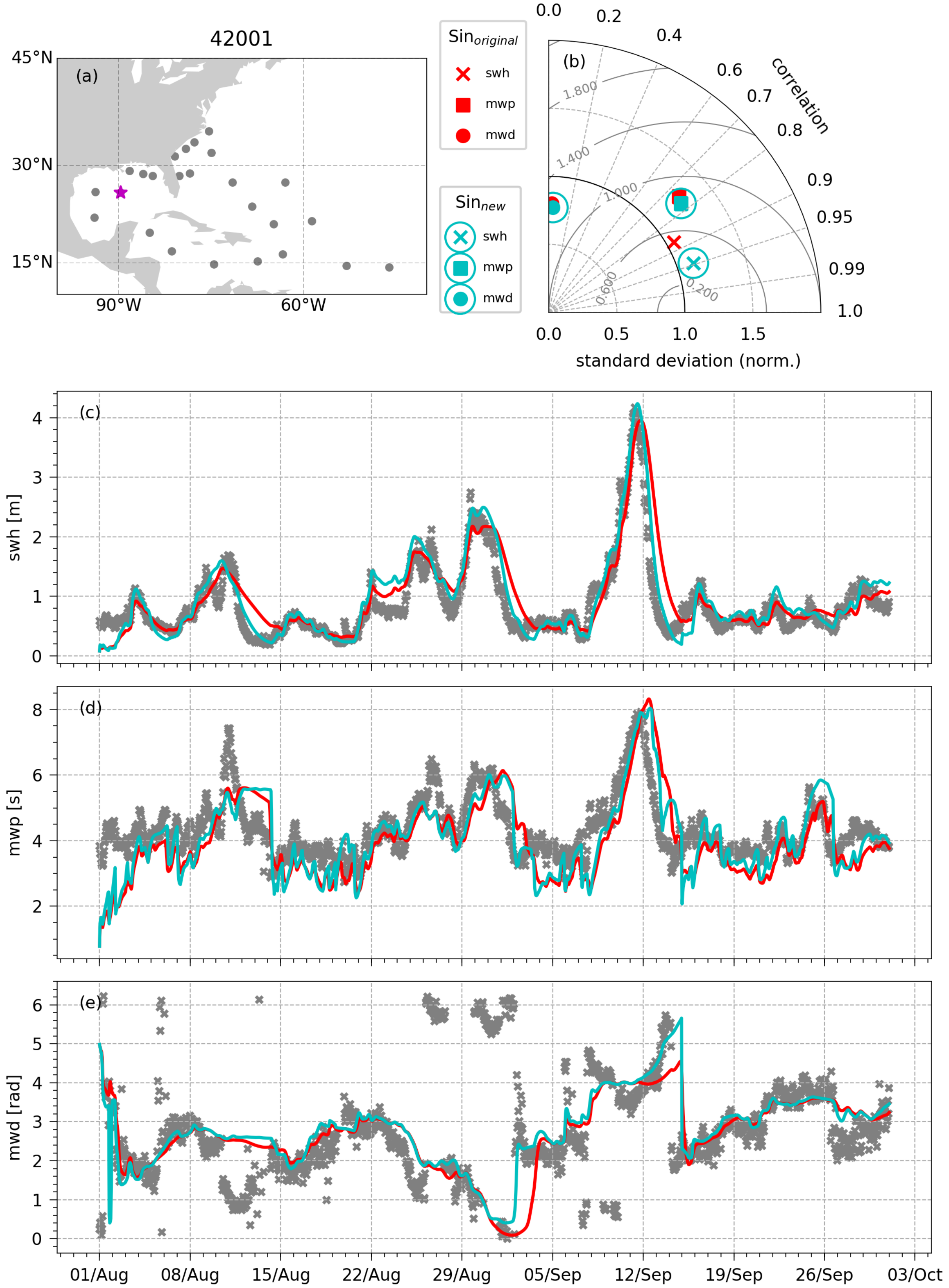

Figure 2.11: The (a) position of the NDBC buoy 42001 and the time series of the significant wave height, mean wave period and mean wave direction, (respectively c, d, e) and the Taylor Diagram of the results. Red (orange) colors indicate the results of the model with the original (new) wind input source function. The results are similar to what is observed in the other positions of the NDBC buoys in Gulf of Mexico. In order to calculate the statistics in the Taylor Diagram, only values after 15/Aug are used. The analysis was made in 2017.

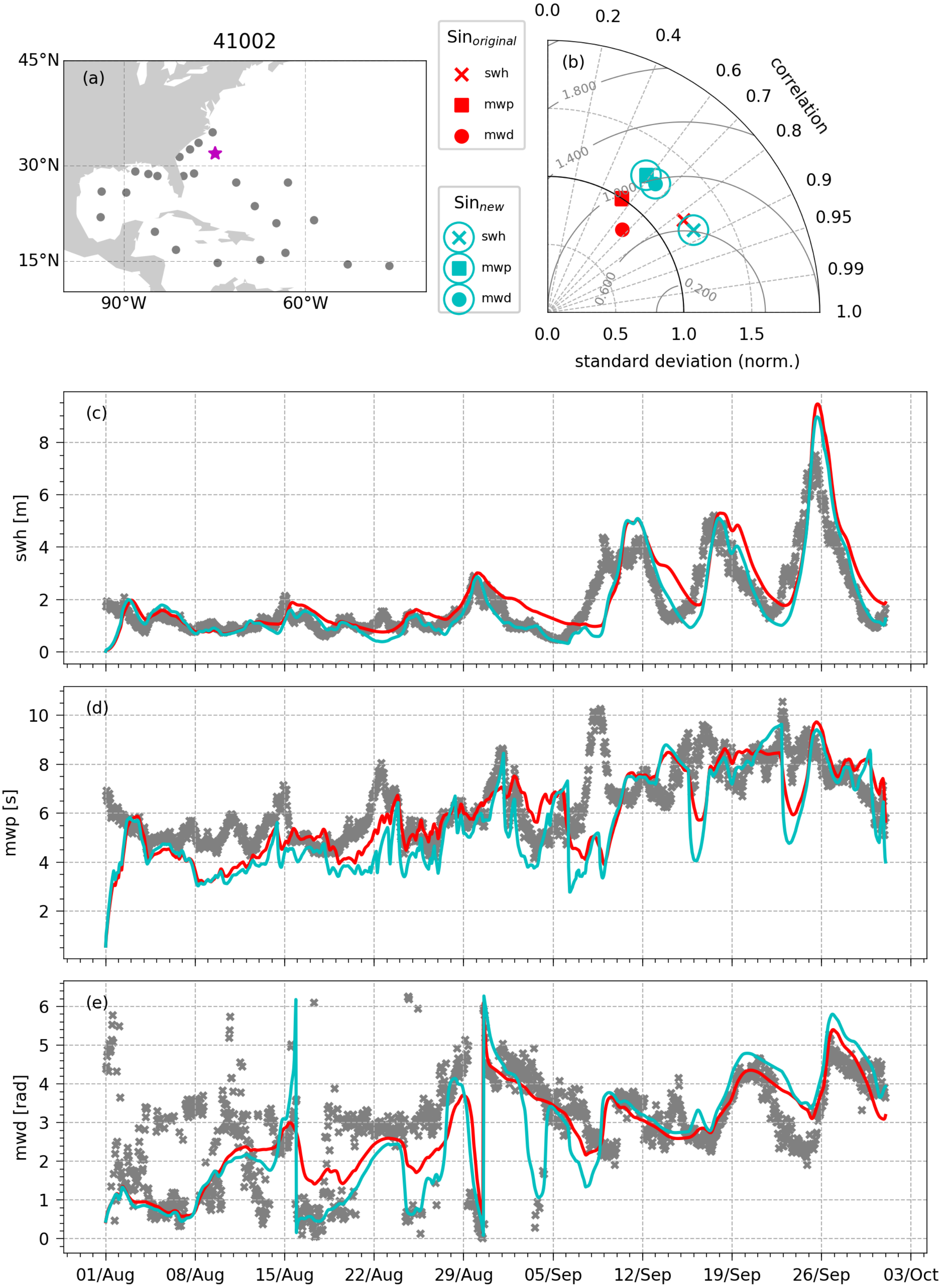

Figure 2.12: The (a) position of the NDBC buoy 42001 and the time series of the significant wave height, mean wave period and mean wave direction, (respectively c, d, e) and the Taylor Diagram of the results. Red (orange) colors indicate the results of the model with the original (new) wind input source function. The results are similar to what is observed in the other positions of the NDBC buoys in the eastern coast of USA. In order to calculate the statistics in the Taylor Diagram, only values after 15/Aug are used. The analysis was made in 2017.

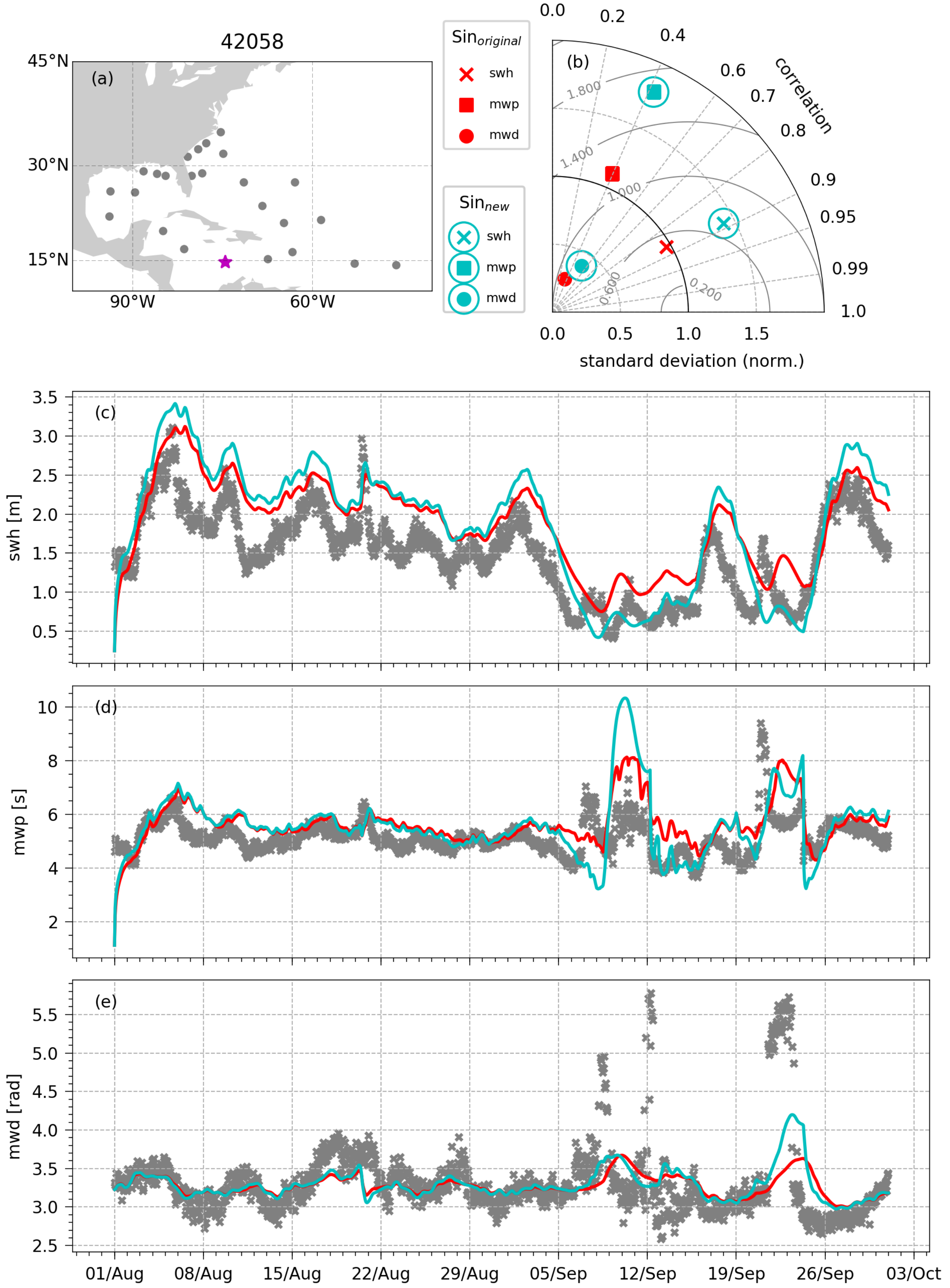

Figure 2.13: The (a) position of the NDBC buoy 42058 and the time series of the significant wave height, mean wave period and mean wave direction, (respectively c, d, e) and the Taylor Diagram of the results. Red (orange) colors indicate the results of the model with the original (new) wind input source function. The results are similar to what is observed in the other positions of the NDBC buoys to the south of Cuba.

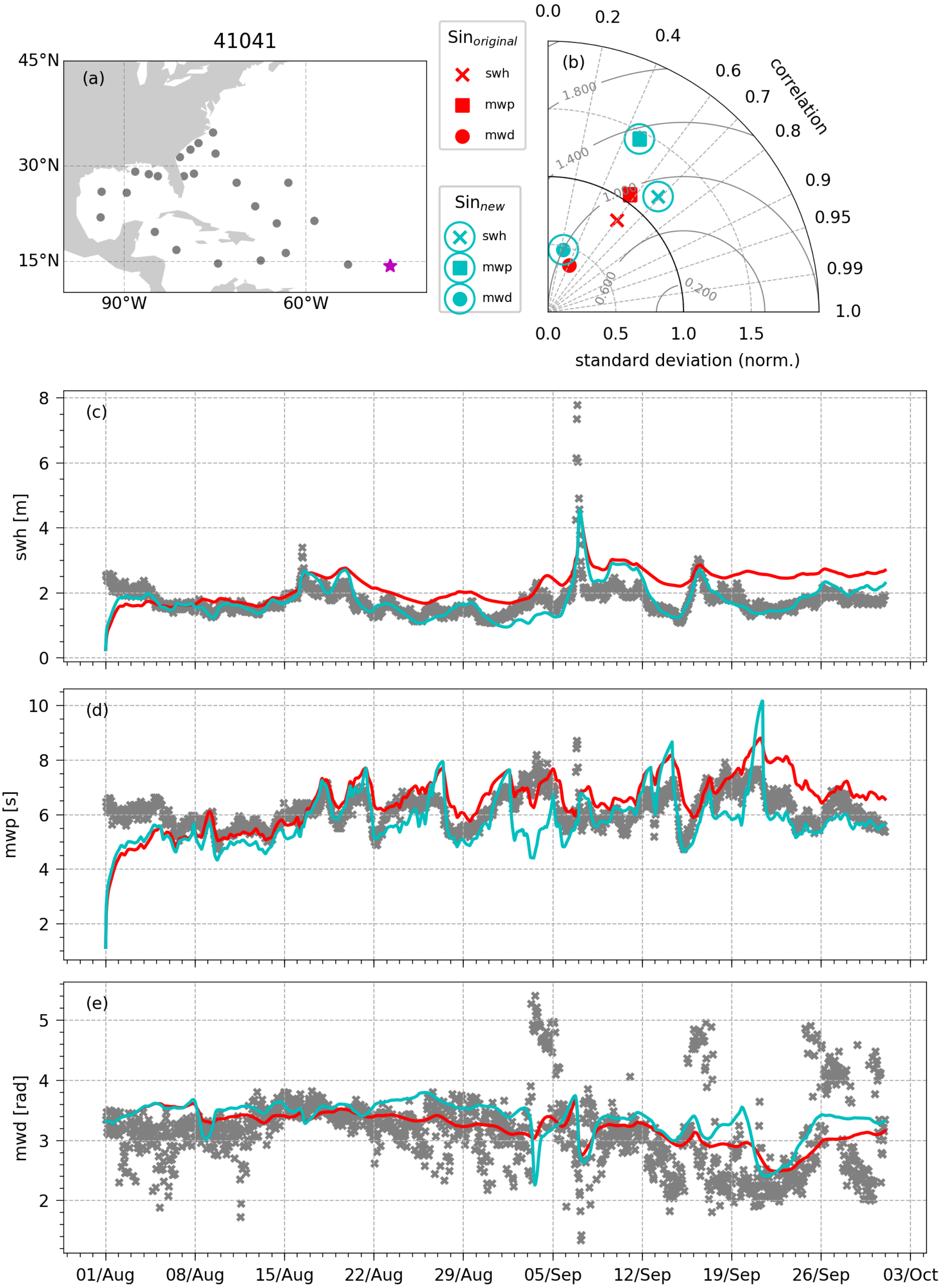

Figure 2.14: The (a) position of the NDBC buoy 41041 and the time series of the significant wave height, mean wave period and mean wave direction, (respectively c, d, e) and the Taylor Diagram of the results. Red (orange) colors indicate the results of the model with the original (new) wind input source function. The results are similar to what is observed in the other positions of the NDBC buoys in the tropical Atlantic. In order to calculate the statistics in the Taylor Diagram, only values after 15/Aug are used. The analysis was made in 2017.

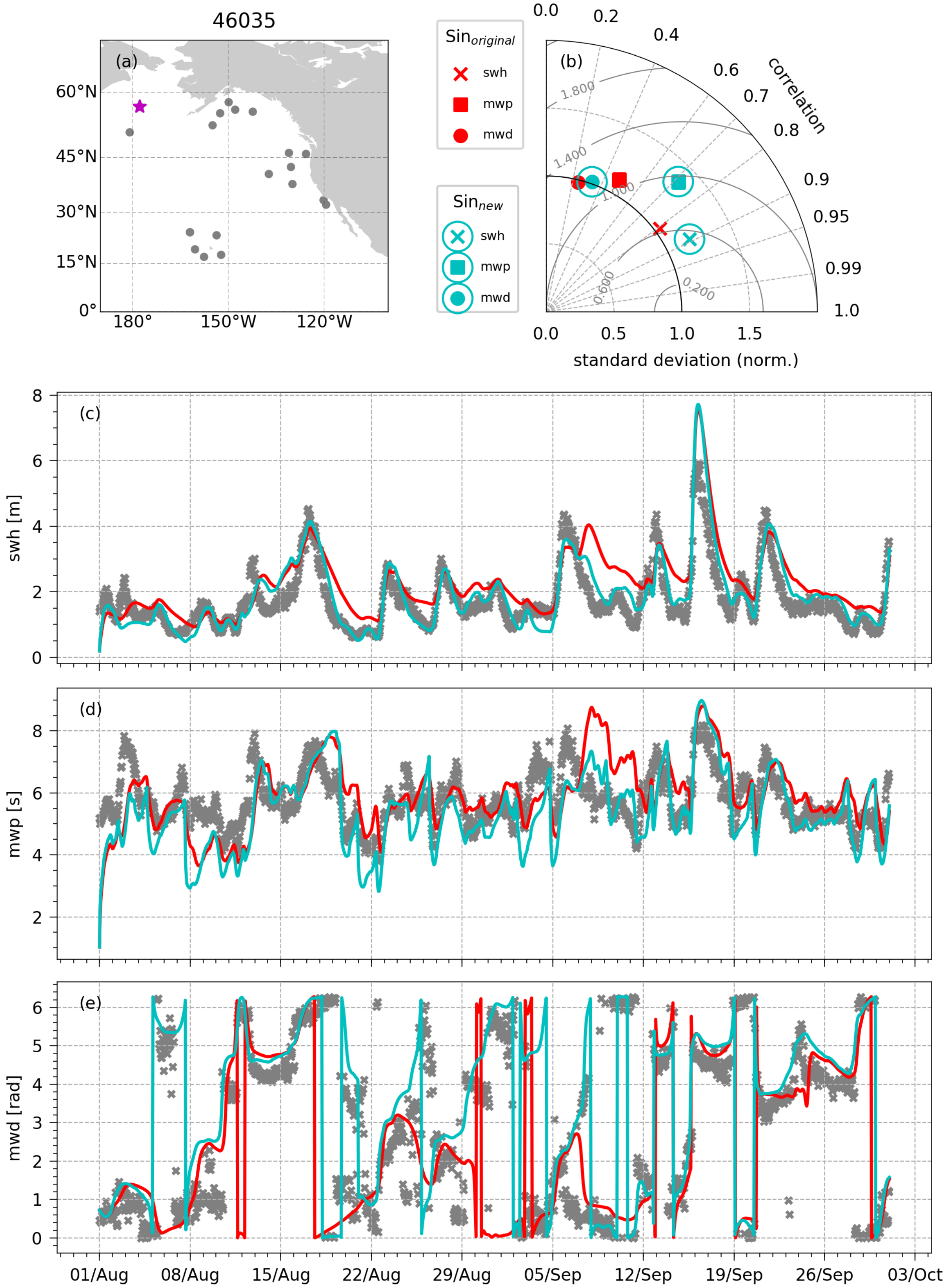

Figure 2.15: The (a) position of the NDBC buoy 46035 and the time series of the significant wave height, mean wave period and mean wave direction, (respectively c, d, e) and the Taylor Diagram of the results. Red (orange) colors indicate the results of the model with the original (new) wind input source function. The results are similar to what is observed in the other NDBC buoy in the Bering Sea. In order to calculate the statistics in the Taylor Diagram, only values after 15/Aug are used. The analysis was made in 2017.

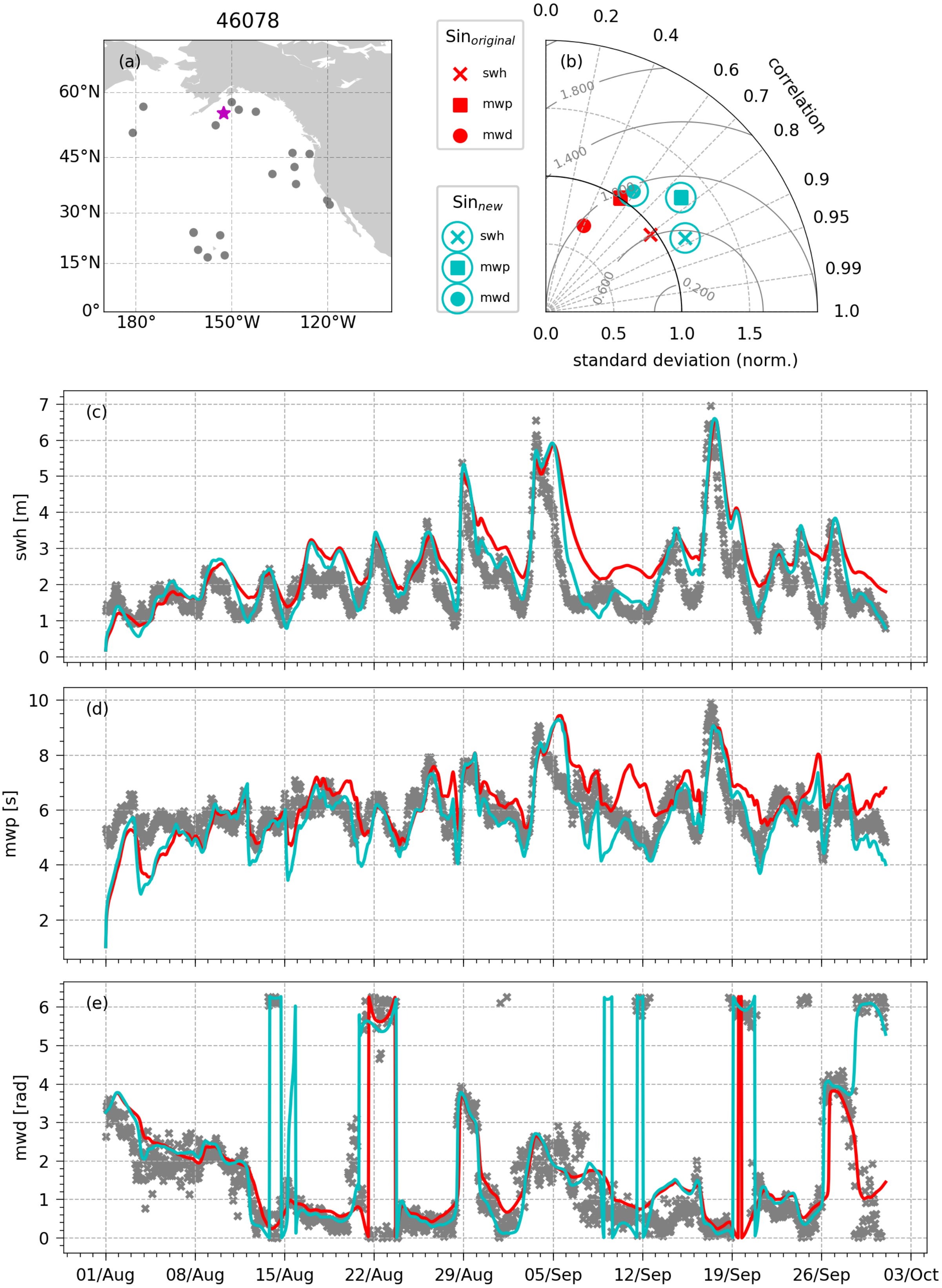

Figure 2.16: The (a) position of the NDBC buoy 46078 and the time series of the significant wave height, mean wave period and mean wave direction, (respectively c, d, e) and the Taylor Diagram of the results. Red (orange) colors indicate the results of the model with the original (new) wind input source function. The results are similar to what is observed in the other positions of the NDBC buoys in Gulf of Alaska. In order to calculate the statistics in the Taylor Diagram, only values after 15/Aug are used. The analysis was made in 2017.

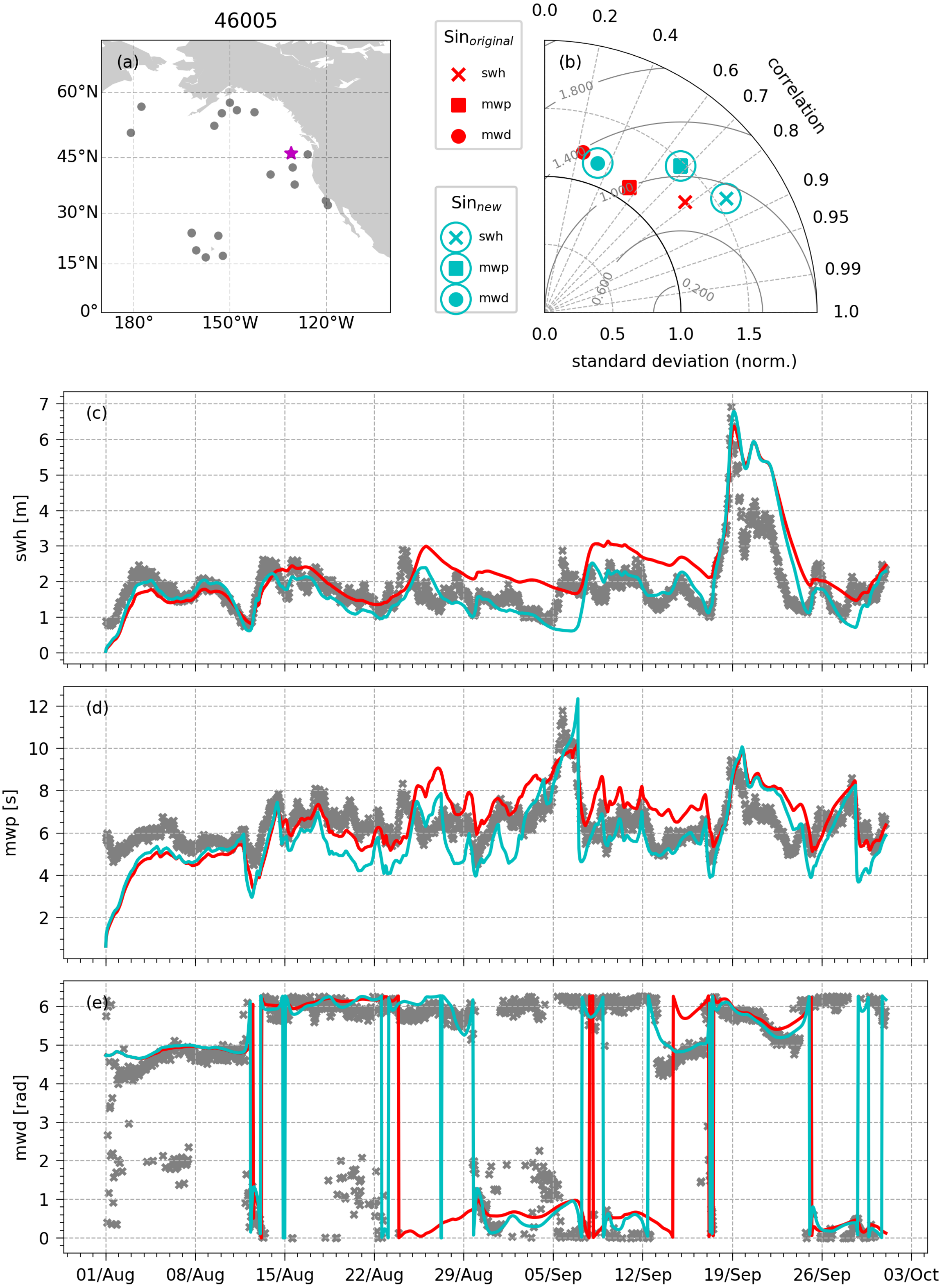

Figure 2.17: The (a) position of the NDBC buoy 46005 and the time series of the significant wave height, mean wave period and mean wave direction, (respectively c, d, e) and the Taylor Diagram of the results. Red (orange) colors indicate the results of the model with the original (new) wind input source function. The results are similar to what is observed in the other positions of the NDBC buoys on the western coast of USA. In order to calculate the statistics in the Taylor Diagram, only values after 15/Aug are used. The analysis was made in 2017.

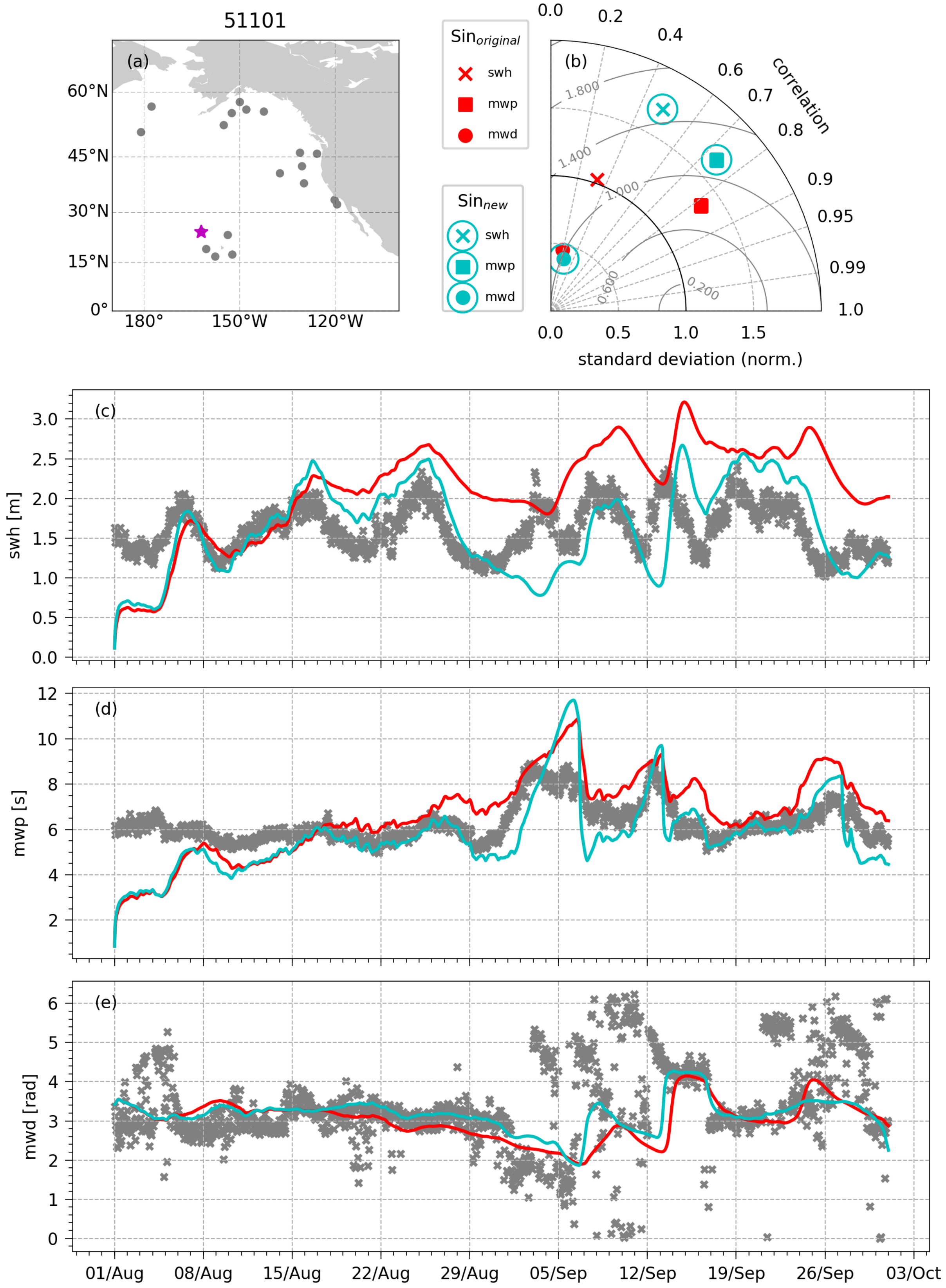

Figure 2.18: The (a) position of the NDBC buoy 51101 and the time series of the significant wave height, mean wave period and mean wave direction, (respectively c, d, e) and the Taylor Diagram of the results. Red (orange) colors indicate the results of the model with the original (new) wind input source function. The results are similar to what is observed in the other positions of the NDBC buoys around Hawaii. In order to calculate the statistics in the Taylor Diagram, only values after 15/Aug are used. The analysis was made in 2017.

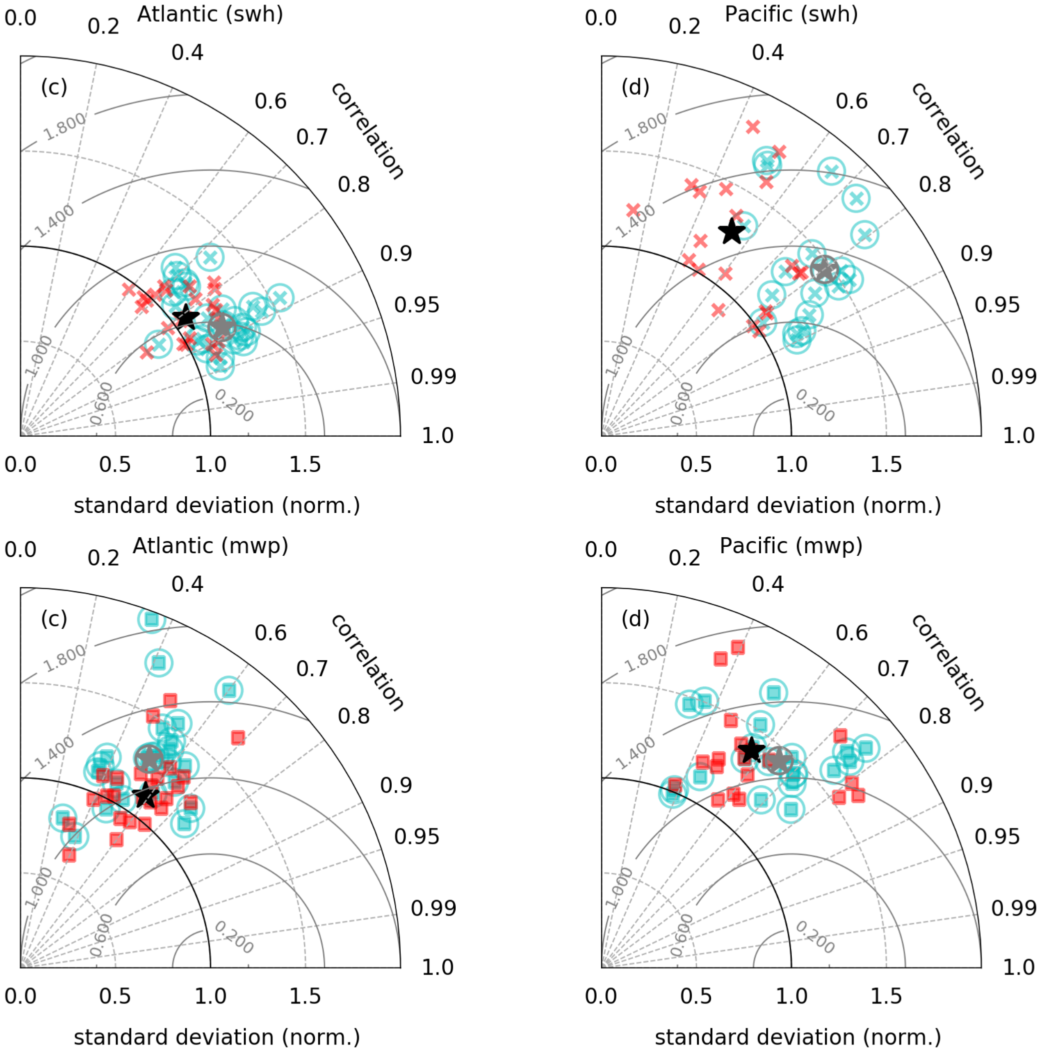

Figure 2.19: Taylor Diagram of (top panels) the significant wave height and (bottom panels) mean wave period in the (left panels) Atlantic and (right panels) Pacific.

deviation (the standard deviation of the model results is divided by the standard deviation of the observations). The stars indicate the median position of the cluster of points related to the model with the original wind input source function (black stars) and with the new source function (gray circled black stars). As the diagram reveals, changes in the wind input source functions improve the median correlation of the significant height from 0.5 to 0.8 (0.81 to 0.88) and the median standard deviation also increases from 1.3 to 1.4 (1.1 to 1.2) in the Pacific (Atlantic). The improvement related to the correlation values is clearly observed in the time series of the swh, where the original model overestimates measured heights below 3 meters in most of the NDBC buoy positions (2.11 to 2.16). Although the correlation values are generally higher in the Taylor Diagram, there is an increase of the σ_{norm} which could indicate the worsening of the quality of the wave model results.

Since Taylor Diagram does not show the values of the central tendency of the time series distribution, we supplement the information by providing boxplots of swh in Figures 2.20 and 2.21. They show that the mean swh in the new wind input source function has better results than the original source function, specially over the the swell pool zones in the Pacific, in the western coast of USA and Hawaii.

2.4 Conclusion

This study made two different experiments to evaluate the results associated to changes in the wind input source function of umwm and also the effect of implementing the lateral boundary forcing in umwm associated to a high resolution grid in the SW region of the South Atlantic. Testing the umwm with S_{don06} in a global grid allows an evaluation of the results in a more diverse set of sea wind and swell conditions that are not usual in the South Atlantic. For instance, the swell dominates the wave condition in Hawaii. Improvements of the results at this site mean that a relatively better simulation of the wave fields will happen, if there is an analogous wave field in the South Atlantic.

In the first experiment in both cases of Sin_{don12} and Sin_{don06} source functions, better results were generally observed in areas, such as the Gulf of Mexico and Bering Sea, where the swell does not dominate the surface wave variability. The original and updated model were tested in a global domain in some of the NDBC buoy positions and the results over NDBC buoys were classified into wind waves, swell and transition zones following Chen et al. (2002). The statistics of the comparisons between NDBC measurements and the model results revealed an improvement of the modeled swh in both the Pacific and the Atlantic basins and also of the mwp in the Pacific basin, when the Sin_{don06} source function was used.

The wind input source function Sin_{don06} improved the model results in terms of swh . This is particularly evident on the North Pacific and also in the Atlantic in terms of the median value, correlation and also normalized standard deviation (Figures 2.19, 2.21). This function includes the sea state into the wave equation and parametrizes the flow separation - a process that was represented solely in the wave stress calculation in the original model. The inclusion reduced the overestimation of values of the swh under 3m in the time series. Worst results were present on areas of swell pool such as the western

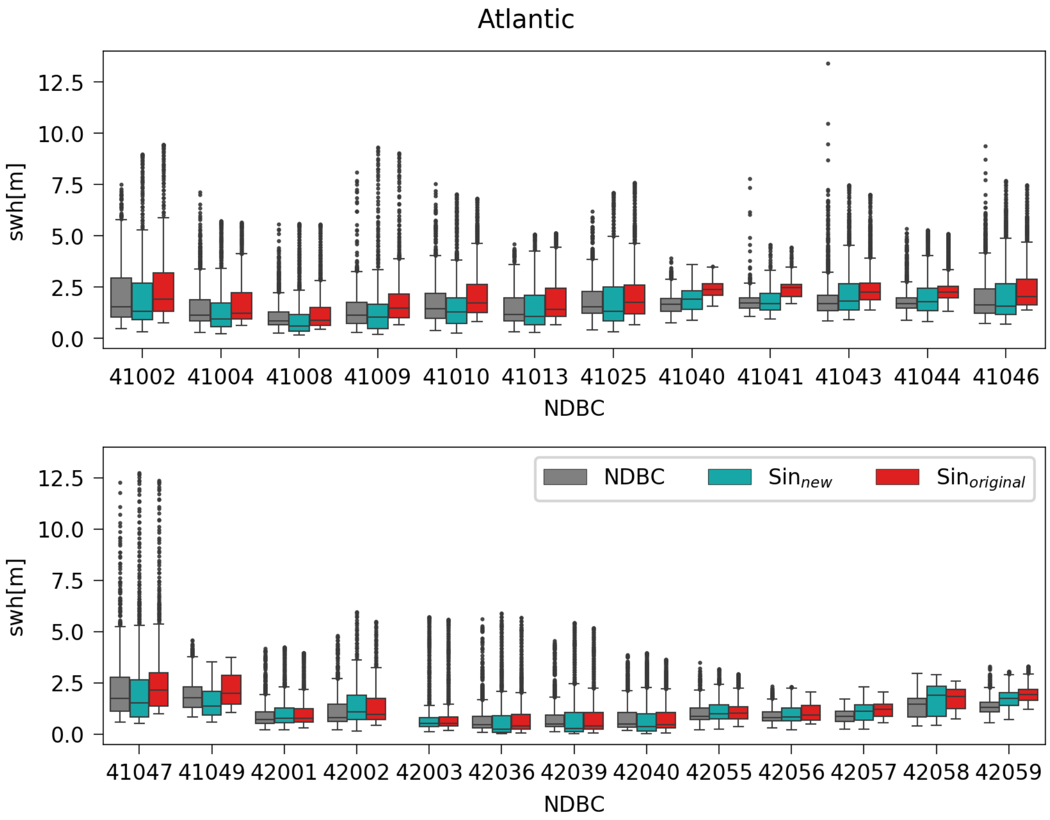

Figure 2.20: Boxplot comparisons between umwm results, with the original (red) and the new (orange) wind input source functions, and the NDBC buoys. The central tendency is the median,; box limits are the the first and third quartiles; inner fences are the 1.5 x the interquartile range; dots show values above the 1.5 x interquartile range. NDBC buoys of the eastern coast: 41002, 41004, 41008, 41009, 41013, 41025, NDBC buoys of the Tropical Atlantic: 41040, 41041, 41043, 41044, 41046, 41047, 41049, NDBC buoys of the gulf of Mexico: 42001, 42002, 42003, 42036, 42039, 42040, 42055, NDBC buoys of the South of Cuba: 42056, 42057, 42058, 42059,

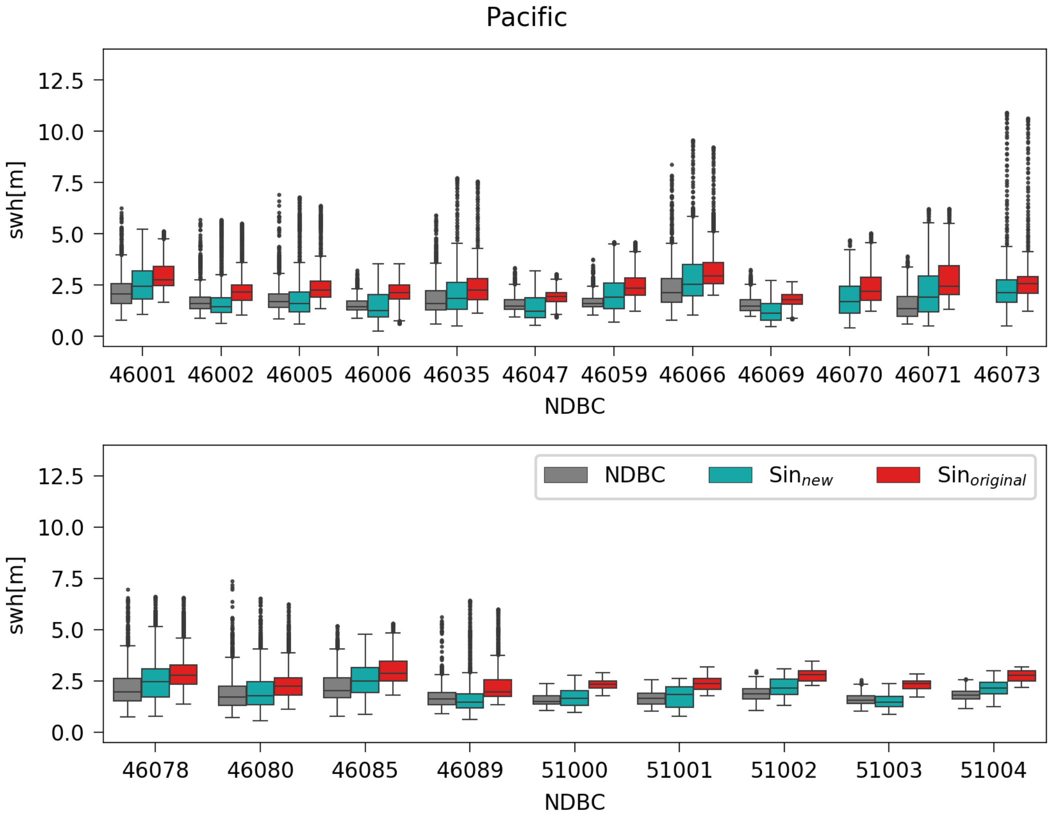

Figure 2.21: Boxplot comparisons between umwm results, with the original (red) and the new (orange) wind input source functions, and the NDBC buoys. The central tendency is the median,; box limits are the the first and third quartiles; inner fences are the 1.5 x the interquartile range; dots show values above the 1.5 x interquartile range.. NDBC buoys of the western coast of California are 46002, 46005, 46006, 46047, 46059, 46069, 46089, 46002, NDBC buoys of the Gulf of Alaska are 46001, 46004, 46066, 46078, 46080, 46085, NDBC buoys of the Bering Sea are 46035, 46071 and the buoys of Hawaii are 51001, 51000, 51003, 51002, 51004.

coast of USA and Hawaii, but S_{don06} improved the results in terms of both swh and mwp in the Pacific.

The nesting results needs further improvement, since the lateral boundary scheme introduce a lag in the propagation of the waves. Nevertheless, over shallow water (depth$< 50m$) the comparison of model results with Parana buoy observations suggest an overestimation of the dwp associated to the convergence of the energy in the spectrum due to changes of the group speed with the same frequency. Neither ww3 nor the coarse umwm present enough resolution to resolve local features as we observed in the fine model. The prediction of dwp in shallow water environment present a bias introduced by the non linear downshifting associated to the spilling breakers and shoaling.

In Chapter 3, the wave simulations use the original wind input source function of umwm. In Chapter 4, the wave simulations are computed with the S_{don06}.

3 INTERANNUAL VARIABILITY OF THE WAVES

3.1 Introduction

Waves generated by winds may enhance flooding and erosion, which affects both the environment and the nearshore population. This is an object of concern since changes in wave climate were observed in the oceans during the last decades. Satellite data (Young et al., 2011a,b) and regional wave measurements (e. g., Gulev and Hasse, 1999; Hemer et al., 2010; Gower, 2002) show increases in the significant wave height.

In the near future scenarios, wave generation areas such as the Southern Ocean may experience changes of wind speed with impacts in the significant wave height climate (Dobrynin et al., 2012). Future projections suggest that climate change will affect 60% of the global ocean by 2060 (Dobrynin et al., 2015) and it may also alter wave parameters, such as mean wave direction in some parts of the world (Wandres et al., 2017; Grabemann and Weisse, 2008). There is also a positive global trend of wind for values above the 90^{th} percentile, which implies in the increase of extreme events of wave height (Young et al., 2011a). Along the South American coast of the Atlantic, positive trends of significant wave height were found in areas corresponding to the continental shelf off Uruguay and Argentina between 32^{o}S and 40^{o}S (Dragani et al., 2010) and in the South Brazil Bight (SBB) (Alfredini et al., 2014), between Cabo Frio (23^{o}S) and Cabo de Santa Marta (28^{o} 40'S) (Figure 3.1).

The scientific community accepts the climate change as an unequivocal anthropogenic impact over the climate variability with a high probability of imposing negative implications to the coastal population (Pachauri et al., 2014). Observational time series length usually does not allow the separation of the anthropogenic and natural variability of waves (Dobrynin et al., 2015), which means trends are to be treated cautiously in climate analysis. For instance, the Southern Annular Mode (SAM) have been reported to shift into a

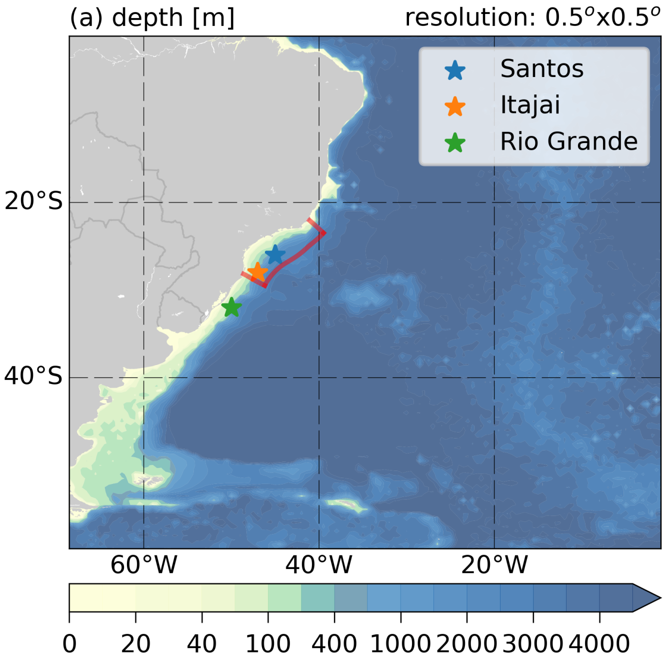

Figure 3.1: The southwestern Atlantic ocean is the domain of the wave simulation. The shaded contour represents the 1x1^o bathymetry used for the modeling. The position of the buoys is highlighted by the points. ETOPO-1 database provides the bathymetric information used in the model. The red contours represent the area of the South Brazil Bight.

positive phase (Marshall, 2003), but this trend is partially explained by natural variability and also by the human influence (Gillett et al., 2008).

SAM is the main mode of variability in the atmospheric circulation of the Southern Hemisphere. It is an annular structure of anomalous pressure with opposite signs between mid-latitudes and Antarctica and plays a relevant influence in the global climate. SAM modulates storm track interannual variability (Rao et al., 2003), which is directly related to wave generation through the winds associated with synoptic-scale systems. High phases of SAM are associated with a decrease of cyclone occurrence in the mid-latitudes (40^oS - 60^oS) and, an increase in the subtropics (20^oS - 40^oS) and high-latitudes (Simmonds and Keay, 2000; Reboita et al., 2009, 2015). This swinging behavior is caused by the relation of the SAM and zonal winds, which may promote changes in the vertical wind shear and static stability associated with baroclinic eddie growth rates (Rao et al., 2003). During the end of the last century, SAM showed a significant trend towards a positive phase associated with climate change and stratospheric ozone depletion (Marshall, 2003). In fact, the total number of cyclones has decreased in the mid-latitudes during the last decades (e.g. Simmonds and Keay, 2000; Fyfe, 2003). However, the number of intense cyclones (pressure at the center $\leq$ 980 hPa, Pezza and Ambrizzi, 2003) and “bomb cyclones” (at least 1 hPa per hour, Lim and Simmonds, 2002) has significantly increased in the Southern Hemisphere. Variations in the zonal wind intensity by SAM mechanism and its relation with cyclone development have affected the wave climate in the Southern Ocean (Hemer et al., 2010).

According to Sun et al. (2017), SAM has also a partial control over the position of the South Atlantic Subtropical High (SASA). In positive (negative) phases there is a southward (northward) displacement of the SASA within the Atlantic Basin. In La Niña years, when SAM is in its positive phase, the SASA tends to be displaced poleward. In El Niño years when SAM is in its negative phase, SASA tends to be displaced equatorward.

Subtropical Anticyclones and cold fronts may act together to define the wave climate of a specific region. For instance, in SBB both SASA and cold fronts associated with cyclones are relevant atmospheric features. The former influences SBB throughout the year mainly with E and NE winds and the last disturbs the region with three to five occurrences per month with S and SW winds (Castro and Lee, 1995). During summer, the observed wave height at SBB (26.5^oS,45^oW) typically ranges from 0.7m to 4.0m with mean values of

1.7 ± 0.7m and in winter the observed wave height ranges from 0.5m to 6.8m with mean values of 2.2 ± 0.8m Pianca et al. (2010).

Synoptic systems are capable of producing waves with a significant height higher than 5m in SBB (Innocentini and Neto, 1996) and are directly related to the presence of surface cyclones. Three main cyclogenetic regions over South America are responsible for the incoming cold fronts (e.g. Hoskins and Hodges, 2005). The cyclones generated in these regions usually move southeastward promoting intense surface winds along the South American coast. The preferential cyclogenetic regions are within the 50^oS-20^oS band: in the Argentina coast (45^oS), Uruguay and Northeastern Argentina (35^oS) and in Southeastern Brazilian Coast (30^oS) Hoskins and Hodges (2005). Cyclones and anticyclones variability over time may alter the wind and consequently the wave field. Over the last decades, the global number of cyclones has reduced, particularly in winter, although there was a positive trend in intense cyclone occurrences in specific regions. (e.g. Fyfe, 2003; Pezza and Ambrizzi, 2003; Lim and Simmonds, 2002).

In this chapter, we evaluate how the interannual variability of the significant wave height in the South Brazil Bight interacts with the large and synoptic scale atmospheric features, such as cyclones and the SASA. We test if SAM is a relevant forcing in interannual scale for the SASA and also evaluate the significant wave height trend in the region. We provide a description of wave model settings and validations in Section 3.2. Section 3.3 present the results, with the main focus on the empirical orthogonal function analysis (EOF) of the wind, 850-hPa of geopotential height, significant wave height datasets and the relation with SAM. It also presents a comparison between cyclone statistics and EOF analysis. Finally, we show the discussion and conclusion in Section 3.4.

3.2 Methods and datasets

3.2.1 The wave model

The University of Miami Wave Model (umwm) is a third generation wave model Donelan et al. (2012), which is used here to simulate the wave climate in the period between 1990 and 2004. This model solves the action balance equation, a description of the evolution of interacting weakly nonlinear waves. In his chapter, the original umwm formulation is employed.

3.2.2 Wind forcing

Two wave hindcasts encompassing different periods were produced: The first was forced by the 10m winds of the Climate Forecast System Reanalysis (CFSR; Saha et al., 2010) and the second with the 10m winds of the Operational Analysis of the Climate Forecast System Version 2 (CFSv2; Saha et al., 2014) between 1990-2004 and 2011-2017, respectively. Both datasets were produced by the National Centers for Environmental Prediction (NCEP). The CFSR is a validated benchmark in climate studies and has been used for past and future climate assessments Chawla et al. (2013). The wave model validation used the results forced by the CFSv2 10m winds and the wave results used in climate analysis were simulated using the CFSR forcing. Both wind databases are similar, though not entirely equivalent. Updates of the numerical code in the operational forecast may introduce artificial variability in the time series. The wave simulation forced by the operational winds is not employed in the long-term analysis, since the artificial variability may introduce extra errors to the results of the wave model. The available measurements of significant wave height in the region span the period 2011-2017 and this is the reason for the choice of the validation period. The wind fields were linearly interpolated to umwm's numerical grids.

3.2.3 Buoy measurements - PNBOIA moored buoy array

An array of moored buoys has measured meteo-oceanographic parameters in the Brazilian continental shelf since 2011. They are part of the Global Ocean Observing System and Brazil's National Buoy Program (PNBOIA). Among the entire data collection, three sites have better temporal availability. São Paulo, Santa Catarina and the Rio Grande do Sul buoy measurements (Figure 3.1) are used here for the validation of umwm simulation and will be called M01, M02 and M03 respectively. The buoy system is described in Pereira et al. (2017).

3.2.4 Model validation

Figure 3.2 presents a significant wave height simulation analysis. All three positions show a high correlation ($r > 0.8$) between the simulated and the measured data. An underestimation (overestimation) of the simulated parameter in the M01 and M03 (M02) occur and can be evaluated through the negative (positive) bias values, the qq-plot and

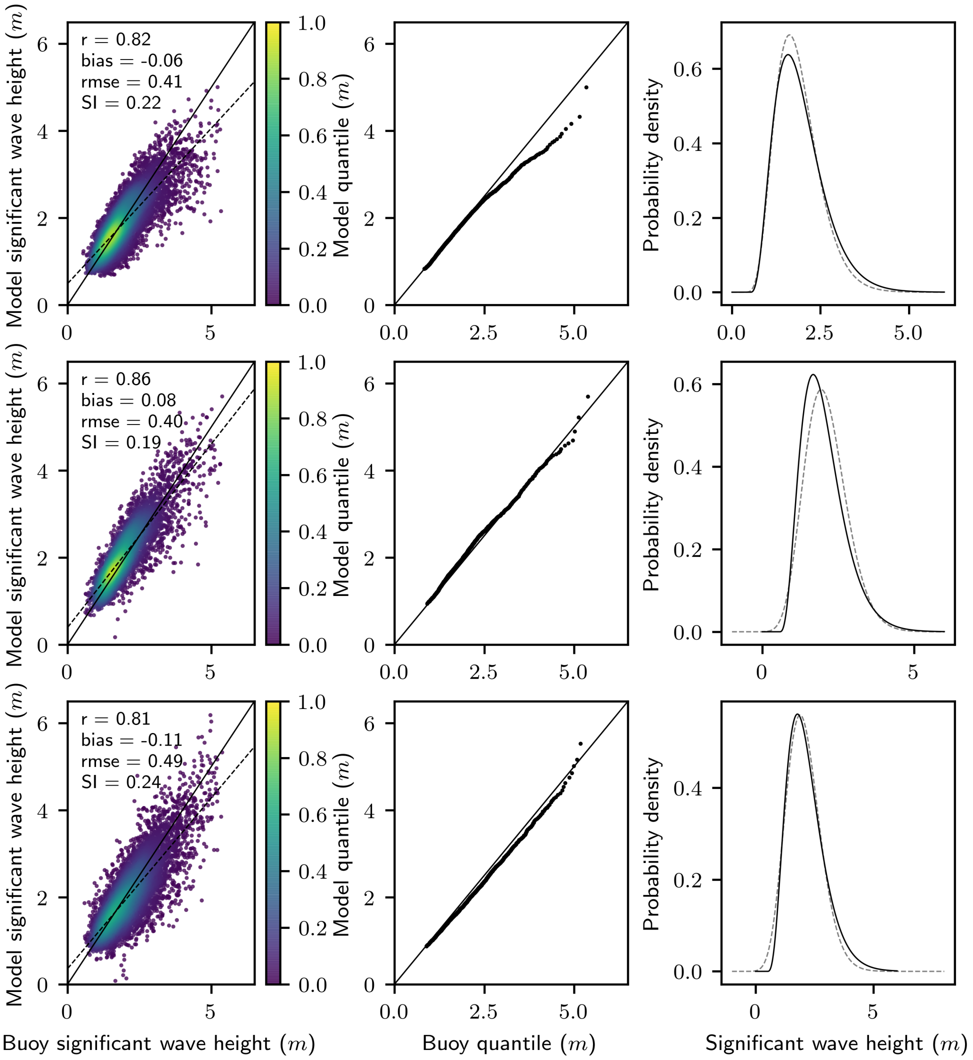

Figure 3.2: Distribution of simulated H_s in the SBB. The first column is the QQ-plot with observations (model results) in the x-axis (y-axis). The middle column presents the PDF of H_s the model (black) and the data (gray). The right column presents the histogram of the observed (dotted) and modeled (continuous line) significant wave height.

the probability distribution function (pdf).

In M01 the correlation between simulated and observed data has value of 0.82, showing a good agreement between observations and simulations. The pdf plot shows that most of the wave height values occur in the interval between 0.5m and 4m, and the qq-plot reveals a more accurate modeling for waves smaller than 2.5m. There is a negative bias of -0.06 and wave heights greater than 3m presented a difference to the observations of at most 1m. This last interval of wave height is less frequent, with probability density smaller than 0.1.

M02 has the highest correlation value (r=0.86) between modeled results and observations. There is a good agreement between the reference line and the quantiles in the qq-plot. In this case, deviations from the references present values of order 0.1m for events with wave heights greater than 4.5m. Significant wave heights between 1.5m and 2m have approximately 0.1 probability density higher occurrence than the observations in the pdf plot.

The correlation value in M03 between modeled and measured data has value of 0.81. This good agreement is also present in the qq-plot diagram and the pdf plot. In the first case, the negative bias of -0.11m is represented as a significant wave height underestimation with order smaller than 0.1m for intervals between 1m and 5m. The model underestimates and overestimates the occurrence waves with significant heights respectively smaller than 1m and greater than 4m - the absolute difference of the probability density is of about 0.05 for both cases.

3.2.5 Cyclone diagnostics

We used the cyclone tracking compiled by Gramcianinov et al. (2019) from the 6-hourly CFSR for the 1979-2010 period. The authors used the automated tracking system, TRACK (Hodges, 1994, 1995), which uses the relative vorticity field at 850 hPa computed from the zonal and meridional winds. The vorticity was truncated to emphasize the synoptic scales and only systems living at least 24 hours and displacing a minimum distance of 1000 km are taken into account. More details concerning the tracking and filtering method are found in Hoskins and Hodges (2002) and Hoskins and Hodges (2005), and the applied tracking constraints and thresholds for the South Atlantic Ocean are found in Gramcianinov et al. (2019). The use of vorticity instead of mean sea level pressure (MSLP; e.g. Murray and Simmonds, 1991) allows the detection of weak and fast moving synoptic systems, particularly between 40°S and 20°S, where they are masked by the strong surface pressure gradient (Sinclair, 1994). For the same reason, cyclones that do not have closed isobars are also identified, which is relevant to wave generation as long as these systems also generate significant winds. The spatial statistics (e.g. track density) are produced by the TRACK code using the spherical kernel method (Hodges, 1996).

A time series of cyclone occurrences and their anomalies are presented in Figure 3.3. The anomaly of the occurrence is calculated by subtracting the climatological monthly mean of the original series and applying a running monthly mean window, which filters the anomaly series (Figure 3.3b). We define the cyclone occurrence as the total of cyclones within a domain in a given instant of time. The selected domain for the cyclones counting was limited by the latitudes between 20^{o}S-40^{o}S in South Atlantic Ocean. Section 3.3.8 uses the cyclone occurrence anomalies time series in the evaluation of the SASA and waves variability.

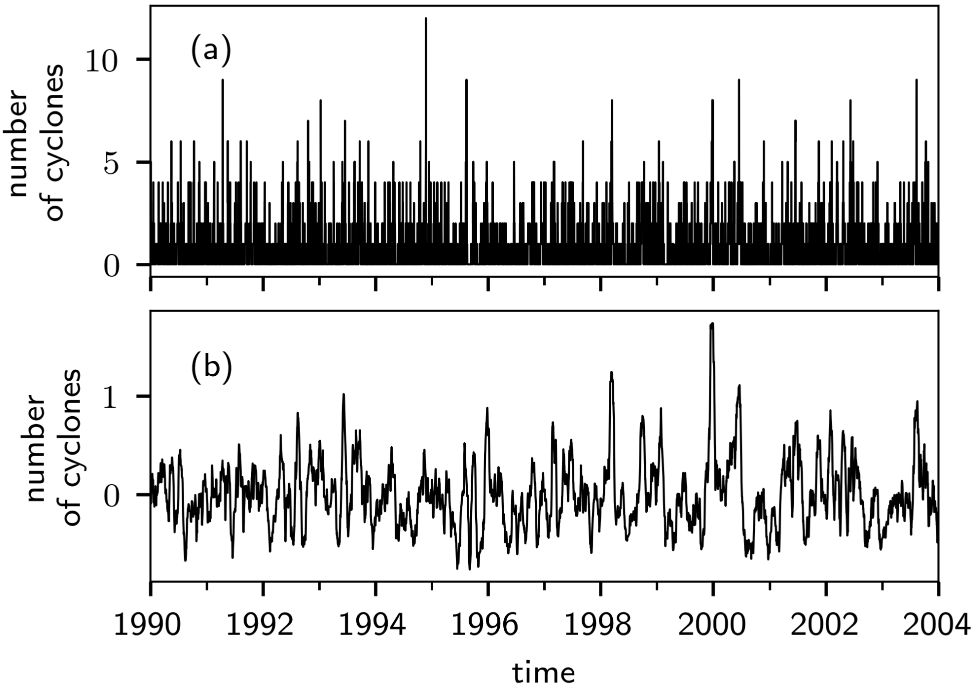

Figure 3.3: Time series of cyclone occurrences (a) and cyclone occurrence anomalies (b) between 20^{o}S-40^{o}S in the South Atlantic. The anomaly was filtered by a moving monthly average window.

3.3 Results

3.3.1 Wave propagation towards the South Brazil Bight

Figure 3.4 shows the cross-correlation between the significant wave height at a SBB reference point and the surface wind and the significant wave height at every point of the domain. These correlations will be hereinafter referred to as wind-correlated and wave-correlated fields. The correlations maps in Figure 3.4 present a lag of t=-48 hours, t=0 hours and t=48 hours.

The correlation maps show that the time series of significant wave height in the SBB has a local forcing associated with the wind and a remote component associated with the advection of the wave field. The wind-correlated fields (Figures 3.4a-c) show maximum values between 0.5 and 0.6 at t=-48 hours and t=0 hours, respectively. The spatial patterns in Figures 3.4a-c shows that correlations are greater in areas restricted to distances of approximately 5^o of the reference point, which suggests areas where the regional wind waves are important. Moreover, the prevailing wind systems with greater influence in the reference point are located near 30^oS (Figure 3.4a). The zonally elongated correlation pattern indicates also the influence of winds from the east.

On the wave-correlated fields at t=-48 hours (Figure 3.4d), values of correlation within 5^o of the reference point are larger than 0.7. These areas are generally under the influence of the same wind system and show an approximate concentric shape.

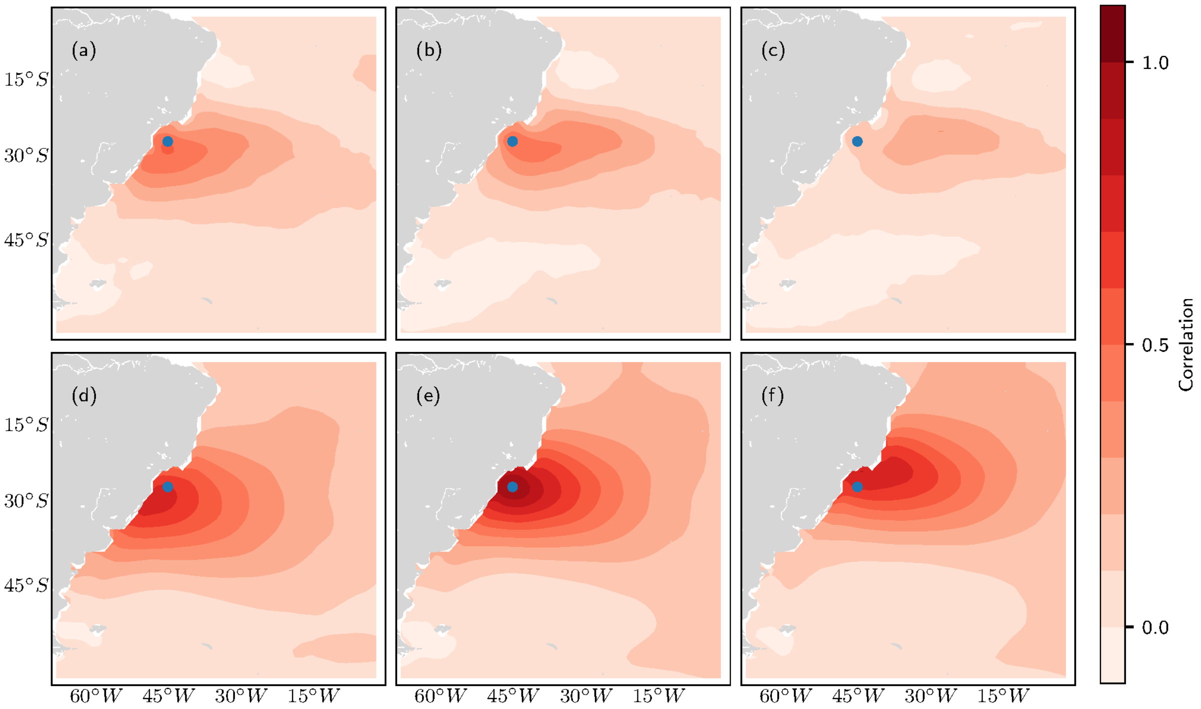

Figure 3.4: Map of correlation between the time series of the entire domain, relative to the reference point (blue dot). The upper (lower) panels the correlations of the leading time series of the significant wave height onto the wind (wave) fields at time lag of -48 hours (a,d), 0 hours, (b,e) and +48 hours (c,f).

Correlation values under 0.7 may be understood as the signal of the swell field which propagates across the reference point. At t=-48 hours, the swell from the S correlates better with the time series of the reference point than the swell from E and NE. At t=48 hours, the correlation fields are to the NE of the reference point. The asymmetry in correlation values shows that the swell propagates northeastward (Figure 3.4).

The center of the bands in both wave and wind-correlated fields show a displacement coherent with the time lag in the correlated fields - higher values of correlation move toward

N/NE, as the time lag value increases. This is in agreement with the regional wave climate description since the northward/northeastward waves are approximately 1m higher in the SBB when compared with the westward component, which is the second most important direction of the waves (Pianca et al., 2010).

Easterlies associated to the SASA also influence the wind and wave-correlated fields. Deviations from the concentric zonal bands at approximately 15^{o}S and 15^{o}W (t=-48 hours) in the wave-correlated fields are explained by easterly wind forced waves, which propagate towards SBB. Wave and wind correlated fields show that the wave observed fields in the SBB are generated mainly in the southwestern Atlantic between approximately 20^{o}S - 40^{o}S and 55^{o}W-20^{o}W. Wind systems southward of the SBB are known to be cold-front related (i.e., extra-tropical cyclones), whereas to the north of the reference point the easterlies prevail.

3.3.2 *Significant wave height and wind annual climatology*

In order to better interpret the empirical orthogonal function analysis over wave and wind fields (Section 3.3.3 - 3.3.6) we present climatological fields. Figure 3.5 shows the annual climatology of the significant wave height, meridional and zonal wind fields. The histograms of these variables (not shown) show an approximately normal distribution, where the mean axis is a good representation of central values. There is a southward increase of the significant wave height gradient, and the significant wave height has approximate value of 1.5 ± 0.6m and 4 ± 1.4 m in the northern and southern edge of the domain, respectively (Figure 3.5a).

Easterlies (westerlies) occur in the north (south) of the domain with mean values of -3.5 ± 3.2 m s^{-1} (3.0 ± 5.6 m s^{-1}). Figure 3.5c shows the meridional wind climatology, which is influenced by the western edge of the SASA. The southward wind intensity reaches a maximum of -4.0 ± 5.6 m s^{-1} at approximately 25^{o}S. The southern part of the domain presents weak positive meridional wind values of 0.5 ± 6.4 m s^{-1}.

3.3.3 *Empirical Orthogonal Function Analysis*

An Empirical Orthogonal Function (EOF) analysis (Dawson, 2016) was performed on the fields of significant wave height, 850-hPa geopotential height and the components of the 10m wind speed anomaly. We calculate anomalies by subtracting the seasonal cycle

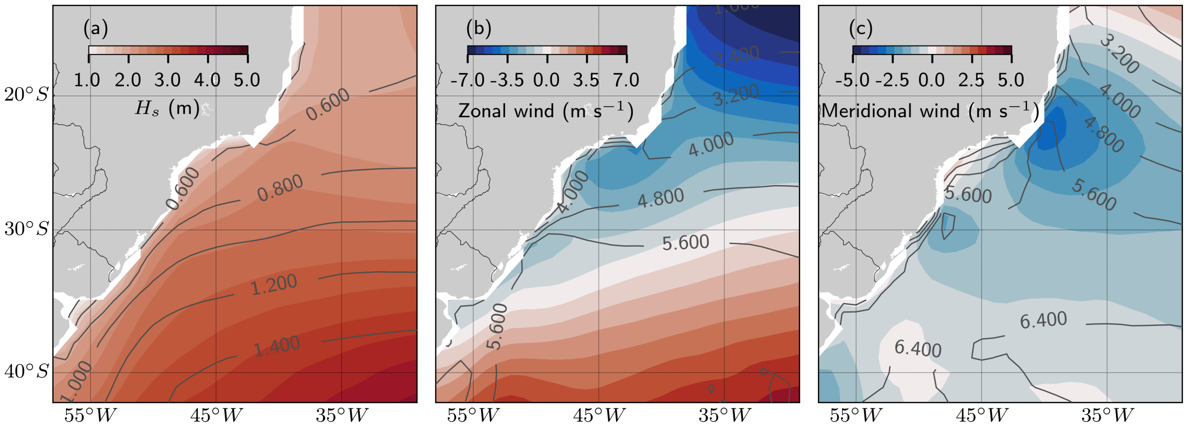

Figure 3.5: Annual climatology of (a) significant wave height, (b) zonal wind and (c) meridional wind. The average and standard deviation fields are represented respectively by shaded colors and contours.

from the original signal. A non-linear least square method was used to fit a sinusoidal curve to the seasonal signal at every grid point with the frequency, phase and amplitude being provided by a discrete Fourier Transform and the standard deviation of the time series. A hamming window of 11 months removed the high-frequency variability of all principal components of the EOF analysis.

North et al. (1982) suggests that the EOF analysis would be able to identify "true" modes only from infinite samples. Thus, the author suggests a "rule-of-thumb" to assess sampling errors when estimating shapes of a "true" EOF with a finite amount of data. Here, North's "rule" (not presented) suggests that the calculated modes are not completely distinguishable among themselves. This is expected since the studied processes are regional and thus, should not show up as true modes of variability.

Figures 3.6 and 3.7 show the EOF fields of the geopotential height, significant wave height, zonal and meridional winds. Although the test suggest that modes are not distinguishable, the analysis of the results in the next sections reveals physical meaning and coherence between the different modes.

It is fundamental to notice, that the positive or negative signal of anomalies doesn't necessarily show the direction/intensity of the real field, but the strengthening or weakening of values relative to the annual signal.

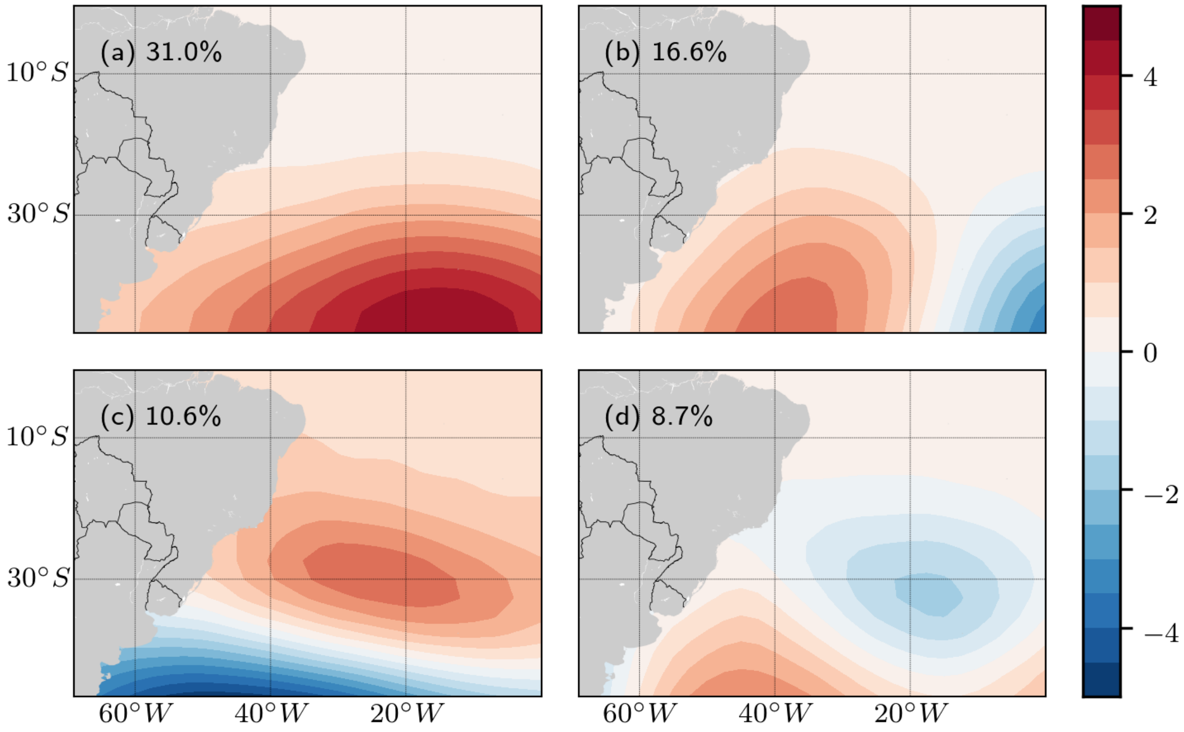

Figure 3.6: The (a) first, (b) second , (c) third and (d) fourth empirical orthogonal function of the 850-hPa geopotential height. Each map is divided by its own standard deviation.

3.3.4 Variability of the SASA and large scale zonal wind

Figure 3.6a shows the EOF1 the 850-hPa geopotential height and Figure 3.7c presents the EOF1 of the zonal wind. Both consist of monopoles southward from 30^{o}S. A high correlation (r=0.72) between the modes and the spatial pattern distribution indicate they are coupled together through geostrophic balance. The monopole of the EOF1 of zonal wind is located over the meridional gradient of the EOF1 of 850-hPa geopotential, configured as the geostrophic wind.

The variability of the EOF1 of geopotential height is related to the expansion (contraction) of the SASA which generates anomalies on the zonal wind field. In other words, positive (negative) anomalies of the 850-hPa geopotential height EOF1 relates to the south-north contraction (expansion) of the SASA and are associated with westward (eastward) anomalies of the zonal wind southward of 30^{o}S, within the westerlies zone. Thus, the meridional variability of the SASA affects directly the transients development, as long as it influences the wind intensity in cyclogenesis areas.

Figure 3.6d shows the 850-hPa of geopotential height EOF4, which appears as a dipole structure. It represents the meridional shift of the SASA and its principal component show a correlation of 0.67 with the SAM index. When negative (positive) phases of SAM are present, negative (positive) anomalies of the 850-hPa geopotential height occur, which results in a southward (northward) shift of SASA. This variability is related to SAM and was also reported in previous studies (Sun et al., 2017; Thompson et al., 2000). The meridional variability of the SASA (EOF4 of the 850-hPa geopotential height) is also related with the EOF1 of zonal wind, (Figure 3.7c) through geostrophic balance. This is indicated by the spatial patterns of the EOFs and also by the correlation between the principal components (r=-0.51) of both modes. When the values of the EOF4 on the northern section show positive (negative) anomalies, the zonal wind usually presents positive (negative) anomalies. In this way, positive (negative) anomalies of the EOF4 of 850-hPa geopotential height represents a more intense (weak) SASA, which reflects in an intensification (weakening) of the westerlies southward of 30°S, impacting the cyclone occurrence in the Atlantic as explained before.

3.3.5 Geostrophic balance between the four EOF of 850-hPa and the zonal and meridional winds EOF1

The EOF1 of meridional wind (Figure 3.7d) correlates moderately (r=-0.53) with the EOF4 of 850-hPa of the geopotential height. Positive (negative) anomalies of the geopotential height intensify (weaken) southward anomalies of the geostrophic meridional wind. This is expected due to the intensification of SASA.

Figure 3.6b shows a zonal dipole of the EOF2 of 850-hPa geopotential height. It couples geostrophically with the EOF1 and EOF2 of respectively zonal and meridional wind, but with a smaller intensity (r=0.39 and -0.46, respectively). When the eastern section of EOF2 of 850-hPa geopotential height is positive (negative), the anomalies related to the EOF1 of zonal wind show positive (negative) values. This forcing may be related to the zonal shift of the SASA.

EOF3 of the 850-hPa geopotential height is presented in Figure 3.6c. It consists of a meridional dipole and it is in geostrophic balance with the EOF1 of zonal wind. There is a moderate value of correlation (r=-0.46) between the principal components (PC) of both modes. When the eastern section of the EOF3 of 850-hPa geopotential height presents positive (negative) anomalies, the meridional wind anomaly associated with the EOF1 of meridional wind shows southward (northward) values.

3.3.6 EOF of winds and EOF of significant wave heights

Figure 3.7a show the EOF1 of significant wave height. It appears as a monopole to the south of 20^{o}S, centered approximately about 40^{o}S. The principal component of EOF1 of significant wave height correlates moderately with the EOF1 (r=0.55) and EOF4 (r=0.41) of the 850-hPa of the geopotential height. The SASA meridional expansion and zonal shift described by the EOF1 and EOF2 of 850-hPa geopotential height (Sections 3.3.4, 3.3.5) is associated with the contraction (expansion) of the SASA and induces negative (positive) anomalies in the wave field related to the EOF1 of the significant wave height. The PC of the zonal wind shows a better correlation with the EOF1 of significant wave height (r=0.62). Wave fields show spatial patterns consistent with respect to both wind and geopotential height modes. Negative (positive) anomalies of westerlies associated with the EOF1 of the zonal winds force negative (positive) anomalies on the wave field related to the EOF1 of the significant wave height.

EOF2 of significant wave height is presented in Figure 3.7b. A dipole characterizes the wave field of the EOF2 of significant wave height and it correlates significantly with EOF1 of the zonal wind (r=-0.86). Meridional contraction (expansion) of the SASA forces positive (negative) anomalies in the EOF2 of the significant wave height. The meridional shift to the north (south) of the SASA is linked to positive (negative) anomalies of the EOF2 of the wave height. Reconstructed fields show that when EOF1 of zonal wind presents negative anomalies in the wind field, it forces negative anomalies of the significant wave height in the northern region of the dipole (Figure 3.7b). On the other hand, positive anomalies of the zonal wind are associated with positive anomalies of the significant wave height. This mode also shows to be influenced by cyclones in the interannual scale, as we show in Section 3.4.

3.3.7 Expansion/contraction and meridional shift of the SASA and its implication to the westerlies anomalies variability and the significant wave height

Figure 3.8 shows the principal components of the EOF1 and EOF2 of 850-hPa geopotential height, the EOF1 of the zonal wind and the EOF2 of the significant wave height.

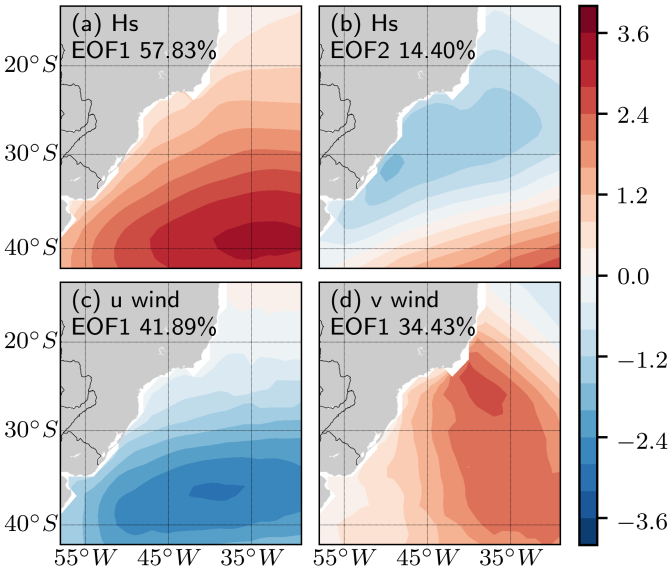

Figure 3.7: First (a) and second (b) EOF of the significant wave height and first EOF of zonal (a) and meridional wind (b).

An out-of-phase signal appears between both geopotential height modes, which affects the EOF1 of zonal wind. The EOF1 of 850-hPa geopotential height accounts for an expansion (contraction) "mode" of the SASA, while the second shows the meridional displacement "mode" of the SASA. The meridional shift "mode" and the intensity "mode" of SASA suppress each other from 1997 onward, according to the reconstructed fields of the EOF1 and EOF4 of 850-hPa geopotential height (not shown). EOF1 and EOF2 of the 850-Pa geopotential height anomaly force the EOF1 of zonal wind and ultimately the EOF2 of the significant wave height.

3.3.8 The interannual effect of Subtropical South Atlantic Anticyclone over Cyclones and Waves

Figure 3.9 shows the storm track density during positive and negative phases of the EOF1 of zonal wind. The density of track was computed using only cyclones that developed within the cyclogenesis regions along South America (Gramcianinov et al., 2019).

There is a moderate correlation between the principal component of EOF1 of zonal wind and the time series of cyclones occurrence (r=-0.53). Cross-correlation analysis shows that the EOF1 of the zonal winds leads the cyclones occurrence by one month. Negative (positive) anomalies related to the EOF1 of the zonal wind field weaken (intensify) westerlies, which reduce (enhances) cyclonic activity on the study domain. 45% (55%) of the total

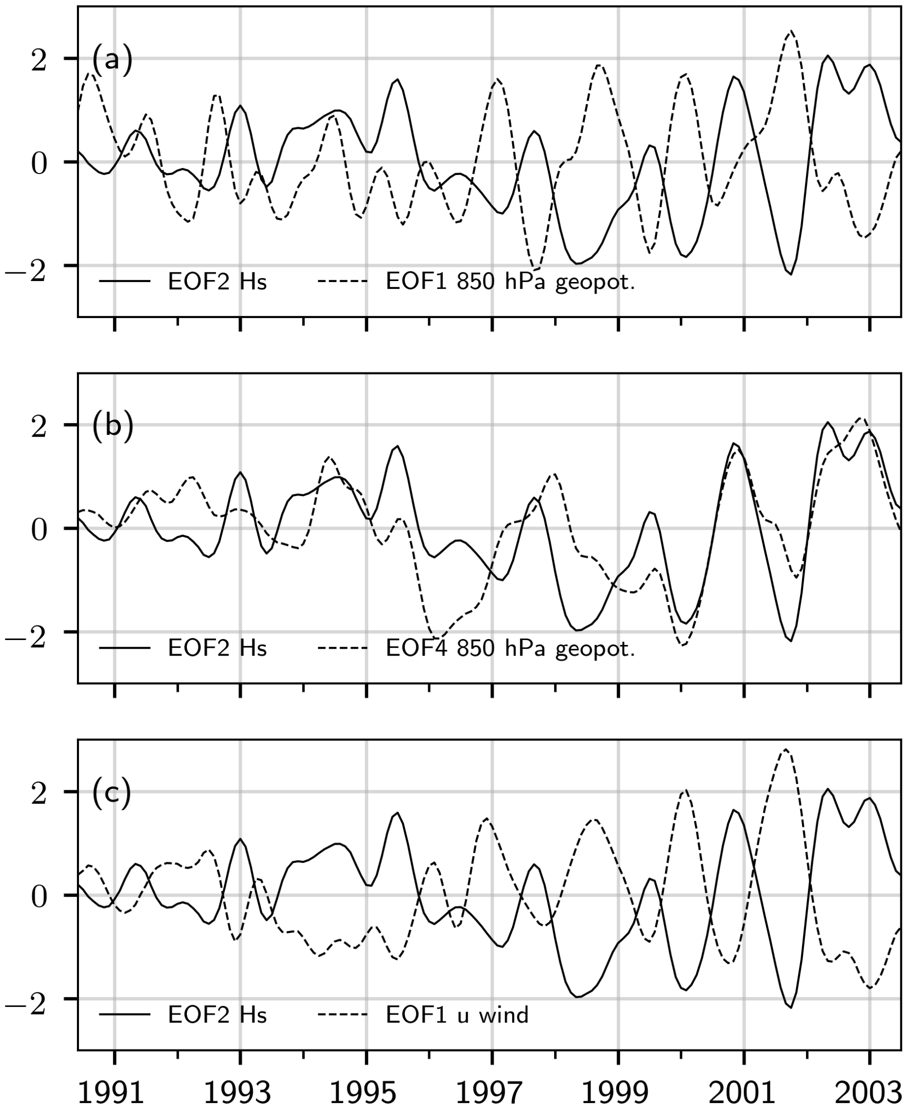

Figure 3.8: Principal components of (a) the EOF2 of significant wave height and EOF1 of 850 hPa geopotential height, (b) EOF4 of 850 hPa geopotential height, (c) EOF of zonal wind. All the results are normalized by the respective standard deviation.

number of cyclones identified occur during negative (positive) phases of EOF1 of zonal wind. This variation can be seen in Fig 3.9, which shows a higher track density during the positive phase of EOF1 of zonal wind. The track density reflects the cyclones paths during their displacement across the South Atlantic. As discussed before, the positive (negative) phase of EOF1 of zonal wind is related to the expansion (contraction) of SASA which means that those processes may modulate the occurrence of cyclones and the cyclogenesis in the Southwestern Atlantic through their influence in the westerlies.

The occurrence of cyclones is associated with the wave signal along the southeastern

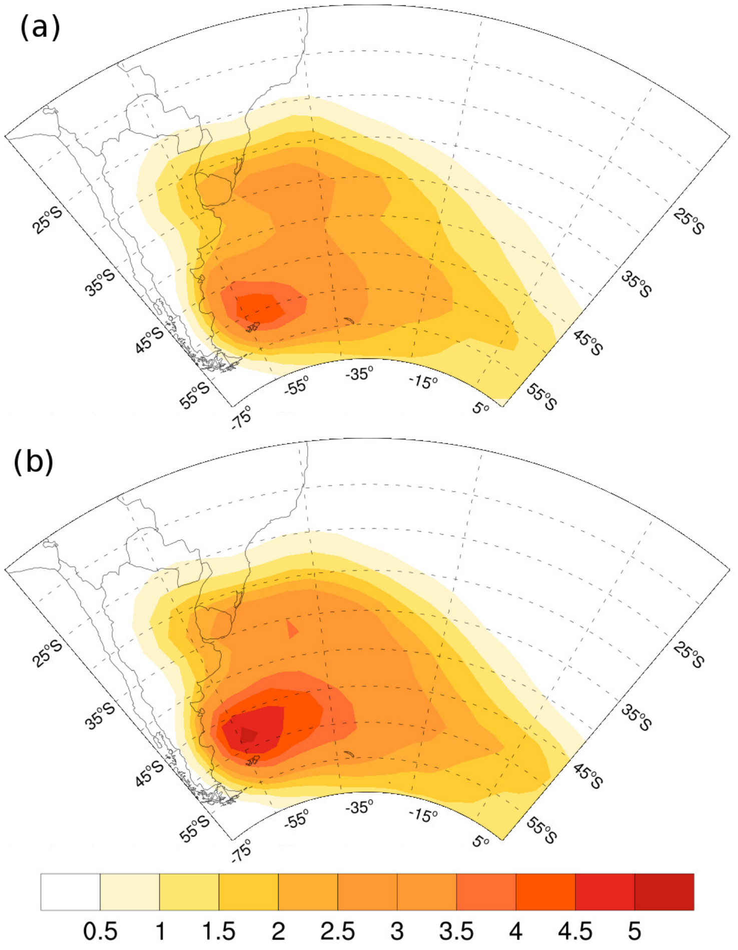

Figure 3.9: The cyclone track density computed for (a) negative and (b) positive phases of the EOF1 of zonal wind. The density unit is cyclone per $10^6 km^2$ per month.

Brazilian coast in the EOF2 of significant wave height (Fig 3.7b). This is also confirmed by moderate correlation values (r=0.51) between the cyclones occurrence and the PC of the EOF2 of the significant wave height. This is an evidence of the influence of the South American cyclones forcing wave variability along the southeastern Brazilian coast. Thus, high cyclone track density (Figure 3.9) is tied to positive anomalies of the EOF2 of the significant wave height (Figure 3.7b) on the southeastern Brazilian coast.

3.3.9 Long term trends

Figure 3.10 presents trends of significant wave height in the SBB and wind fields in the Southwestern Atlantic. The tendencies were calculated using linear regression and their significance was computed by the Mann-Kendall trend test citepMann1945. Values of wave and wind parameter were extracted from the original time series at each point of the grid. This wave analysis was performed only in the SBB region, where the model was

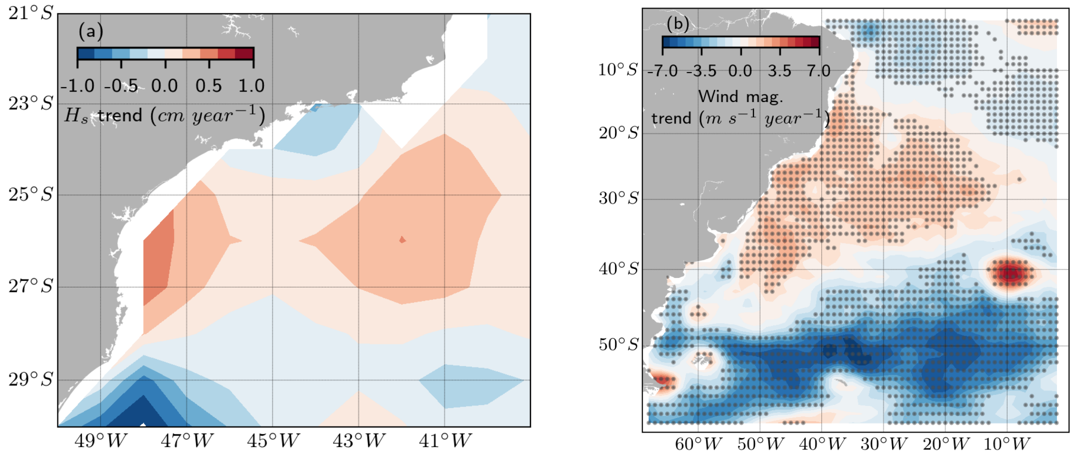

Figure 3.10: Trends of (a) significant wave height and (b) wind magnitude. Black dots represent areas where the trend is significant according to the Mann-Kendall trend test.

validated. However, as we showed in this work, the area of the wind analysis covers all the Southwestern Atlantic due to its importance to the regional wave climate.

Mann-Kendall test does not show significance in the trend of the wave height in the continental shelf, although positive trends up to 0.6 cm year^{-1} occur in the SBB domain (Figure 3.10a). These values have the same order of magnitude of previous studies estimations of Alfredini et al. (2014), who found an increase of approximately 0.4m in 40 years. Maximum values occur approximately at 26^{o}S and west of 48^{o}W and also at 26^{o}S and 42^{o}W. Over the entire period, the maximum increase of the significant wave height within SBB is of approximately 7cm.

The spatial distribution of the wind trend shows three zonal bands (Figure 3.10b), which correspond to the tropical, subtropical and subpolar regions. Both tropical and subpolar areas show negative trends of wind magnitude, while the subtropics present positive values.

3.4 Summary and conclusions

We demonstrate the existence of interannual variability of the waves. The interactions between the interannual variability of significant wave height, SASA, cyclones and SAM index have been quantified in the Southwestern Atlantic, with a focus in the SBB region. The SASA variability is important for the significant wave height in the Southeastern Brazilian coast and its spatial position interferes in the occurrence of cyclones in the region. Zonal wind variability integrates the interaction between the first and fourth EOF modes of the 850-hPa geopotential height. The former is related to the meridional expansion (or contraction) and shift of the SASA and is shown to be an important forcing mechanism for the wave climate. The latter connects the SAM index to the Southwestern Atlantic climate variability.

Positive anomalies of geopotential height field related to the first mode agree strongly with westward anomalies of the first mode of zonal wind. These positive anomalies of the zonal wind ensure positives anomalies in both EOF1 and EOF2 of significant wave height in the interannual scale. When the first mode of geopotential height has negative values, the processes described above are inverted.

There is also an important but weaker interaction between the EOF1 of zonal wind and the EOF4 of the 850-hPa geopotential height. This is regarded as a SAM-index related mode and positive anomalies associated with the northern section of it are generally related to westward anomalies of the wind. A positive (negative) phase of SAM shifts SASA northward (southward).

Cyclone occurrences were shown to be important for the significant wave height variability in the southwestern region of the Atlantic. Higher occurrences of cyclones are linked to positive anomalies of the significant wave height. Anomalies associated with the EOF1 of the zonal wind (de)intensify cyclones occurrences over South Atlantic. When zonal wind anomalies are positive (negative), cyclones in the domain are more (less) frequent.

Trends of significant wave height at SBB are generally positive, although not significant. These trends contrast with the positive phase of SAM over the last decades (Marshall, 2003), which would weaken the cyclogenesis over the analyzed period (Reboita et al., 2009) and lead to a downward trend of the significant wave height. On the other hand, absolute wind magnitude is intensified which can counter-act a possible SAM-related downward trend. The significant wave height trend we observed in the area has the same order of magnitude of previous studies (Alfredini et al., 2014) and the absence of significance might be related to the relatively short period of this analysis and contrasting processes occurring at the same time.

4 RELEVANT PROCESSES FOR THE WAVE VARIABILITY IN THE SOUTHWESTERN REGION OF THE SOUTH ATLANTIC

4.1 Introduction

Over coastal regions, the sea surface height consists of the sum of the amplitude of surface wind waves, storm surges and high tides. It poses a risk for the population safety and economic activities close to the coastlines (Kuriyama et al., 2012; Hemer et al., 2010). Surface waves changes the shoreline by enhancing the sediment transport and intensifying the erosion, which may damage or even tear down buildings. They are relevant for the safety of navigation, the operation of ports, offshore oil platforms, but are also suitable as a source of electrical energy across the world (Espindola and Araújo, 2017) and were shown to be important in the advection of pollutants under strong wind forcing (Curcic et al., 2016).

Gravity waves are forced by the wind and are therefore under the influence of synoptic processes that control the atmospheric circulation. Subtropical anticyclones characterizes the circulation at low levels around the world and are spread over about 40% of the globe (Rodwell and Hoskins, 2001). These winds are controlled by different features such as the Hadley Circulation, the SST and monsoons (Rodwell and Hoskins, 2001; Seager et al., 2003; Gan et al., 2004; Vera et al., 2006; Richter et al., 2008). In the South Atlantic, the semi-permanent subtropical anticyclone is known as the South Atlantic Subtropical Anticyclone (SASA) or the South Atlantic Subtropical High, which contributes to weather and climate features over South America and South Atlantic basin (Reboita et al., 2019; Gilliland and Keim, 2018). For instance, NE winds of the SASA are the main forcing of southwestward propagating waves at areas close to the southeastern coast of Brazil (Pianca et al., 2010).

Cyclones are also important components in generating waves both in the tropics and over extra tropical regions. For instance, in the North Atlantic, extra tropical cyclones generate dangerous sea states with high waves associated to long fetches with strong winds (Ponce de León and Bettencourt, 2019). Over the North Pacific, explosive extra-tropical cyclones present a rapid wind speed intensification, which forces the significant wave height increase with a delay of a few hours. Enhanced peakedness and narrow directionality are relevant due to their association with the presence of freak waves and are forced on the right-hand side and also over the cold side of the warm front of these storms (Kita et al., 2018). On the southwestern South Atlantic cyclones are responsible for significant wave height events of over 6m (Innocentini and Neto, 1996; Machado et al., 2010; Campos et al., 2012; Pianca et al., 2010) and estimates of return period of swh for 50 and 100 years present values of 8.8 and 9.5m respectively (Campos et al., 2012).

As a semi-permanent system, the SASA is often disturbed and fragmented by transient cyclones(Degola, 2013; Reboita et al., 2019), which are formed at three different sites over South America. They are located at the south-southeast coast of Brazil (SE-BR), the northeastern Argentina/Uruguay region (LA PLATA) and the central Argentina coast (ARG) (Gan and Rao, 1991; Reboita et al., 2010; Gramcianinov et al., 2019). The SE-BR cyclogenesis region activity is more important during austral summer (Hoskins and Hodges, 2005; Reboita et al., 2010), while the austral winter is the moment when the LA PLATA region is most active. The southernmost ARG cyclogenesis area is the most active around the year (Hoskins and Hodges, 2005).

Over the year, the SASA has two peaks of intensity and size and the southern boundaries of its seasonal climatology (Sun et al., 2017) are collocated with the northern boundaries of the density tracks of cyclones (Gramcianinov et al., 2019). During the DJF months, the SASA lies over the center of the basin and locates furthest to the pole and its southwestern boundaries occur approximately at 40^oW (Sun et al., 2017). This longitude also represents the northeastern limits of the climatological density tracks of cyclones (Gramcianinov et al., 2019).

Along the southwestern brazilian coast the mean swh height show values of 1.7m and about 45% of the waves propagates from the E and NE directions and were associated to SASA (Pianca et al., 2010). In JJA months the SASA is centered over the western area of the South Atlantic domain at its northernmost position over the year and its western limits of the SASA extends further to 60^oW (Sun et al., 2017). At this time of the year, the latitude of 30^oS defines a the northern boundaries of the cyclones track density (Gramcianinov et al., 2019) and the southern limits of the SASA found (Sun et al., 2017). The cyclongensis is more frequent during boreal winter (Gan and Rao, 1991) and the cyclones forces waves that propagates from S direction in about 40% of the time (Pianca et al., 2010).

The meridional position of the SASA is dominated by ENSO on the interannual time scale during DJF. During La Niña (El Niño) years, SAM tends to be in its positive phase and in DJF the anticyclone is more usually displaced poleward (equatorward). During JJA several mechanisms such as the Southern Annular Mode (SAM), ENSO, the Asian-African monsoon, among others possibly are linked to the position of the anticyclones without a clearly dominating signal (Sun et al., 2017). Cyclogenesis also presents interannual variability over time (Reboita et al., 2010) and the position of cyclone trajectories are shifted northward under negative SAM phases, which enhances the frontogenetic activity the SE area of South America (Reboita et al., 2009). Although the synoptic components of wind system at low levels in the South Atlantic present interannual variability, a few studies found little correlation between the the El Niño Southern Oscillation (ENSO) and the wave climate in the southwestern South Atlantic (Pereira and Klumb-Oliveira, 2015; Dragani et al., 2010; Reguero et al., 2015). Trends over a few decades of the swh and the dwp have been identified with relatively small values (order of 10cm or less) (Dragani et al., 2010; Branco, 2016; Alfredini et al., 2014) and the studies suggest that interannual variability or the climate change are both plausible explanations for these results.

Previously, the wave climate on the southwestern south Atlantic was described based solely on the directional histograms of different wave parameters. Pianca et al. (2010) attributed their forcing to cyclones and the SASA, without presenting the spatial structure of the winds associated with the wave fields. Also, as the literature assumed the interannual variability in the area could be important and tried to find correlation between the local time series and indexes of climate variability (Pereira and Klumb-Oliveira, 2015; Dragani et al., 2010). So far, no important signal has been found, which could mean the interannual variability has a very small signal or is absent in the regional wave climate. Our science question is: what time scales and what spatial structure of the winds are important for the wave climate in the southwestern South Atlantic?

We describe the data and methodology over the wind and wave fields in the South Atlantic in Section 4.2. The average fields and dominant variability on the SW region of South Atlantic are presented in Figure 4.4. In Section 4.5 we present results that summarize the variability separated in frequencies equal, higher or lower than the annual cycle. We evaluate the spatial structure of wind and wave fields according to synoptic fields in Section 4.6. Finally the conclusion and summary are made in section 4.7

4.2 Dataset and methods

SURFACE WAVE MODEL

We employ the University of Miami Wave Model (Donelan et al., 2012) to compute the wave fields. It consists of a third generation wave model and it solves the energy balance equation in terms of the spectrum of elevation variance by wave number and propagation direction. The domain is solved in a 1^o resolution (70^oW-20^oE-60^oS-10^oN) and at each point, the spectral domain is organized in 32 directional bins and in 37 wave frequencies ranging from 0.0313Hz to 2.0Hz.

The wave model is initialized from the steady state and 6-hourly 10m winds from CFSR (CFSv2) force the wave fields between 1980-2010 (2011-2017). CFSv2 is used for validation, since CFSR does not cover the period when waves and wind measurements of Brazil's National Buoy Program (PNBOIA) are available. The period between 2011-2017 are used for the validation in the SW region of the South Atlantic.

Previous works have shown the wave conditions in the SW South Atlantic may be simulated accurately by the wind for without including the information from the Pacific and Indian Oceans, nor the North Atlantic (Branco, 2016; Pereira et al., 2017).

PNBOIA

The waves and winds were validated using data from 3 buoys from PNBOIA provided by the Global Ocean Observing System. They correspond to the buoys identified as Santos

(25.7^{o}S, 45.1^{o}W), Itajai (28,5^{o}S, 47.4^{o}W) and Rio Grande(31.52^{o}S, 49.8^{o}W). All buoys are located at the 200m isobath. Wave parameters in the datasets are the swh, dwd, mwp and the wind parameters in terms of wind speed and wind direction. Details of the the buoys were described by Pereira et al. (2017).

CYCLONE TRACKING ALGORITHM

In order to identify the cyclone occurrences, we use the tracking dataset calculated in Gramcianinov et al. (2019). They identified cyclones through the relative vorticity field computed from the zonal and meridional winds at 850hPa in the CFSR reanalysis results. This automated tracking system (Hodges, 1994, 1995) allows the detection of fast moving and weak systems which wouldn't be observed by algorithms based on the mean sea level pressure criteria (Sinclair, 1994). In the South Atlantic, the vorticity is a better choice to evaluate the cyclones (Sinclair, 1994; Hoskins and Hodges, 2002; Gramcianinov et al., 2019).

4.3 Model Validation

The swh, mwd and dwp, and wind components of measurements and model results at the buoys are compared in Figures 4.1 4.2, 4.3, 4.4, 4.5. In general, there is good agreement between the wave model and the observations, particularly for the swh and mwd direction.

Among the comparisons, the best results correspond to the swh simulation. According to the histograms (Figure 4.1d, e, f) and the scattered probability plots (Figure 4.1g, h, i), the simulated swh at Santos buoy underestimates values higher than 3m, while the results at Itajai and Rio Grande show a better agreement for this interval of wave height. For values smaller than 3m, the modeled the swh is better described over Santos region, while in Itajai and Rio Grande the modeled values are underestimated and overestimated, respectively. The mwd results also compare well with the observations, even though the NE and SW directions show each an underestimation of 5% (Figure 4.2). The histograms show there is an overestimation of about 3-5% in each direction bin between S-ESE (Figures 4.2d,e,f). The modes in the observed dwp occur in the period of 7-8s, whereas in the umwm results the modes are associated to periods of about 10s (Figures 4.3d,e,f). The correlation values in all buoys present values between 0.49 and 0.60, and the dwp is distributed in discrete bins of periods, which is a consequence of the relatively low resolution in the frequency space of this model, and of the non linear source function of the model.

The zonal wind component of CFSv2 underestimates (overestimates) zonal wind above (below) 10m s^{-1} (5m s^{-1}) and present correlation values between 0.59 and 0.72 with the observations. In the meridional wind, the histograms show a similar distribution between the CFSv2 numerical results and the observations. The amplitude of both zonal and meridional modeled components underestimates the values measured by the array of buoys at given periods and the most evident case occurred in 2016 in Santos and Itajai buoys, when the wind components of CFSv2 present 50% of the observed values. These values are responsible for the overestimated wind values in the histograms.

Surface waves integrate the energy transferred from the wind to the ocean as they propagate in the domain. At a given point the significant wave height time series is not only an answer to the local wind, but includes also the lateral advection of the waves.

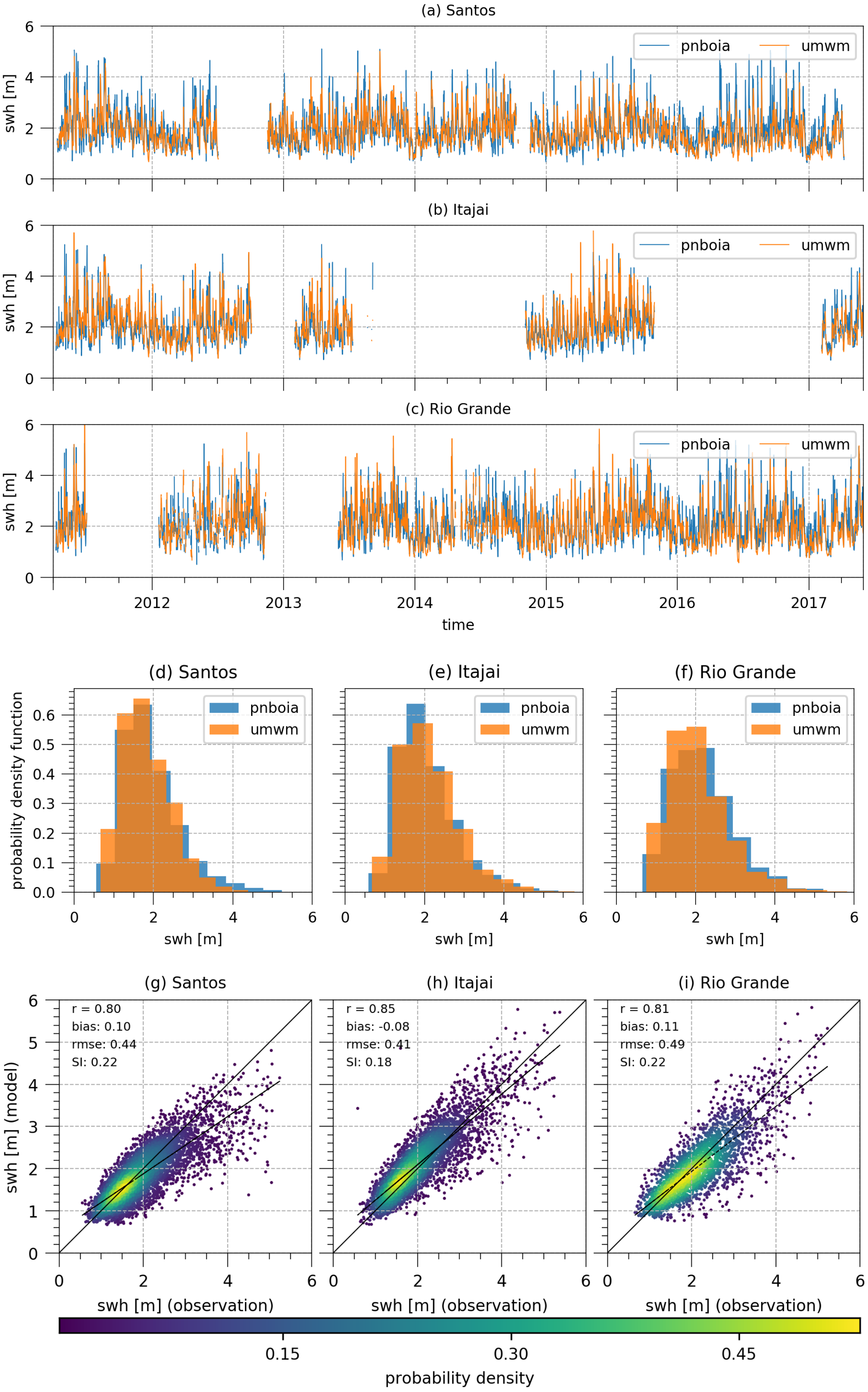

Figure 4.1: Time series (a, b, c), histograms (d, e, f) and scatter probability plot (g, h, i) of the significant wave height of the measured and model results at Santos (a, d, g), Itajai (b, e, h) and Rio Grande (c, f, i).

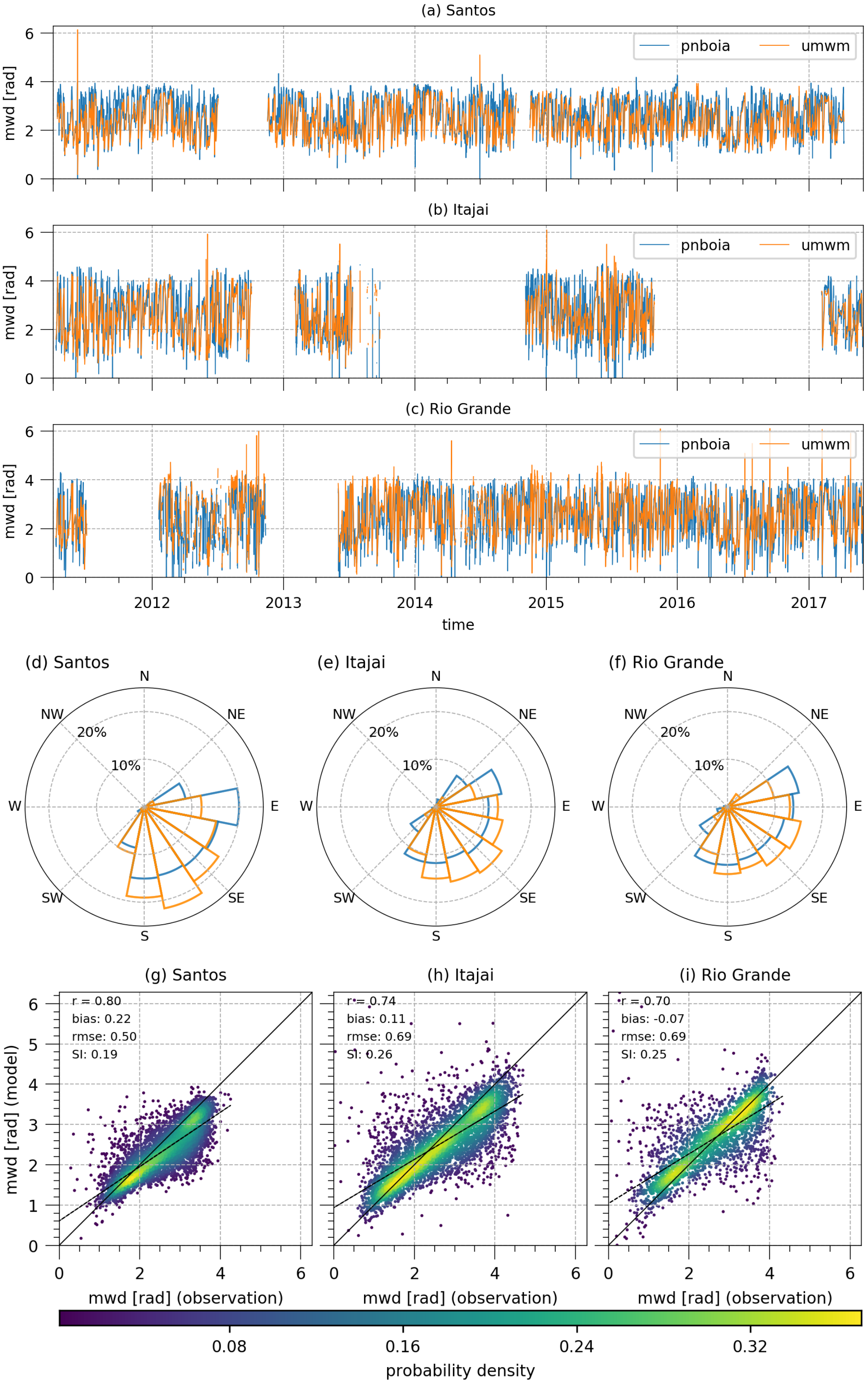

Figure 4.2: Time series (a, b, c), histograms (d, e, f) and scatter probability plot (g, h, i) of the mean wave of the measured and model results at Santos (a, d, g), Itajai (b, e, h) and Rio Grande (c, f, i).

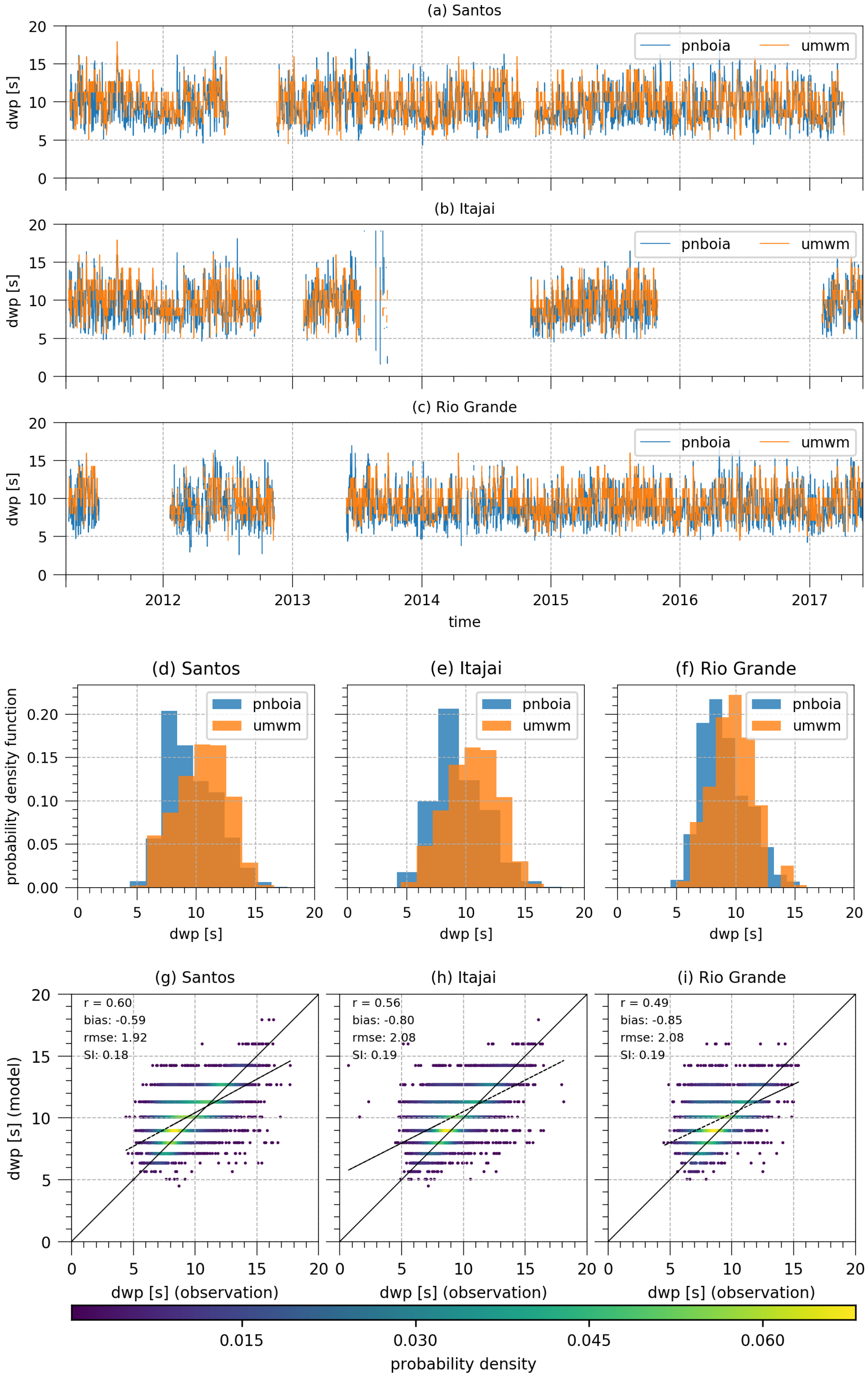

Figure 4.3: Time series (a, b, c), histograms (d, e, f) and scatter probability plot (g, h, i) of the dominant wave period of the measured and model results at Santos (a, d, g), Itajai (b, e, h) and Rio Grande (c, f, i).

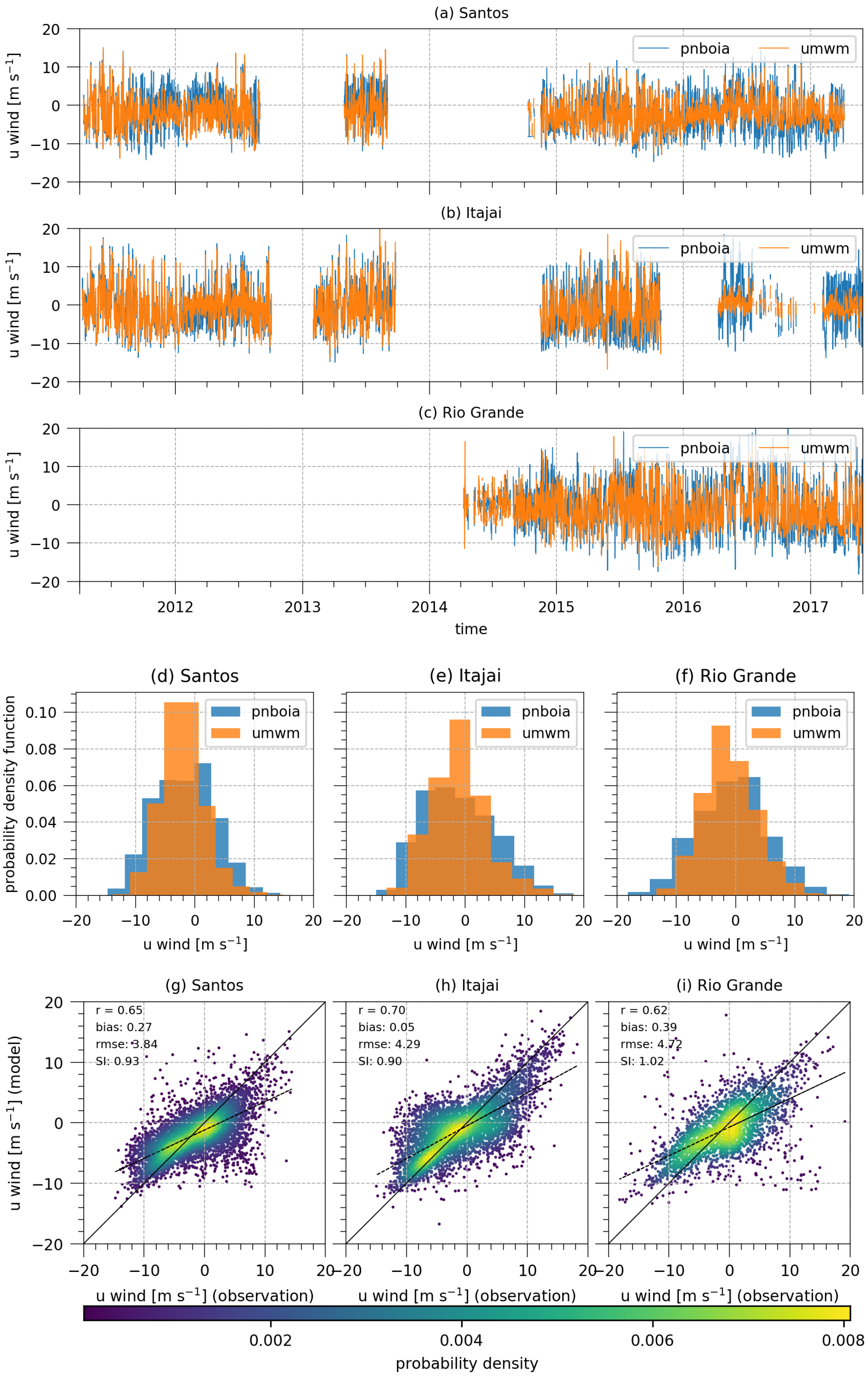

Figure 4.4: Time series (a, b, c), histograms (d, e, f) and scatter probability plot (g, h, i) of the zonal wind measured by measured and model results at Santos (a, d, g), Itajai (b, e, h) and Rio Grande (c, f, i).

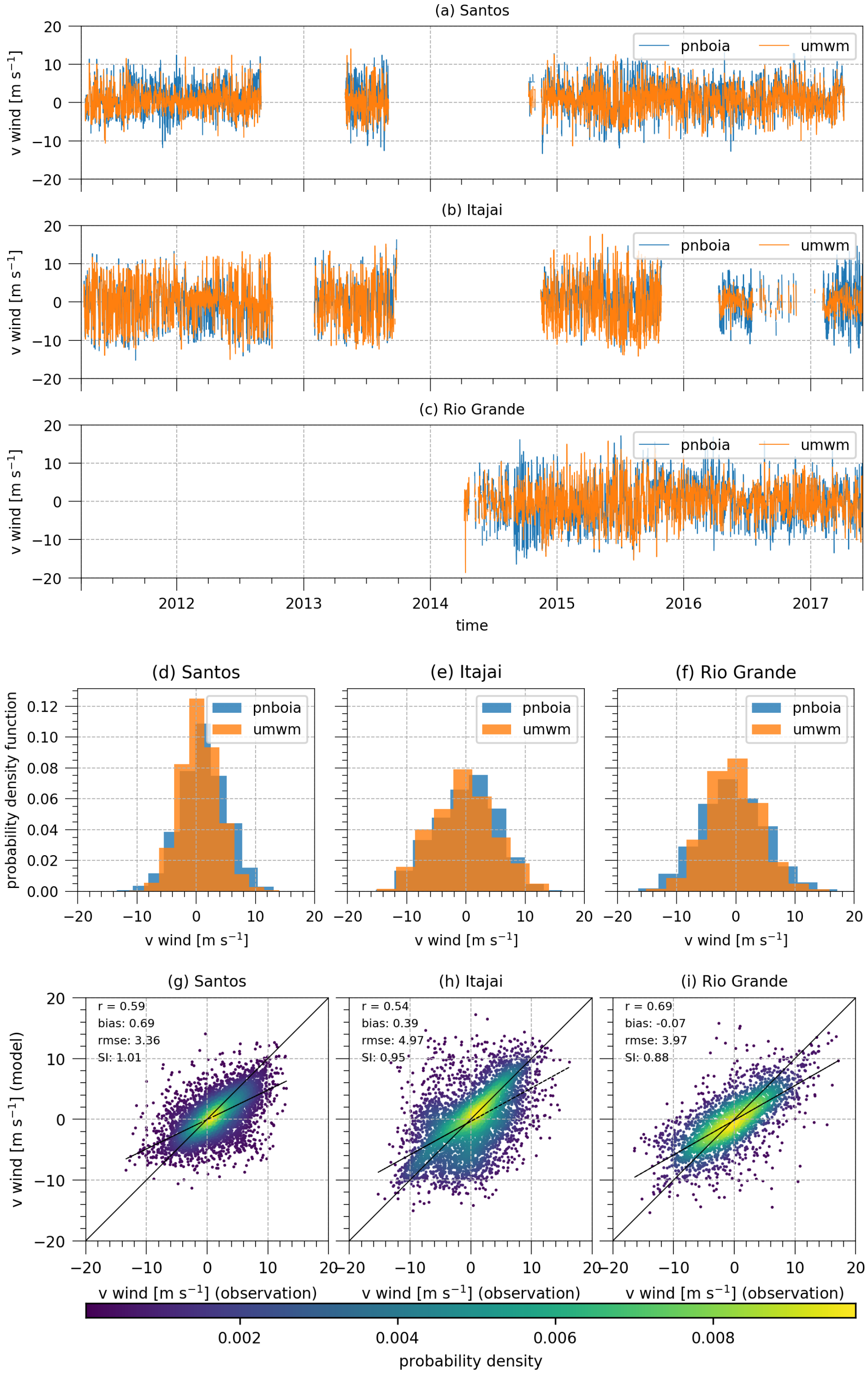

Figure 4.5: Time series (a, b, c), histograms (d, e, f) and scatter probability plot (g, h, i) of the meridional wind measured by measured and model results at Santos (a, d, g), Itajai (b, e, h) and Rio Grande (c, f, i).

4.4 Climatology of the 10m wind and the surface wave fields

Figure 4.6 presents the climatology of the 10m wind speed fields considering annual, December-January-February (DJF) and June-July-August (JJA) periods. In all three panels, the easterlies, the SASA and westerlies winds dominate respectively the tropical, subtropical and subpolar South Atlantic. The 10m wind signature of SASA consists of the mean anticyclone dominated by the easterlies (westerlies) winds northward (southward) of 20^oS (35^oS). The average climatology of swh generally follows the variability displayed by 10m winds and the dwd is also organized as an anticyclonic field forced by both easterlies and westerlies. Northward of 20^oS the easterlies dominate the average climate, with wind speed (swh) values ranging between 6 ± 2.5 m s^{-1} and 8 ± 1.5m s^{-1} (1.5 ± 0.9m and 2.5 ± 0.6m) and southward of 35^oS the westerlies are present with values ranging between 8 ± 3.5 m s^{-1} and over 12 ± 4.0m s^{-1} ($3.0\pm0.1.2$m and over 5 ± 1.8m). In the subtropical domain, the dwd is not always in the same direction of the wind, particularly in the SW South Atlantic.

Both position and intensity of the SASA in the 10m wind speed field present a seasonal variation and follows the patterns of the 850hPa geopotential fields described in the literature (Sun et al., 2017). While the western (eastern) limit of the SASA lies near 20^oS (35^oS), the central region of the anticyclone is organized into an elliptical shape with a semi-major axis parallel to the latitude lines. Near the SE coast of South America, the NE winds parallel to the coastline dominate the latitudes between 20^oS and 40^oS and the swh presents values of approximately 2m.

During DJF the center of the SASA lies at its climatological southernmost position at approximately 15^oW and 30^oS (Figure 4.6a). During this period we observed the lowest seasonal winds between 20^oS and 40^oS with average values from 5 ± 2.5m s^{-1} to 8 ± 2.0m s^{-1}. The swh associated to these winds ranges from 1 ± 0.9 to 2.5 ± 0.9m, which are relatively low values in the domain (Figure 4.6e). From DJF to JJA the SASA migrates equatorward to 20^oW and 27^oS (Figure 4.6c). In JJA we observed also an intensification of the average winds of approximately 2m s^{-1} followed by an average increase of 0.5m in the swh fields over the basin (Figure 4.6f). In JJA, the SASA is also organized in an elliptical shape, but there is a shift of its southern boundary. The mean westerlies with wind speeds values between 8.0m s^{-1} and 9.0m s^{-1} migrates to the north from 40^oS to 35^oS and the NE winds along the coast are active in between 20^oS and 35^oS. Previously in DJF these winds were

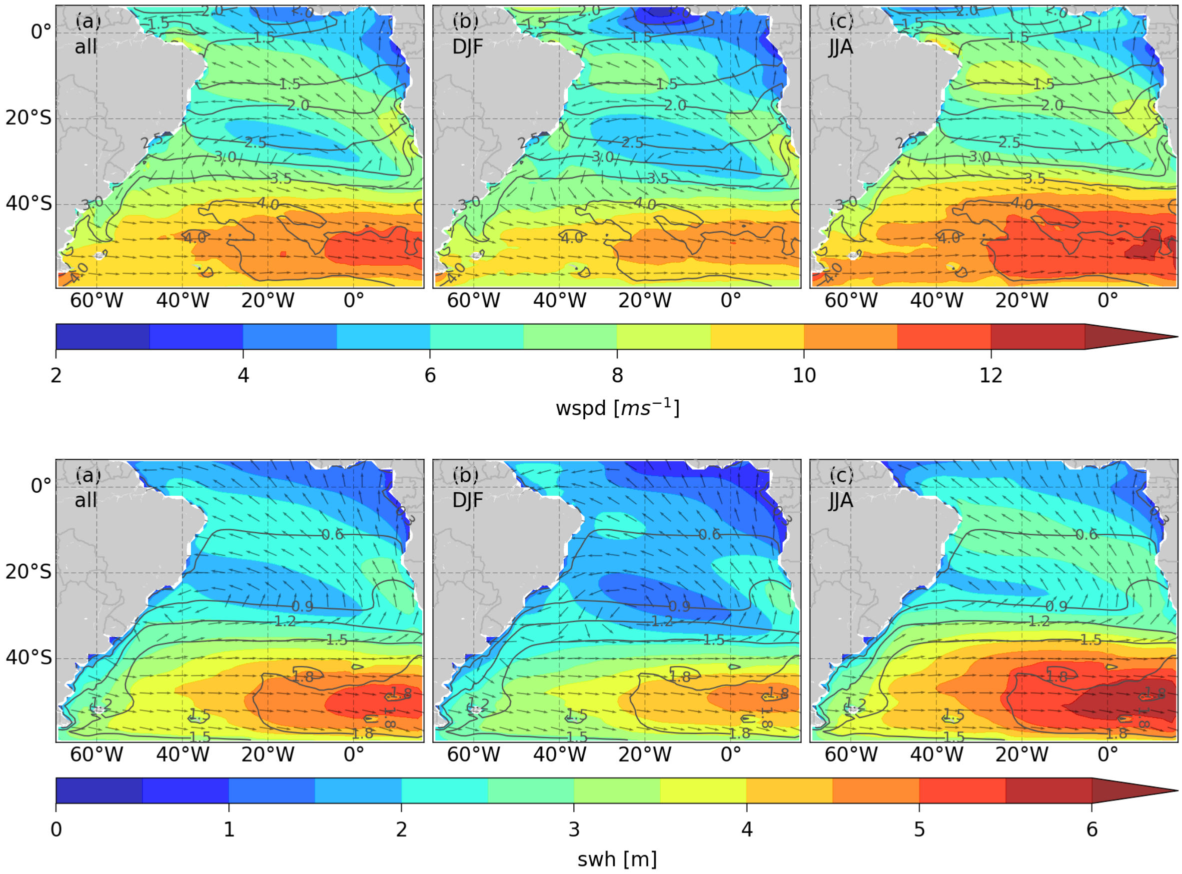

Figure 4.6: Annual (a), December-January-February (b) and June-July-August (c) climatology of wind speed (background colors) and wind direction (vectors). The contours represent the standard deviation of the swh.

distributed from 20^{o}S to 40^{o}S (Figure 4.6b).

Along the longitudes in 30^{o}S, the wind and wave directions are not parallel all the year around (Figure 4.6), which indicates that forcing mechanisms unrelated to the SASA are active. The directional histograms presented in Figures 4.7 and 4.8 show the wave and wind directions do not always agree in the southwestern region of the South Atlantic. For instance, in the SW quadrant the directional bars of the swh present percentage values as high as 20% (Figure 4.8f), while the directional bars of the wspd at the same position and season (Figure 4.8f) have maximum percentage values of approximately 10%. These histograms were built using the information available from the CFSR winds and the wave model results at the location of the selected PNBOIA buoys from 1980-2010. The swh directional histograms agree with the results of Pianca et al. (2010) and Pereira and Klumb-Oliveira (2015).

The directional histograms Figure 4.7 results and the climatology show the NE winds are the most frequent in the region of the buoys. The SW winds integrates the second mode in the distribution of the Itajai and Rio Grande histograms (Figure 4.7 d to i). Strong wind speeds ranging from 12-16m s^{-1} are present in the directions associated with the NE and S-SW winds at Itajai and Santos positions (Figure 4.7a to f), whereas in Rio Grande other directions also present these interval of values (Figure 4.7g, h, i). Winds from E-NE directions (counterclockwise) are the most frequent during the year and the winds from the W-S directions are active mostly during the JJA months (Figure 4.7c, f, i).

The waves also show a bimodal distribution in the histograms in the period from 1980-2010 (Figure 4.8). Again, the E-N quadrant corresponds to the most important mode in the distribution and the second most important mode is the quadrant W-S. There is a clear difference between the DJF and JJA wave climate. The DJF period shows the ESE, SE and SSE (SSE, S, SSW, SW) directions concentrate about 30% (20%) of the propagating waves (Figure 4.8b, e, h). During the JJA months the ESE, SE and SSE (SSE, S, SSW, SW) answer to about 15% (40%) of the propagating waves (Figure 4.8c, f, i). This change of direction is also followed by an increase of approximately 5% in the frequency of swh with heights ranging between 3-5m and propagating from the SSW direction. The wind and wave histograms present times when waves with swh lower than 1m are absent, although low wind speeds between 4-8m s^{-1} are preset. This confirms the presence of swell at all buoy locations.

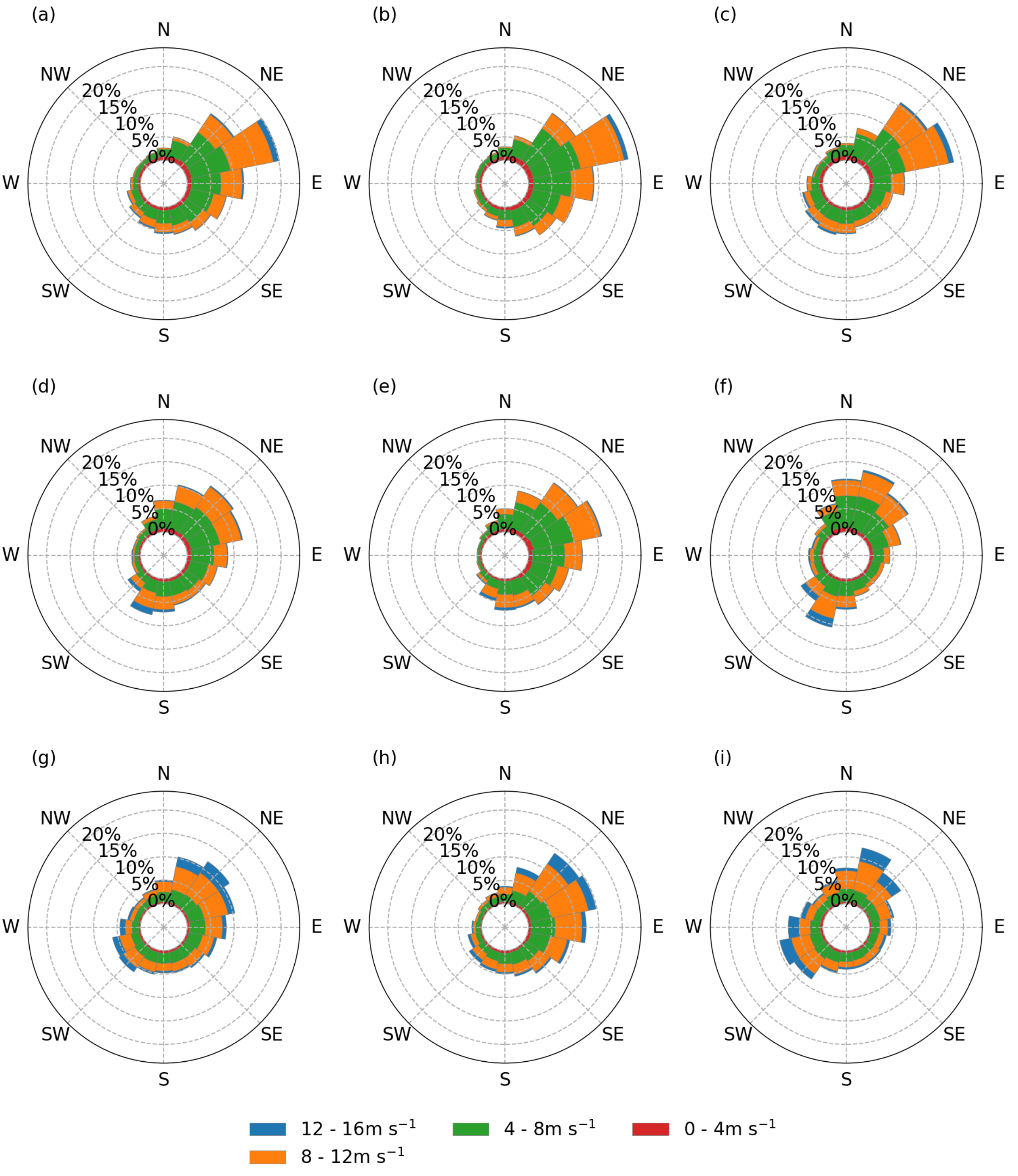

Figure 4.7: Directional histogram of the CFSR wind speed and the wind direction at (a,b,c) Santos, (d,e,f) Itajai and (g,h,i) Rio Grande buoy position. The periods correspond to (a,d,g) 1980-2010, (b,e,h) December-January-February and (c,f,i) June-July-August.

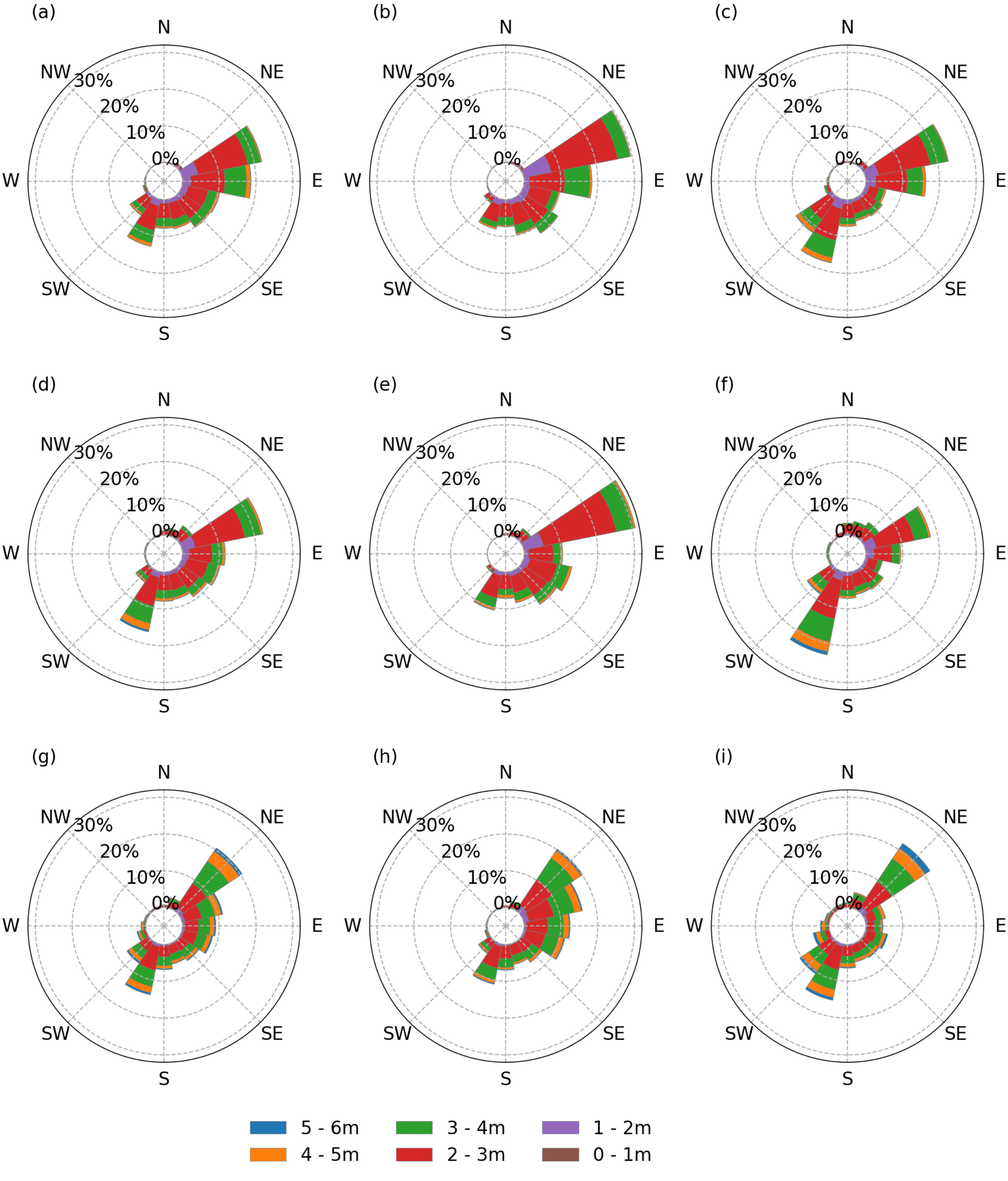

Figure 4.8: Directional histogram of the umwm significant wave height and the dominant wave direction at (a,b,c) Santos, (d,e,f) Itajai and (g,h,i) Rio Grande buoy position. The periods correspond to (a,d,g) 1980-2010, (b,e,h) December-January-February and (c,f,i) June-July-August..

4.5 Synoptic, Seasonal, and Interannual variability

We evaluate the waves amplitudes modeled with umwm associated to frequency bands lower, equal and higher than the annual cycle in the South Atlantic (Figures 4.9) estimating the power spectrum of the swh at the position of Itajai buoy (Fig4.9d). Santos and Rio Grande buoys share similar variability as with Itajai and are therefore omitted. The maps of standard deviation of the swh (σ_{swh}) are based on the Fourier reconstruction of the time series at each grid point. The annual and diurnal cycle in the SW region of South Atlantic are the only significant signal in the power spectrum (Figure 4.9d). Although significant, the diurnal cycle reconstruction (not shown) has a maximum magnitude of order 10^{-2}m over the continental shelf and usually represents less than 1% of the mean significant wave height values. Both the explained variance and the σ_{swh} show that the high frequency band contains most of the variability followed by the annual and low frequency signals, as expected (Figure 4.9a, b, c).

The σ_{swh} in the high frequency reconstruction has the same spatial structure and magnitude of the values indicated by the standard deviation of the swh in the climatology (Figure 4.6). In the South Atlantic it consists of about 70% (90%) of the total explained variance in tropical (subtropical and subpolar) regions. The explained variance of the seasonal cycle represents about 20% of the variability in the tropics and decreases gradually to about 5% in the subpolar regions. Our low frequency σ_{swh} panel (Figure 4.9c) presents significant height smaller than 0.5m in the entire basin and 2% of the explained variance suggests the interannual variability has little impact in the swh. This feature is further confirmed in the SW South Atlantic, where no significant peaks in the interannual period band ($>$ 1 year) is present (Figure 4.9d). The non significant correlation between the swh signal and climate indexes found previously in the literature (Pereira and Klumb-Oliveira, 2015; Dragani et al., 2010; Reguero et al., 2015) may be a consequence of relatively low values of the interannual component in the swh time series.

A similar reconstruction and Fourier analysis in the 10m wind speed parameter in Itajai is shown in Figure 4.10. The spatial structure of the 10m wind speed standard deviation (σ_{wspd}) and the power spectrum are similar to the swh (Figure 4.9). Despite the similarity, the explained variance of the 10m wind speed in the high frequency reconstruction ranges between 80% and 90% in the South Atlantic, which is even greater than for the

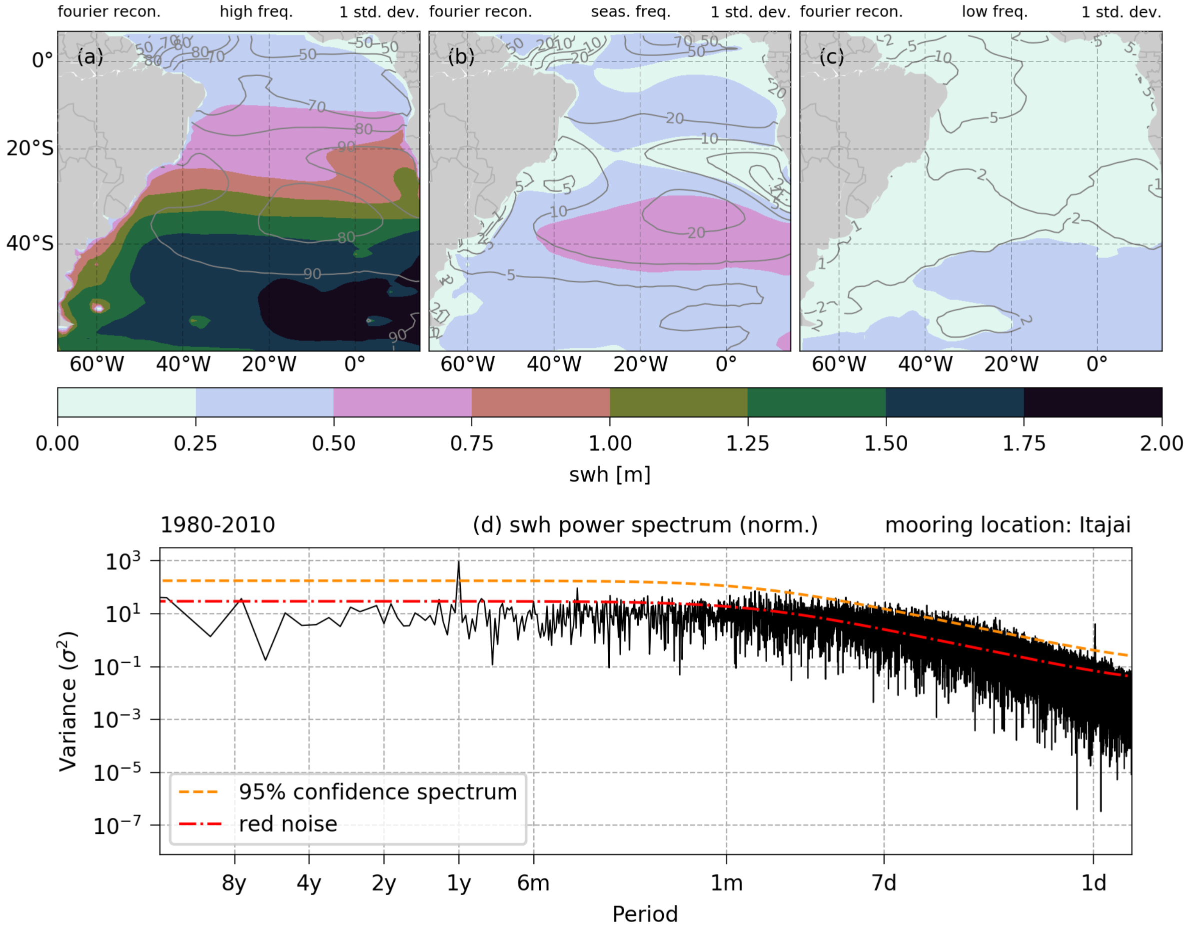

Figure 4.9: Standard deviation of the reconstructed significant wave height fields for (a) high, (b) seasonal and (c) low frequencies for the period between 1980-2010. Grey contours indicate the percentage of the explained variance of each reconstructed field compared to the total variance. Panel (d) shows the Fourier power spectrum (solid black line) of the swh of umwm on the position of Itajai buoy normalized by $N/2\sigma^2$, where N is the total number of points in the time series and σ is the standard deviation.

swh parameter (Figure 4.9). As the mean lifetime of a cyclone in the South Atlantic is 3.9±2.7 days (Gramcianinov et al., 2019), we also reconstructed a standard deviation map for the period band between 1-15 days (Figure 4.11). In the subtropics this reconstruction concentrates 60-80% of the explained variance and indicates cyclones are a dominant component of the variability in the region. For instance, southward of 30^{o}S, the σ_{wspd} in Figure 4.10a presents values greater than 3.0m s^{-1} as a consequence of these processes. In the SW South Atlantic, the significant signals in the power spectrum correspond again to the seasonal and diurnal cycles, where the diurnal cycle has maximum values of approximately 1m s^{-1}.

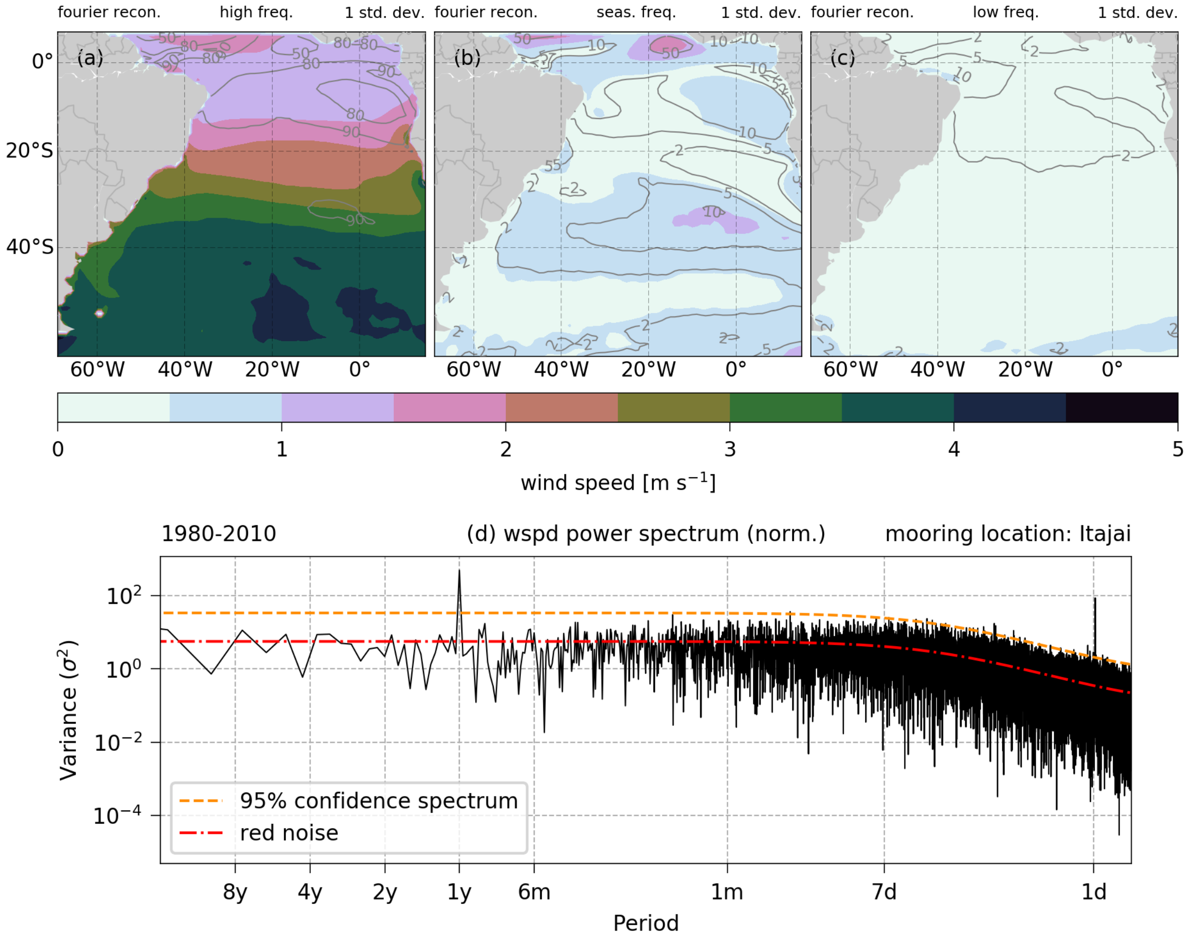

Figure 4.10: Standard deviation of the reconstructed swh fields for (a) high, (b) seasonal and (c) low frequencies for the period between 1980-2010. Grey contours indicate the percentage of the explained variance of each reconstructed field compared to the total variance. Panel (d) shows the Fourier power spectrum (solid black line) of the swh of umwm on the position of Itajai buoy normalized by $N/2\sigma^2$, where N is the total number of points in the time series and σ is the standard deviation.

The figure indicates about 90% of explained variance is dominated by high frequency processes in the subtropical regions followed respectively by the annual ($< 10\%$) and the

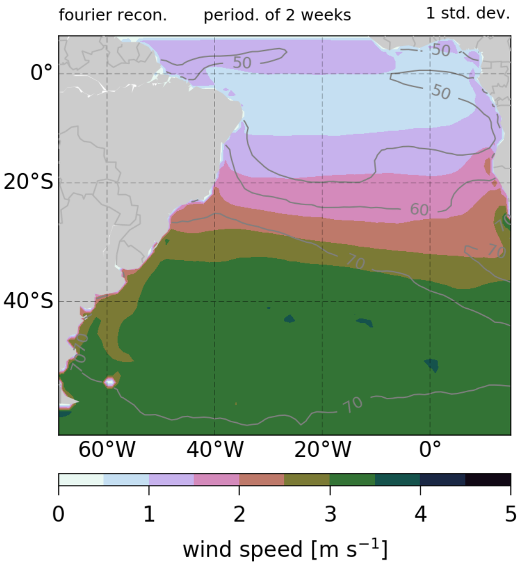

Figure 4.11: Standard deviation of the reconstructed significant wave height for the period band between 1-15 days between 1980-2010. Grey contours indicate the percentage of the explained variance of the reconstructed field compared with the total variance.

low frequency signal ($< 2\%$). Southward of 30^{o}S, the σ_{wspd} in Figure 4.10a presents values higher than 2.5m s^{-1} as a consequence of the variability of the westerlies, which appears as eastward propagating transient cyclones and anticyclones. At this region at least 70% of the total variance is explained by processes with period ranging from 1-14 days (Figure 4.12).

The seasonal reconstruction (Figure 4.10b) shows maximum σ_{wspd} values northward of the equator and in the subtropics (between 20^{o}S-40^{o}S)where the values range from 0.5m s^{-1} to 1.5m s^{-1}. These values coincide with the location of the climatological center of SASA in austral summer as indicated by the 10m wind speed minimum (see Section 4.4) and also with the northern boundaries of the climatological DJF cyclones density track (Gramcianinov et al., 2019). During JJA months the northern limits of the cyclones track and the center of the anticyclone migrates northward, which engulf the area previously occupied by the summer center of the SASA. This seasonal difference produces the maximum values of σ_{wspd} in the SW South Atlantic.

In the SW region of South Atlantic both SASA and cyclones have been linked to the variability of the ENSO and SAM during summer and to different climate indexes during winter (Sun et al., 2017; Reboita et al., 2009). The interannual signal of the 10m wind speed is not significant in the SW South Atlantic and the standard deviation associated

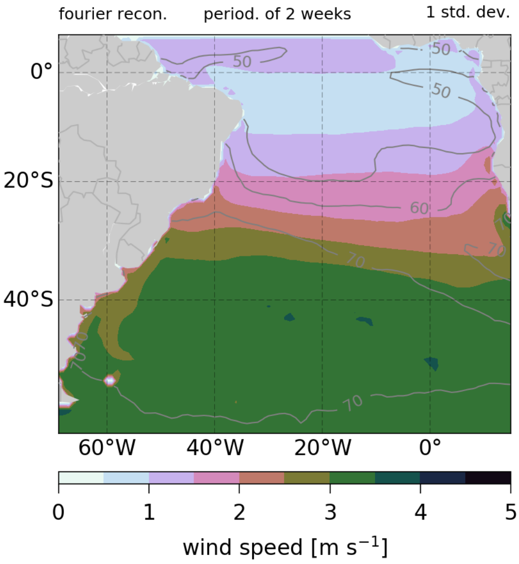

Figure 4.12: Standard deviation of the reconstructed wind speed for the period band between 1-15 days between 1980-2010. Grey contours indicate the percentage of the explained variance of the reconstructed field compared with the total variance.

with its reconstructed time series is smaller than 1m s^{-1} (Figure 4.10c). It answers for less than 2% of the explained variance over the South Atlantic, with the exception of the equatorial Atlantic close to the South America coast.

4.6 Synoptic wind structure and the wave fields over the SW South Atlantic

In the last section we showed that the transient synoptic systems have an important role in the variability in the subtropical South Atlantic. In this section, our aim is to understand what are the average wind fields associated to the transient and the semi-permanent systems, and how they they are connected to the wave field. We present composites of these parameters and σ_{wspd} based on the periods when waves were propagating to selected directions over the region of Itajai buoy from 1980 to 2010 (Figure 4.13). The directions (ψ) are delimited by the quadrants in between N< ψ ≤W, E< ψ ≤N, S< ψ ≤E and W< ψ ≤S (counterclockwise) and are defined as the conditions **A, B, C, D** hereinafter - ψ is the dominant direction at the buoy position. We only present the analysis from the Itajai composite, since the results are similar to Santos and Rio Grande results.

In all cases, W winds southward of 40°S present σ_{wspd} > 3.0m s^{-1} and are associated

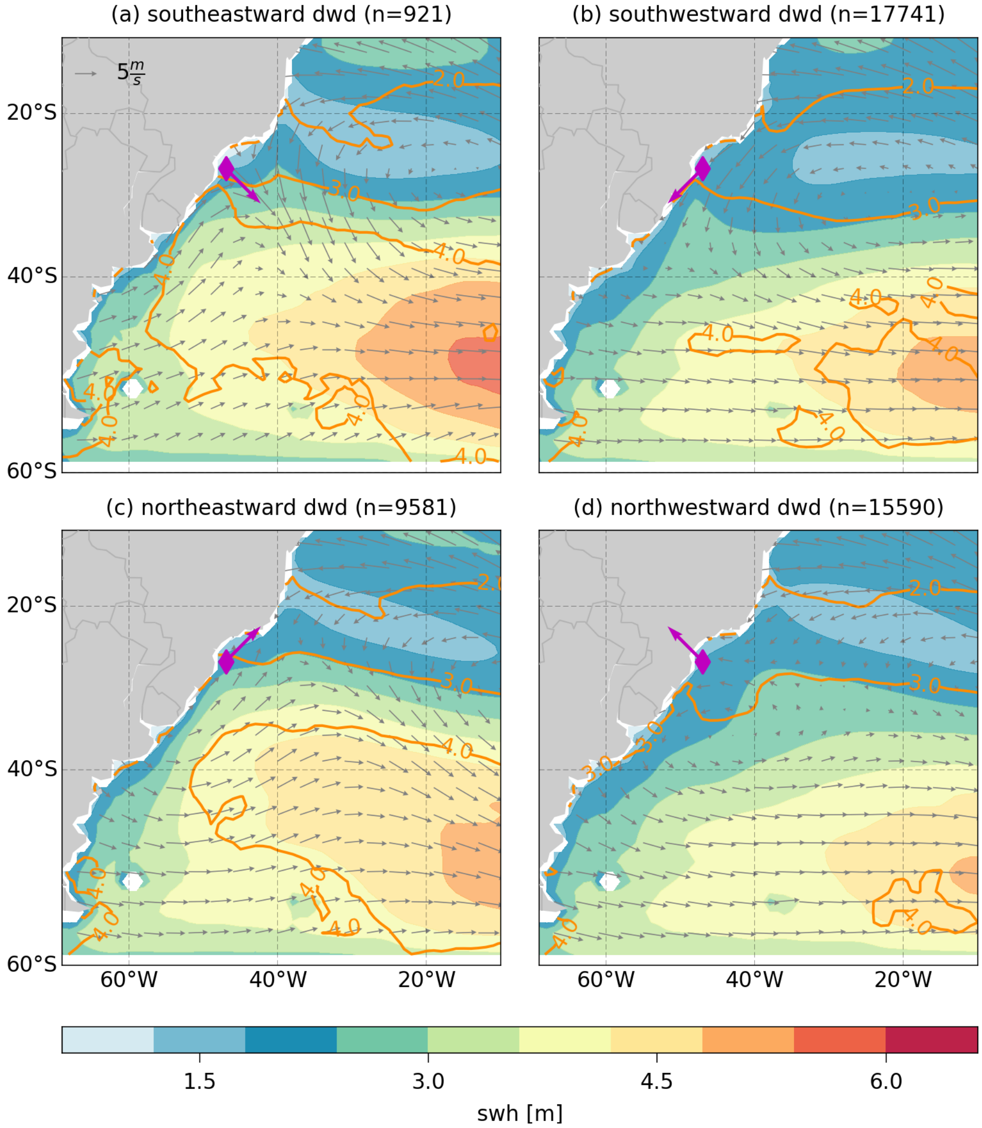

Figure 4.13: Composite analysis of the modeled significant wave height (background colors) and 10m wind fields calculated by selecting moments when the dominant direction (magenta vector) in the position of Itajai buoy (magenta diamond) points towards (a) SE, (b) SW, (c) NE and (d) NW. The orange contours represent the standard deviation of the wind speed fields.

with swh values of 3m or higher, while E winds are associated with swh values of about 3m or lower. The composite provides a mean wind field that is not necessarily linked to the occurrence of cyclones, since periods with no cyclones may be included in the analysis. Condition **A** (Figure 4.13a) captures a convergence of the winds over the buoy region, which produces NW winds and southwestward propagating waves on the region. The convergence consists of the combined effect of winds with a cyclonic (anticyclonic) configuration in the area to the south (east) of the buoy. This convergence is associated with swh values higher than 2.5m at about 30^{o}S. Under condition **B** (Figure 4.13b), low significant wave heights (<2.0m) are present between 20^{o}S and 40^{o}S, where the wind fields are dominated by the southwestward winds associated to an anticyclonic circulation in the area centered at 30^{o}W and 30^{o}S. The winds in condition **C** (Figure 4.13c) are similar to the fields in case **A**, but the convergence zone occurs further to the west. This configuration makes the winds in the buoy position to be dominated by the SW winds associated to the cyclonic region of the convergence zone. Under this configuration, a swh band with 4.5m to the south of 35^{o}S and to the west of 40^{o}W presents a NW-SE axis with increasing values to the pole, and occurs approximately n the same region as the 4.0m s^{-1} standard deviation of the 10m wind speed. Condition **D** (Figure 4.13d) shows relatively weak average winds of about 1-2 m s^{-1} over the buoy position, which are organized as an anticyclonic circulation on the area to the south of the buoy. Under conditions **A** and **C** the limits of the swh in the range between 3.0m-3.5m are close to the continent and positioned at its northernmost and westernmost position, whereas in conditions **B** and **D** these contours lie further to the south and east.

We present Figure 4.14 to explain the role of the cyclones and the anticyclones structures in the average fields of wind and swh. The Figure shows the conditions A, B, C, D only at moments when cyclones were present and also the probability density function of cyclone occurrences. It is based on the dataset of cyclones built by Gramcianinov et al. (2019). From 1980-2010 cyclones were active during 88.6% of the time in the South Atlantic domain.

The wind structure in Figure 4.13 and Figure 4.14 is similar where the probability density function of cyclones occurrence has values higher than 0.6. Under conditions **A** and **C** the SW winds to the south or west of the buoy present a southeastward turn when they meet the wind convergence area. This turn coincides with the domain where the

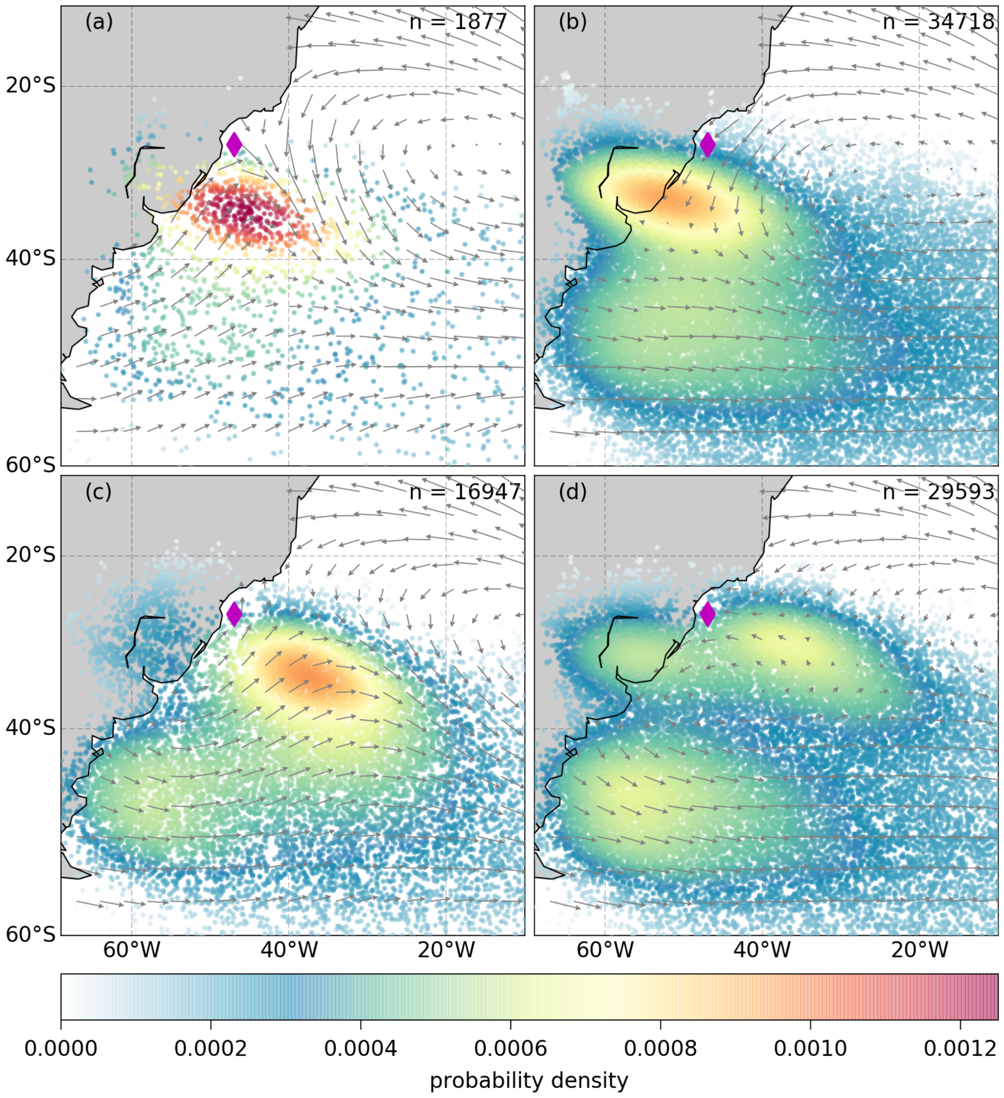

Figure 4.14: Composite analysis of the 10m wind fields calculated by selecting moments when (1) the dominant direction (magenta vector) in the position of Itajai buoy (magenta diamond) points towards (a) SE, (b) SW, (c) NE (d) NW and (2) a cyclone is present at the selected moment. The center of the cyclones are indicated by the dots.

cyclone occurrence has maximum probability. These relatively high values of occurrence are relevant for the 10m wind and wave fields composites and also mark the position of the average trough associated to the cyclones. The average fields show what are the signature of the background flow in the 10m wind field and also show the position where cyclones more effectively force the waves in the buoy location when waves propagate to NE.

The 10m wind field indicates the presence of mean anticyclones under conditions **B** and **D** (Figures 4.13b, d). On the vicinity of these anticyclones the probability density of cyclones has its highest values in each panel. The average anticyclone consist of propagating or stationary systems. The first case consist of systems that causes an atmospheric blocking and the second are part of the westward propagation of cyclones and anticyclones (Rodrigues et al., 2019; Sinclair, 1996). In all four panels there is a patch of occurrence centered at about 50^{o}S, which corresponds to cyclones generated at ARG region. These cyclones generally do not interfere significantly with the wind nor with the wave fields over the buoys site, unless they propagate to the area marked by the the probability density values of 0.7 in condition **A** or **C**. When the cyclones of ARG region are removed from the analysis there is no significant change in the wind and swh fields in any of the conditions. In the following paragraph, we explain the reason these systems are not relevant for the wave conditions in the buoy site.

Cyclones force changes the wave conditions in the buoy location either by forcing local waves directly or by forcing swell that propagates to the position of the buoy (specially in case **D**). Thus, the calculation of the composites may include cyclones independent from the swell that propagates across the buoy region as we observed in the cyclones formed at the ocean region next to ARG region (not shown). Additionally, cyclones detected by the TRACK algorithm in their initial stages may have no signature on the 10 wind speed nor on the wave fields since they are, at this stage, relatively weak systems.

In order to reduce the number of cases where independent wave systems and cyclones are included in the composite analysis, we calculate the composites by selecting moments when only one cyclone was active at a given time during DJF and JJA months for conditions **B** (Figure 4.15) and **C** (Fig4.16). We use the mean 10m wind speed over the ocean inside a 6^o radius around the center of the cyclone as a measure of the system intensity and indicate it on the position of the cyclones center. The radius size is based on the the sum of the mean and the standard deviation of the radius of maximum wind speed at 925hPa

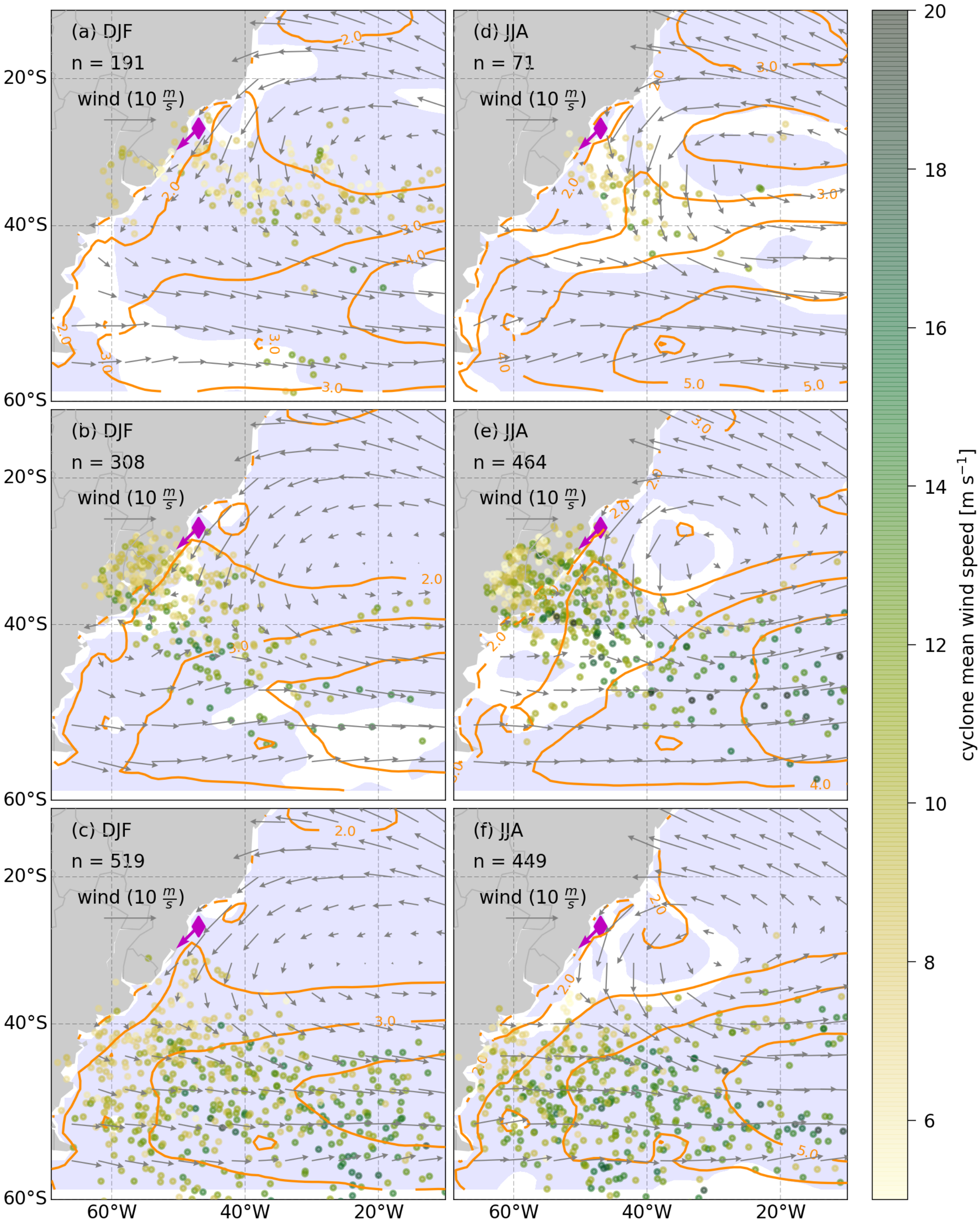

Figure 4.15: Mean values of the singificant wave height (orange contours), wind speed (black vectors) and cyclones position (dots) are plotted based on the moments when the mean wave direction points towards SW at the buoy position (magenta diamond). The color of the dots represents the mean wind speed within a 6 degrees radius around the center of the cyclone. The genesis of the cyclones occurred in the regions at (a,d,g) south-southeast coast of Brazil, (b,e,h), at northeastern Argentina/Uruguay and (c,f,i) the central Argentina coast. Background colors show areas with significant difference between the composite wave fields and the climatology.

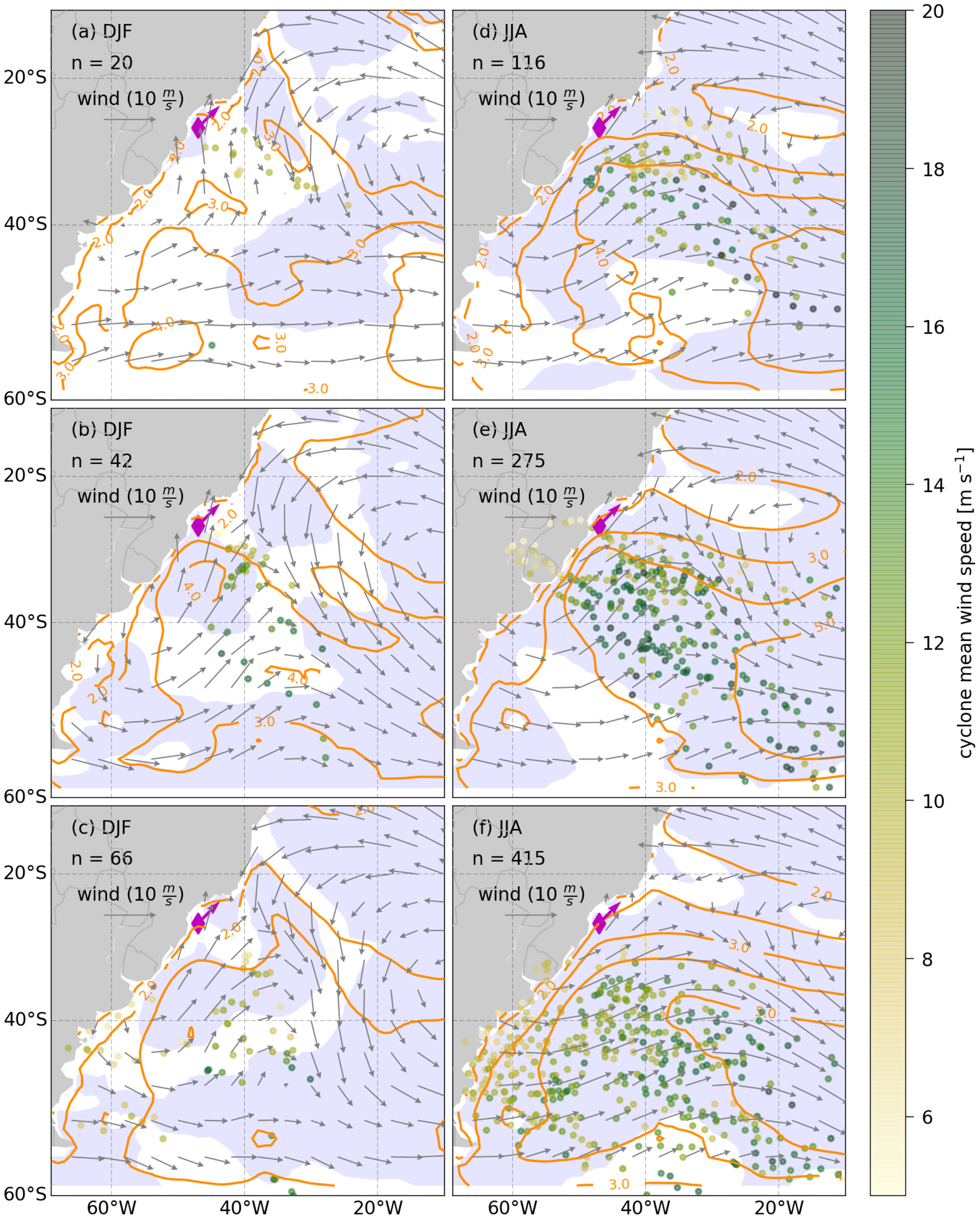

Figure 4.16: Mean values of the singificant wave height (orange contours), wind speed (black vectors) and cyclones position (dots) are plotted based on the moments when the mean wave direction points towards NE at the buoy position (magenta diamond). The color of the dots represents the mean wind speed within a 6 degrees radius around the center of the cyclone. The genesis of the cyclones occurred in the regions at (a,d,g) south-southeast coast of Brazil, (b,e,h), at northeastern Argentina/Uruguay and (c,f,i) the central Argentina coast. Background colors show areas with significant difference between the composite wave fields and the climatology.

of the entire cyclones track dataset, which is a default output of the algorithm.

Under condition **B** the wind fields present a structure that represents the western region of the SASA system during DJF months (Figures 4.15a,b,c). During JJA, the SE-BR region presents an average anticyclonic circulation with N winds approximately parallel to the coast (Figure 4.15d). In LA PLATA and ARG cases, the average anticyclone shows an approximate closed circulation structure which may represent the presence of transient anticyclones (Figure 4.15e,f). Cyclones formed within SE-BR have average winds ranging in the interval 5-10m s^{-1} (pale green dots) and may occur in the average anticyclone region (Figure 4.15a,d). These weak systems do not necessarily influence the mean wind and wave fields during DJF as we exemplify later in this section. In JJA the cyclones occur mostly at the western flank of the anticyclones (both the SASA and the transient anticyclones) and do not occur frequently at their central areas. The cyclones generated at LA PLATA region are present in the western and southern flanks of both transient anticyclones and the SASA (Figure 4.15c,f). Over the continent, the mean wind speeds of cyclones range in the interval 5-12m s^{-1}, whereas average values in the ocean range from 12m s^{-1} to over 18m s^{-1}. During DJF and JJA, cyclones formed in ARG region usually occur southward of 30^{o}S. The swh values range in the interval 1.0m-3.0m along the SE coast of South America and during DJF (JJA) the swh varies from 1.0m-2.0m (1.0m-3.0m) northward 30^{o}S, while to the south the average values are always greater than 2.0m.

Figure 4.17 presents different wind and swh fields associated to cyclones under condition **B**. SASA and transient anticyclones force southwestward propagating waves along the coast in DJF and JJA in Itajai region. During DJF the eastern or northeastern flank of the cyclones usually interact with (or are modulated by) the SASA winds in the SW South Atlantic, which results in areas where a convergence between the anticyclonic and cyclonic wind speeds may be higher than 10m s^{-1} (Figures 4.17a,c,d,f). At these regions with relatively strong winds, the swh values present values higher than 3.0m-4.0m. In other cases, like in Figure 4.17b, the cyclonic circulation is detected by the algorithm, but displays little or no signal in the 10m wind and in the swh fields. This situation is associated with cyclones formed over the SE-BR region during DJF, where the cyclogenesis are a typical consequence of a secondary recirculation of the winds (Gramcianinov et al., 2019). Figures 4.17e,f show two more examples when cyclones do not directly interact with the waves at the buoy region. In the first case the cyclone present winds weaker than

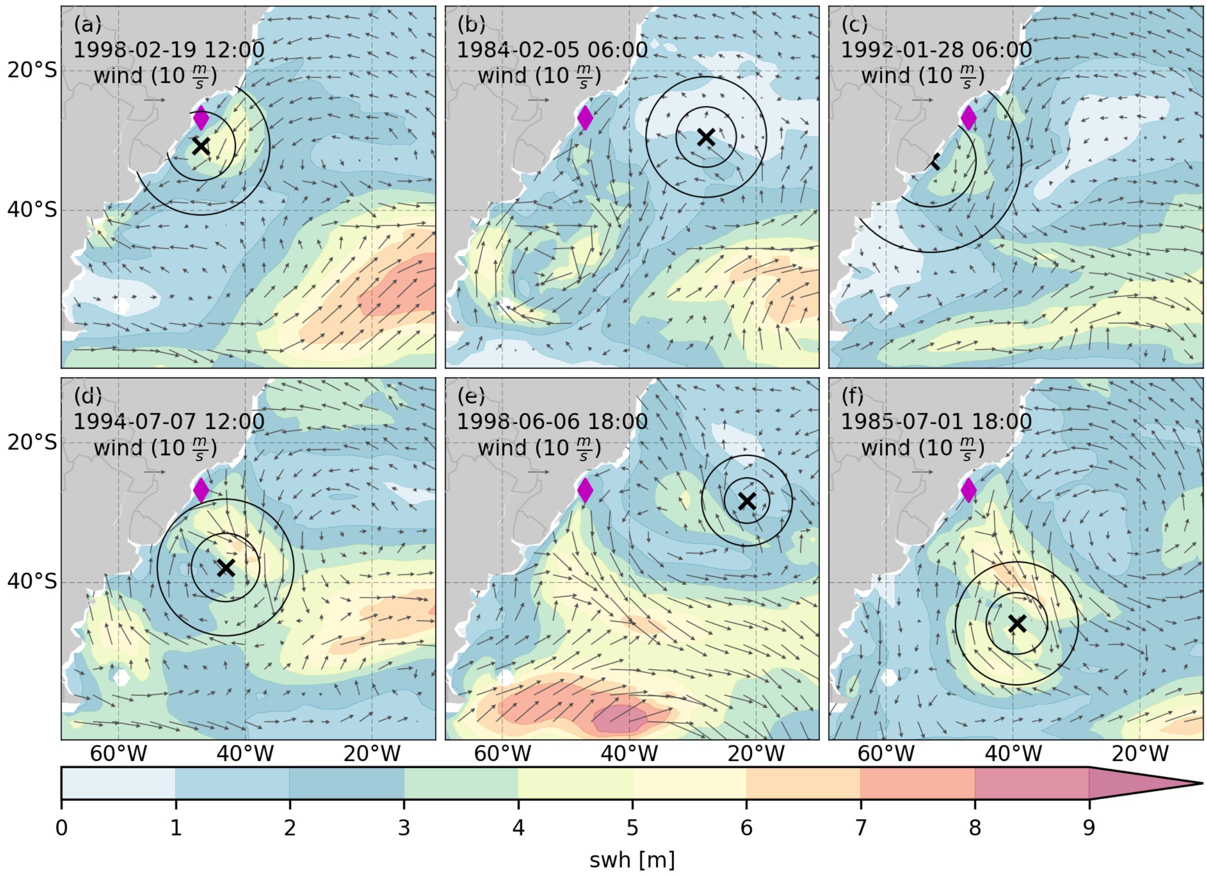

Figure 4.17: Fields of significant wave height (background colors) and 10m wind (vectors) under condition **B**. The black cross shows the position of the center of the cyclone and the black circles mark the circle with the radius and twice the radius of maximum wind speed at 925hPa.

10m s^{-1} and forces waves smaller than 4m and in the second case the cyclone is not near enough to the buoy to force the waves over the region.

Figure 4.16 reveals the seasonality is relevant to the intensity and number of cyclones in condition **C**, but is unimportant for the spatial structure of the wind and swh fields. Contours of swh higher than 3.0m are located in areas where the cyclones are present. During DJF, the mean wind speed of cyclones ranges from 8m s^{-1} to 14m s^{-1} and in JJA they are stronger, with values ranging from 10m s^{-1} to over 20m s^{-1} as indicated by the dark green dots in the figure.

The trough location is indicated by the average cyclonic winds (Figure 4.16) and does not depend on the cyclogenesis area, since cyclones can propagate from their genesis at SE-BR, LA PLATA or ARG region and force wave fields advected through the buoy position. Systems present during JJA at the ARG region to the west and south of the buoy site are an exception - as explained earlier, their position or intensity do not allow them to force

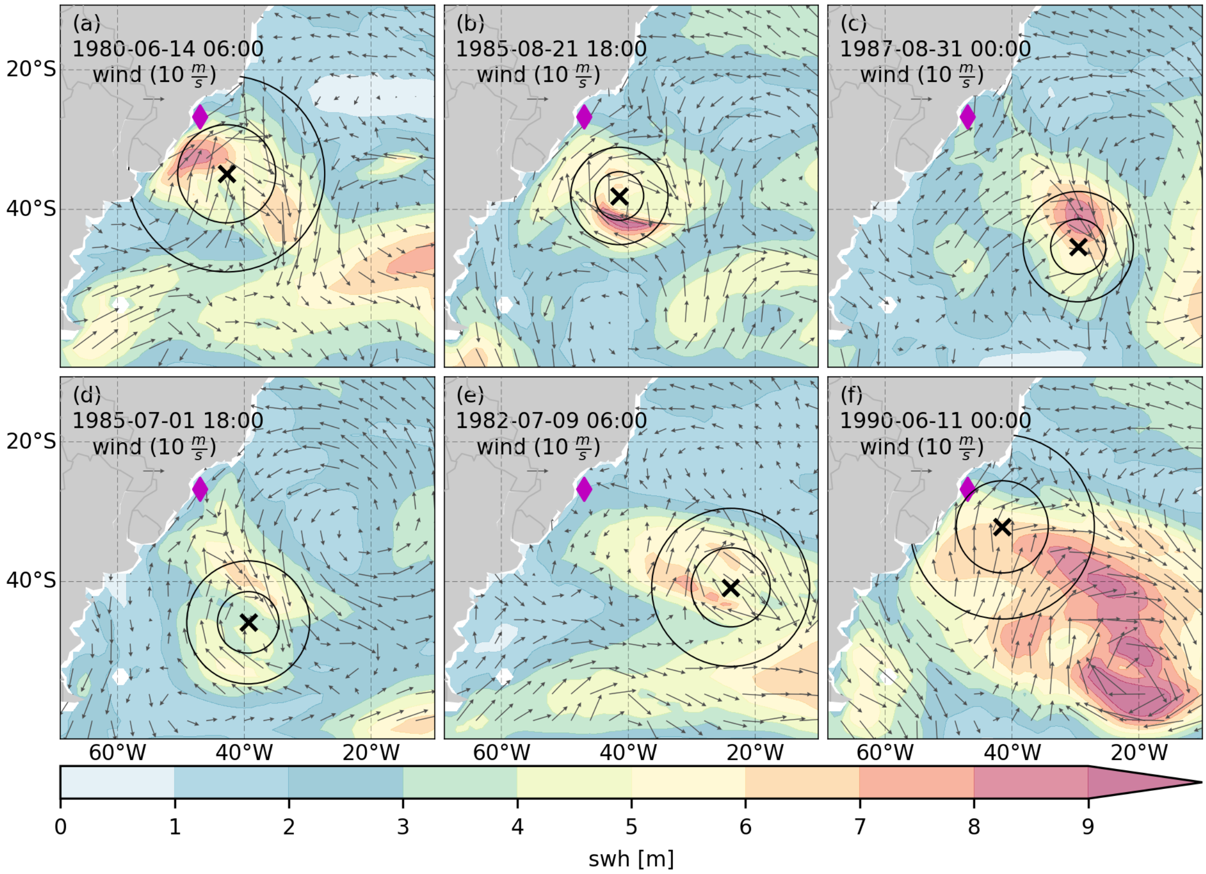

Figure 4.18: Fields of significant wave height (background colors) and 10m wind (vectors) under condition **C**. The black cross shows the position of the center of the cyclone and the black circles mark the circle with the radius and twice the radius of maximum wind speed at 925hPa.

waves that are sufficiently strong to be detected over in buoy site. Their detection is an artifact of the presence of propagating waves in the buoys associated to other systems.

A few selected cases show the configuration of wind fields when cyclones were detected under condition **C** (Figure 4.6). Figure 4.6a exemplify a case where the SW wind in the western flank of the cyclone is higher than 15m s^{-1} and generates waves with swh higher than 7m. In the east side of the cyclones, strong NW winds converging with E winds force swh values higher than 6m (Figure 4.6a to f). The areas at the western flank of the storm are not always associated to the maximum 10m winds as in Figure 4.6a, but are also represented in composite fields. In the region, the systems propagate mostly to SE according to the cyclones tracks (not shown) and leave a southeastward trail where northeastward winds and northeastward propagating swh are the dominant features (Figure 4.6c). These wind fields are usually present on the W/NW flank of the cyclone and in the rear of the SW/NE wind convergence zone, which indicates the cold front position (Figures 4.6b,c,e).

4.7 Conclusion

The spatial and temporal variability of the swh and the 10m wind speed have been studied in the South Atlantic with emphasis to its southwestern sector. The explained variance in the subtropical and subpolar regions shows swh and wind speed with frequency bands higher than the annual cycle are the most important (80-90%), followed by the annual cycle (5-20%) and the interannual variability (2%). The relatively small signal of the interannual variability helps explaining why studies like Pereira and Klumb-Oliveira (2015) and Dragani et al. (2010) found little or no apparent relationship with ENSO.

The directional histograms show the main modes of the waves propagation are towards NE and SW, which are roughly similar to what Pianca et al. (2010) found. Although the SW waves are frequent and present high values of swh, the dominant meteorological system in the region is the semi-permanent SASA and the average swh patterns follow the seasonal migration and intensification of this anticyclone.

By compositing the wind/wave fields and marking the position of transient cyclones, we identify different conditions that define the dominant wave direction in the S and SE coast of South America. Winds associated to the SASA and transient anticyclones are present during DJF and JJA. In DJF, the SASA circulation dominates the 10m wind fields when the waves over the buoys propagates southwestward. During JJA, a local mean anticyclone is present, which represents transient anticyclones reported previously in the literature (Sinclair, 1996; Rodrigues et al., 2019). These wind fields are associated with an average lower significant wave height in the continental shelf to the west of 40^oW and associated cyclones occur in the vicinity of these high pressure systems. Some cyclones were also detected by the tracking algorithm in the area of the average anticyclone, but these systems are weak with little or no signature in the surface,

The average 10m wind fields mark the position where cyclones occur most frequently, when the dominant wave direction points towards SE and NE in the position of the PN-BOIA buoys. Higher average swh are associated to these conditions to the west of 40^oW in the continental shelf.

5 FINAL REMARKS

5.1 Summary

A description of the wave variability and its forcing is presented in this work. In the second chapter the University of Miami Wave Model (umwm) was tested and two changes were implemented in the source code of the model with the aim of improving the model accuracy and precision. The first modification consisted of the inclusion of a wind input source function (Donelan et al., 2006) that presents the sheltering hypothesis (Jeffreys, 1924, 1925). The results of a global run with the original code of umwm and another with the source function of Donelan et al. (2006) are compared against National Data Buoy Center (NDBC) buoy measurements. The run with the new implementation led to an improvement of biases associated to values of significant wave height (swh) lower than 3m, which was translated in the simulation with better correlations and mean values. The second implementation consisted of the inclusion of an algorithm in the model code for setting up boundary conditions for a regional model with a higher resolution grid. It uses the spectral results from a low resolution model. In deep water, the results of the high and low resolution grid presented similar time variability , although a 12hours lag is introduced into the high resolution grid. In shallow water, the model source functions related to the wave-wave non-linear interaction and the associated wave dissipation led to an overestimation of the dominant wave period values due to enhanced spilling breakers in a shoaling environment. The main improvements of the results were seen in the Pacific both in terms of the swh and the dominant wave period.

Chapter 3 shows that the interannual variability of the swh in the southwestern region of the South Atlantic is connected to the meridional expansion and shift of the South Atlantic Subtropical Anticyclone. A contraction (expansion) of the anticyclone calculated by the EOF1 of the geopotential height induces negative (positive) anomalies of the zonal wind, which forces negative (positive) anomalies on the wave field associated to the EOF1 of the significant wave height. The EOF4 of the 850hPa geopotential height is correlated (0.67) to the Southern Annular Mode (SAM). In the southwestern region of the South Atlantic, the second Empirical Orthogonal Function (EOF2) of the significant wave height present a strong correlation the EOF1 of the zonal wind (-0.86). This shows that the interannual variability of the SASA and SAM acts in the wave climate and that the zonal wind is the parameter that better communicates these large scale systems to the waves in the southwestern region of South Atlantic.

In Chapter 4 we evaluate the variability of the swh from the interannual to the synoptic time scales with emphasis in the SASA and transient cyclones and anticyclones. The results show that the position and intensity of these meteorological systems are relevant to determine the average dominant wave direction and significant wave height values on the SE coast of South America. Waves propagating southeastward (northeastward) are produced by transient cyclones located to the south (southwest) of the buoy and present significant wave height values higher than 2-3m. When waves are propagating to southeast, the wind forcing is related to transient anticyclones during June-July-August and to the SASA during December-January-February and the significant wave heights average in the coast are as high as 2m. In this work we have shown the interannual variability present relatively small magnitude when compared with the total signal containing 2% of the total explain variance.

Bibliography

Alfredini, P., E. Arasaki, A. Pezzoli, M. Arcorace, E. Cristofori, and W. C. de Sousa (2014). Exposure of Santos Harbor Metropolitan Area (Brazil) to Wave and Storm Surge Climate Changes. *Water Quality, Exposure and Health 6*(1-2), 73–88.

Andrews, D. G. and M. E. McIntyre (1978). On wave-action and its relatives. *J . Fluid Mech 89*(4), 647–664.

Ardhuin, F., W. C. O'Reilly, T. H. C. Herbers, and P. F. Jessen (2003). Swell Transformation across the Continental Shelf. Part I: Attenuation and Directional Broadening. *Journal of Physical Oceanography 33*(9), 1921–1939.

Atlas, R., R. N. Hoffman, J. Ardizzone, S. M. Leidner, J. C. Jusem, D. K. Smith, and D. Gombos (2011, feb). A Cross-calibrated, Multiplatform Ocean Surface Wind Velocity Product for Meteorological and Oceanographic Applications. *Bulletin of the American Meteorological Society 92*(2), 157–174.

Babanin, A. (2011). *Energy dissipation across the wave spectrum*, pp. 232–321. Cambridge: Cambridge University Press.

Babanin, A. V., M. L. Banner, I. R. Young, and M. A. Donelan (2007). Wave-Follower Field Measurements of the Wind-Input Spectral Function. Part III: Parameterization of the Wind-Input Enhancement due to Wave Breaking. *Journal of Physical Oceanography 37*(11), 2764–2775.

Babanin, A. V., M. Onorato, and F. Qiao (2012). Surface waves and wave-coupled effects in lower atmosphere and upper ocean. *Journal of Geophysical Research: Oceans 117*(11), 1–10.

Belcher, S. E. and J. C. R. Hunt (1993). Turbulent shear flow over slowly moving waves. *Journal of Fluid Mechanics 251*, 109–148.

Blumberg, A. F., N. Georgas, L. Yin, T. O. Herrington, and P. M. Orton (2015). Street-scale modeling of storm surge inundation along the New Jersey Hudson river waterfront. *Journal of Atmospheric and Oceanic Technology 32*(8), 1486–1497.

Branco, F. V. (2016). *As mudanças climáticas e o clima de ondas no atlântico sul.* Ph. D. thesis, Instituto de Astronomia, Geofísica e Ciências Atmosféricas. Universidade de São Paulo.

Campos, R. M., C. E. Parente, and R. de Camargo (2012, jul). Extreme Wave Analysis in Campos Basin (Rio de Janeiro - Brazil) Associated With Extra-Tropical Cyclones and Anticyclones. In *Volume 2: Structures, Safety and Reliability*, pp. 71–80. American Society of Mechanical Engineers.

Castro, B. M. and T. N. Lee (1995). Wind-forced sea level variability on the southeast Brazilian shelf. *Journal of Geophysical Research 100*(C8), 16045.

Cavaleri, L., J. H. G. M. Alves, F. Ardhuin, A. Babanin, M. Banner, K. Belibassakis, M. Benoit, M. Donelan, J. Groeneweg, T. H. C. Herbers, P. Hwang, P. A. E. M. Janssen, T. Janssen, I. V. Lavrenov, R. Magne, J. Monbaliu, M. Onorato, V. Polnikov, D. Resio, W. E. Rogers, A. Sheremet, J. McKee Smith, H. L. Tolman, G. van Vledder, J. Wolf, and I. Young (2007). Wave modelling - The state of the art. *Progress in Oceanography 75*(4), 603–674.

Chawla, A., D. M. Spindler, and H. L. Tolman (2013). Validation of a thirty year wave hindcast using the Climate Forecast System Reanalysis winds. *Ocean Modelling 70*, 189–206.

Chen, G., B. Chapron, R. Ezraty, and D. Vandemark (2002, nov). A Global View of Swell and Wind Sea Climate in the Ocean by Satellite Altimeter and Scatterometer. *Journal of Atmospheric and Oceanic Technology 19*(11), 1849–1859.

Chen, S. S. and M. Curcic (2016). Ocean surface waves in Hurricane Ike (2008) and Superstorm Sandy (2012): Coupled model predictions and observations. *Ocean Modelling 103*, 161–176.

Chen, S. S., J. F. Price, W. Zhao, M. A. Donelan, and E. J. Walsh (2007). The CBLAST-Hurricane program and the next-generation fully coupled atmosphere-wave-ocean models for hurricane research and prediction. *Bulletin of the American Meteorological Society 88*(3), 311–317.

Chen, S. S., W. Zhao, M. A. Donelan, H. L. Tolman, S. S. Chen, W. Zhao, M. A. Donelan, and H. L. Tolman (2013). Directional Wind–Wave Coupling in Fully Coupled Atmosphere–Wave–Ocean Models: Results from CBLAST-Hurricane. *Journal of the Atmospheric Sciences 70*(10), 3198–3215.

Chune, S. L. and L. Aouf (2018). Wave effects in global ocean modeling: parametrizations vs. forcing from a wave model. *Ocean Dynamics 68*(12), 1739–1758.

Curcic, M., S. S. Chen, and T. M. Özgökmen (2016). Hurricane-induced ocean waves and stokes drift and their impacts on surface transport and dispersion in the Gulf of Mexico. *Geophysical Research Letters 43*(6), 2773–2781.

Dawson, A. (2016). eofs: A Library for EOF Analysis of Meteorological, Oceanographic, and Climate Data. *Journal of Open Research Software 4*, 4–7.

Degola, T. S. D. (2013). *Impacts and Variability of the South Atlantic Subtropical Anticyclone on Brazil in the Present Climate and in Future Scenarios.* Ph. D. thesis, University of São Paulo,.

Dobrynin, M., J. Murawski, J. Baehr, and T. Ilyina (2015). Detection and attribution of climate change signal in ocean wind waves. *Journal of Climate 28*(4), 1578–1591.

Dobrynin, M., J. Murawsky, and S. Yang (2012, sep). Evolution of the global wind wave climate in CMIP5 experiments. *Geophysical Research Letters 39*(18), 2–7.

Donelan, M. A. (2001). A nonlinear dissipation function due to wave breaking. *Proceedings of ECMWF workshop on ocean wave forecasting, 2–4 July 2*(4), 87–94.

Donelan, M. A., A. V. Babanin, I. R. Young, and M. L. Banner (2006). Wave-Follower Field Measurements of the Wind-Input Spectral Function. Part II: Parameterization of the Wind Input. *Journal of Physical Oceanography 36*(8), 1672–1689.

Donelan, M. A., M. Curcic, S. S. Chen, and A. K. Magnusson (2012). Modeling waves and wind stress. *Journal of Geophysical Research: Oceans 117*(7), 1–26.

Dragani, W. C., P. B. Martin, C. G. Simionato, and M. I. Campos (2010). Are wind wave heights increasing in south-eastern south American continental shelf between 32^{o}S S and 40^{o}S S? *Continental Shelf Research 30*(5), 481–490.

Earle, M. (1996). Nondirectional and directional wave data analysis procedures. *NDBC Tech. Doc. 96 002*(January), 43.

Espindola, R. L. and A. M. Araújo (2017). Wave energy resource of Brazil: An analysis from 35 years of ERA-Interim reanalysis data. *PLoS ONE 12*(8), 1–28.

Fyfe, J. C. (2003). Extratropical Southern Hemisphere cyclones: Harbingers of climate change? *Journal of Climate 16*(17), 2802–2805.

Gan, M. A., V. E. Kousky, and C. F. Ropelewski (2004). The South America Monsoon circulation and its relationship to rainfall over west-central Brazil. *Journal of Climate 17*(1), 47–66.

Gan, M. A. and V. B. Rao (1991, may). Surface Cyclogenesis over South America. *Monthly Weather Review 119*(5), 1293–1302.

Georgas, N. and A. F. Blumberg (2010). Establishing Confidence in Marine Forecast Systems: The design and skill assessment of the New York Harbor Observation and Prediction System, version 3 (NYHOPS v3). *Estuarine and Coastal Modeling 7*(2009), 1447–1456.

Gillett, N. P., D. A. Stone, P. A. Stott, T. Nozawa, A. Y. Karpechko, G. C. Hegerl, M. F. Wehner, and P. D. Jones (2008). Attribution of polar warming to human influence. *Nature Geoscience 1*(11), 750–754.

Gilliland, J. M. and B. D. Keim (2018). Position of the South Atlantic anticyclone and its impact on surface conditions across Brazil. *Journal of Applied Meteorology and Climatology 57*(3), 535–553.

Gower, J. F. R. (2002). Temperature, wind and wave climatologies, and trends from marine meteorological buoys in the Northeast Pacific. *Journal of Climate 15*(24), 3709–3718.

Grabemann, I. and R. Weisse (2008). Climate change impact on extreme wave conditions in the north sea: An ensemble study. *Ocean Dynamics 58*(3-4), 199–212.

Gramcianinov, C. B., K. I. Hodges, and R. Camargo (2019, oct). The properties and genesis environments of South Atlantic cyclones. *Climate Dynamics 53*(7-8), 4115–4140.

Gulev, S. K. and L. Hasse (1999). Changes of wind waves in the North Atlantic over the last 30 years. *International Journal of Climatology 19*(10), 1091–1117.

Hasselmann, K. (1962, apr). On the non-linear energy transfer in a gravity-wave spectrum Part 1. General theory. *Journal of Fluid Mechanics 12*(04), 481.

Hasselmann, S. and K. Hasselmann (1985). Computations and Parameterizations of the Nonlinear Energy Transfer in a Gravity-Wave Spectrum. Part I: A New Method for Efficient Computations of the Exact Nonlinear Transfer Integral.

Hasselmann, S., K. Hasselmann, J. H. Allender, and T. P. Barnett (1985). Computations and Parameterizations of the Nonlinear Energy Transfer in a Gravity-Wave Specturm. Part II: Parameterizations of the Nonlinear Energy Transfer for Application in Wave Models.

Hemer, M. A., J. A. Church, and J. R. Hunter (2010). Variability and trends in the directional wave climate of the Southern Hemisphere. *International Journal of Climatology 30*(4), 475–491.

Hodges, K. I. (1994, nov). A General Method for Tracking Analysis and Its Application to Meteorological Data. *Monthly Weather Review 122*(11), 2573–2586.

Hodges, K. I. (1995, dec). Feature Tracking on the Unit Sphere. *Monthly Weather Review 123*(12), 3458–3465.

Hodges, K. I. (1996). Spherical Nonparametric Estimators Applied to the UGAMP Model Integration for AMIP. *Monthly Weather Review 124*, 2914–2932.

Hoskins, B. J. and K. I. Hodges (2002). New Perspectives on the Northern Hemisphere Winter Storm Tracks. *Journal of the Atmospheric Sciences 59*(6), 1041–1061.

Hoskins, B. J. and K. I. Hodges (2005). A new perspective on Southern Hemisphere storm tracks. *Journal of Climate 18*(20), 4108–4129.

Innocentini, V. and E. D. S. C. Neto (1996, mar). A Case Study of the 9 August 1988 South Atlantic Storm: Numerical Simulations of the Wave Activity. *Weather and Forecasting 11*(1), 78–88.

Janssen, P. A. E. M. (1991). Quasi-linear Theory of Wind-Wave Generation Applied to Wave Forecasting. *Journal of Physical Oceanography 21*, 1631–1642.

Jeffreys, H. (1924). On the Formation of Water Waves by Wind. *Proceedings of the Royal Society of London 110*(754), 241–247.

Jeffreys, H. (1925). On the Formation of Water Waves by Winds II. *Proceedings of the Royal Society of Londo n 107*, 189–206.

Kita, Y., T. Waseda, and A. Webb (2018). Development of waves under explosive cyclones in the Northwestern Pacific. *Ocean Dynamics 68*(10), 1403–1418.

Komen, G. J., L. Cavaleri, M. Donelan, K. Hasselmann, S. Hasselmann, and P. A. E. M. Janssen (1994). *Dynamics and Modelling of Ocean Waves.* Cambridge: Cambridge University Press.

Kuriyama, Y., M. Banno, and T. Suzuki (2012). Linkages among interannual variations of shoreline, wave and climate at Hasaki, Japan. *Geophysical Research Letters 39*(6), 2–5.

Lim, E.-P. and I. Simmonds (2002). Explosive Cyclone Development in the Southern Hemisphere and a Comparison with Northern Hemisphere Events. *Monthly Weather Review 130*(9), 2188–2209.

Liu, Q., A. Babanin, Y. Fan, S. Zieger, C. Guan, and I. J. Moon (2017). Numerical simulations of ocean surface waves under hurricane conditions: Assessment of existing model performance. *Ocean Modelling 118*, 73–93.

Liu, Q., W. E. Rogers, A. V. Babanin, I. R. Young, L. Romero, S. Zieger, F. Qiao, and C. Guan (2019). Observation-based source terms in the third-generation wave model WAVEWATCH III: Updates and verification. *Journal of Physical Oceanography 49*(2), 489–517.

Machado, A. M., L. J. Calliari, E. Melo, and A. H. F. Klein (2010). Historical assessment of extreme coastal sea state conditions in southern Brazil and their relation to erosion episodes. *Journal of Aquatic Sciences 5*, 277–286.

Marshall, G. J. (2003). Trends in the Southern Annular Mode from observations and reanalyses. *Journal of Climate 16*(24), 4134–4143.

Menéndez, M., F. J. Méndez, I. J. Losada, and N. E. Graham (2008, nov). Variability of extreme wave heights in the northeast Pacific Ocean based on buoy measurements. *Geophysical Research Letters 35*(22), L22607.

Miles, J. W. (1957). On the generation of surface waves by shear flows. *Journal of Fluid Mechanics 3*(02), 185.

Murray, R. J. and I. Simmonds (1991). A numerical scheme for tracking cyclone centers from digital data Part I: development and operation of the scheme. *Australian Meteorological Magazine 39*(3), 155–166.

North, G. R., T. L. Bell, R. F. Cahalan, and F. J. Moeng (1982). Sampling Errors in the Estimation of Empirical Orthogonal Functions. *Monthly Weather Review 110*(7), 699–706.

Pachauri, R. K., M. R. Allen, V. R. Barros, J. Broome, W. Cramer, R. Christ, J. A. Church, L. Clarke, Q. Dahe, P. Dasgupta, and Others (2014). *Climate change 2014: synthesis report. Contribution of Working Groups I, II and III to the fifth assessment report of the Intergovernmental Panel on Climate Change.* IPCC.

Pereira, H. P. P., N. Violante-Carvalho, I. C. M. Nogueira, A. Babanin, Q. Liu, U. F. de Pinho, F. Nascimento, and C. E. Parente (2017). Wave observations from an array of directional buoys over the southern Brazilian coast. *Ocean Dynamics 67*(12), 1577–1591.

Pereira, N. E. d. S. and L. A. Klumb-Oliveira (2015). Analysis of the influence of ENSO phenomena on wave climate on the central coastal zone of Rio de Janeiro (Brazil). *Journal of Integrated Coastal Zone Management - Revista de Gestão Costeira Integrada 15*(3), 353–370.

Pezza, A. B. and T. Ambrizzi (2003). Variability of Southern Hemisphere cyclone and anticyclone behavior: Further analysis. *Journal of Climate 16*(7), 1075–1083.

Pianca, C., P. L. F. Mazzini, and E. Siegle (2010). Brazilian offshore wave climate based on NWW3 reanalysis. *Brazilian Journal of Oceanography 58*(1), 53–70.

Pierson, W. J. (1955). Wind generated gravity waves. *Advances in Geophysics 2*(C), 93–178.

Pierson, W. J., M. A. Donelan, and W. H. Hui (1992). Linear and nonlinear propagation of water wave groups. *Journal of Geophysical Research 97*(C4), 5607.

Pilar, P., C. G. Soares, and J. C. Carretero (2008). 44-year wave hindcast for the North East Atlantic European coast. *Coastal Engineering 55*(11), 861–871.

Ponce de León, S. and J. Bettencourt (2019, jul). Composite analysis of North Atlantic extra-tropical cyclone waves from satellite altimetry observations. *Advances in Space Research*.

Rao, V. B., A. M. C. Do Carmo, and S. H. Franchito (2003). Interannual variations of storm tracks in the Southern Hemisphere and their connections with the Antarctic oscillation. *International Journal of Climatology 23*(12), 1537–1545.

Reboita, M. S., T. Ambrizzi, and R. P. da Rocha (2009, mar). Relationship between the southern annular mode and southern hemisphere atmospheric systems. *Revista Brasileira de Meteorologia 24*(1), 48–55.

Reboita, M. S., T. Ambrizzi, B. A. Silva, R. F. Pinheiro, and R. P. da Rocha (2019). The South Atlantic Subtropical Anticyclone: Present and Future Climate. *Frontiers in Earth Science 7*(February), 1–15.

Reboita, M. S., R. P. da Rocha, T. Ambrizzi, and C. D. Gouveia (2015). Trend and teleconnection patterns in the climatology of extratropical cyclones over the Southern Hemisphere. *Climate Dynamics 45*(7-8), 1929–1944.

Reboita, M. S., R. P. da Rocha, T. Ambrizzi, and S. Sugahara (2010). South Atlantic Ocean cyclogenesis climatology simulated by regional climate model (RegCM3). *Climate Dynamics 35*(7), 1331–1347.

Reguero, B. G., I. J. Losada, and F. J. Méndez (2015). A global wave power resource and its seasonal, interannual and long-term variability. *Applied Energy 148*, 366–380.

Richter, I., C. R. Mechoso, and A. W. Robertson (2008). What determines the position and intensity of the South Atlantic anticyclone in austral winter? - An AGCM study. *Journal of Climate 21*(2), 214–229.

Rodrigues, R. R., A. S. Taschetto, A. Sen Gupta, and G. R. Foltz (2019). Common cause for severe droughts in South America and marine heatwaves in the South Atlantic. *Nature Geoscience 12*(8), 620–626.

Rodwell, M. J. and B. J. Hoskins (2001). Subtropical Anticyclones and Summer Monsoons. *Journal of Climate 14*(15), 3192–3211.

Rusu, E. (2012). Modeling Waves in Open Coastal Areas and Harbors with Phase-Resolving and Phase-Averaged Models. *Journal of Coastal Research 29*(6), 1309.

Saha, S., S. Moorthi, H.-L. Pan, X. Wu, J. Wang, S. Nadiga, P. Tripp, R. Kistler, J. Woollen, D. Behringer, H. Liu, D. Stokes, R. Grumbine, G. Gayno, J. Wang, Y.-T. Hou, H.-y. Chuang, H.-M. H. Juang, J. Sela, M. Iredell, R. Treadon, D. Kleist, P. Van Delst, D. Keyser, J. Derber, M. Ek, J. Meng, H. Wei, R. Yang, S. Lord, H. van den Dool, A. Kumar, W. Wang, C. Long, M. Chelliah, Y. Xue, B. Huang, J.-K. Schemm, W. Ebisuzaki, R. Lin, P. Xie, M. Chen, S. Zhou, W. Higgins, C.-Z. Zou, Q. Liu, Y. Chen, Y. Han, L. Cucurull, R. W. Reynolds, G. Rutledge, and M. Goldberg (2010). The NCEP Climate Forecast System Reanalysis. *Bulletin of the American Meteorological Society 91*(8), 1015–1058.

Saha, S., S. Moorthi, X. Wu, J. Wang, S. Nadiga, P. Tripp, D. Behringer, Y. T. Hou, H. Y. Chuang, M. Iredell, M. Ek, J. Meng, R. Yang, M. P. Mendez, H. Van Den Dool, Q. Zhang, W. Wang, M. Chen, and E. Becker (2014). The NCEP climate forecast system version 2. *Journal of Climate 27*(6), 2185–2208.

Seager, R., R. Murtugudde, N. Naik, A. Clement, N. Gordon, and J. Miller (2003). Air-sea interaction and the seasonal cycle of the subtropical anticyclones. *Journal of Climate 16*(12), 1948–1966.

Simmonds, I. and K. Keay (2000). Variability of Southern Hemisphere extratropical cyclone behavior, 1958-97. *Journal of Climate 13*(3), 550–561.

Sinclair, M. R. (1994, oct). An Objective Cyclone Climatology for the Southern Hemisphere. *Monthly Weather Review 122*(10), 2239–2256.

Sinclair, M. R. (1996). A Climatology of Anticyclones and Blocking for the Southern Hemisphere. *Monthly Weather Review 124*(2), 245–264.

Stanton, T. F. R. S., D. Marshall, and R. Houghton (1932). The Growth of Waves on Water due to the Action of Wind. *Proceedings of the Royal Society of London, Series A 132*(A), 283–293.

Sun, X., K. H. Cook, and E. K. Vizy (2017). The South Atlantic subtropical high: Climatology and interannual variability. *Journal of Climate 30*(9), 3279–3296.

Taylor, K. E. (2001). Summarizing multiple aspects of model performance in a single diagram. *Journal of Geophysical Research 106*(D7), 7183–7192.

Taylor, P. K. and M. J. Yelland (2001). The Dependence of Sea Surface Roughness on the Height and Steepness of the Waves. *Journal of Physical Oceanography 31*(2), 572–590.

Thompson, D. W. J., J. M. Wallace, and G. C. Hegerl (2000, mar). Annular Modes in the Extratropical Circulation. Part II: Trends. *Journal of Climate 13*(5), 1018–1036.

Tolman, H. L. (2002). Validation of WAVEWATCH III version 1.15 for a global domain. *Technical Note 213*, 33.

Townsend, A. A. (1980, may). The response of sheared turbulence to additional distortion. *Journal of Fluid Mechanics 98*(1), 171–191.

Tsagareli, K. N., A. V. Babanin, D. J. Walker, and I. R. Young (2010). Numerical Investigation of Spectral Evolution of Wind Waves. Part I: Wind-Input Source Function. *Journal of Physical Oceanography 40*(4), 656–666.

Vera, C., W. Higgins, J. Amador, T. Ambrizzi, R. Garreaud, D. Gochis, D. Gutzler, D. Lettenmaier, J. Marengo, C. R. Mechoso, J. Nogues-Paegle, P. L. Silva Dias, and C. Zhang (2006). Toward a unified view of the American monsoon systems. *Journal of Climate 19*(20), 4977–5000.

Wandres, M., C. Pattiaratchi, and M. A. Hemer (2017). Projected changes of the southwest Australian wave climate under two atmospheric greenhouse gas concentration pathways. *Ocean Modelling 117*(2008), 70–87.

Weisse, R. and H. Gnther (2007). Wave climate and long-term changes for the Southern North Sea obtained from a high-resolution hindcast 1958-2002. *Ocean Dynamics 57*(3), 161–172.

Young, I. R. and A. V. Babanin (2006). Spectral Distribution of Energy Dissipation of Wind-Generated Waves due to Dominant Wave Breaking. *Journal of Physical Oceanography 36*(3), 376–394.

Young, I. R., M. L. Banner, M. A. Donelan, A. V. Babanin, W. K. Melville, F. Veron, and C. McCormick (2005). An integrated system for the study of wind-wave source terms in finite-depth water. *Journal of Atmospheric and Oceanic Technology 22*(7), 814–831.

Young, I. R., S. Zieger, and A. V. Babanin (2011a). Global trends in wind speed and wave height. *Science 332*(6028), 451–455.

Young, L. R., S. Zieger, and A. V. Babanin (2011b). Response to Comment on “Global Trends in Wind Speed and Wave Height”. *Science 332*(6028), 451–455.